Relativistic Plasmonics for Ultra-Short Radiation Sources

Giada Cantono

Giada Cantono. Relativistic Plasmonics for Ultra-Short Radiation Sources. Plasma Physics [physics.plasm-ph]. Université Paris Saclay (COmUE); Università degli studi (Pise, Italie), 2017. English. NNT : 2017SACLS353 . tel-01720024

NNT : 2017SACLS353

Thèse de doctorat
de
l'Università di Pisa
et de
l'Université Paris-Saclay

préparée à l'Université Paris Sud
effectuée au Laboratoire Interactions DYnamiques et Lasers, CEA Saclay

Ecole doctorale n°572:
Ondes et Matière (EDOM)
Spécialité de doctorat: Physique des Plasmas

par

Mme. Giada Cantono

Relativistic plasmonics for ultra-short radiation sources

Thèse présentée et soutenue à Saclay, le 27 Octobre 2017:

Composition du Jury:

Mme.	Marta Fajardo	Universidad de Lisboa, Professeur associé	Rapporteur
M.	Paul McKenna	University of Strathclyde, Professeur	Rapporteur
M.	Tiberio Ceccotti	CEA Saclay, Ingénieur chercheur	Directeur de thèse
M.	Andrea Macchi	CNR/INO, Università di Pisa, Chercheur	Directeur de thèse
M.	Francesco Pegoraro	Università di Pisa, Professeur	Directeur de thèse
M.	Francesco Califano	Università di Pisa, Professeur associé	Examinateur
M.	Patrick Mora	École Polytechnique, Professeur	Président du jury

Contents

Summaries

According to the reglementation of Université Paris Saclay and the PhD contract in joint supervision between France and Italy, the manuscript must include a summary in both languages of the partner universities.

Résumé en français

L'interaction d'une impulsion laser à haute intensité avec une cible solide ou gazeuse se révèle être très intéressante à cause de la possibilité de générer des sources de radiation secondaire (électrons, ions, rayonnement X ou gamma) énergétiques et brillantes. Celles-ci sont étudiées depuis désormais des dizaines d'années en tant que possible alternatives aux accélérateurs conventionnels.

Une fois focalisés, les faisceaux des systèmes laser les plus récents, qui délivrent des impulsions avec des puissances de l'ordre du PW, des énergies de dizaines de Joules et des durées aussi courtes que quelques femto-secondes, peuvent atteindre des intensités de l'ordre de $\sim 10^{22}$ W/cm^2. Tout matériel irradié dans un tel régime est transformé en plasma sur un temps de quelque cycle optique de l'impulsion laser. Les électrons libres ainsi obtenus peuvent gagner des vitesses proches de la vitesse de la lumière, avec des énergies qui varient de quelques MeV à quelques GeV en fonction de la densité du plasma et du relatif régime d'interaction.

Dans ce cadre, on définit « sur-critiques » les plasmas dont la densité dépasse la densité critique, c'est-à-dire la densité pour laquelle le plasma devient opaque à la longueur d'onde du laser utilisé. Typiquement, ces plasmas dont la densité est comparable à la densité du solide ($n \sim 10^{23}$ cm^{-3}) sont obtenus en laboratoire en faisant interagir un faisceau laser très intense et de courte durée avec une cible solide. Puisque les ondes électromagnétiques sont évanescentes dans ce milieu, l'absorption laser par la cible s'effectue via une population d'électrons du plasma qui sont accélérés par le champ laser près de l'interface avec le vide et puis réinjectés dans la région sur-critique. Il s'ensuit que pour optimiser le couplage cible-laser, ainsi que tous les autres processus secondaires qui dépendent de la dynamique des ces électrons, il faut développer de nouveaux régimes d'interactions entraînants la génération d'électrons plus énergétiques, nombreux et, dans certains cas,

plus directionnels.

Pour arriver à ce but, l'une de stratégies les plus suivies consiste à utiliser des cibles micro-structurées. Cette thèse, en particulier, adopte le schéma très connu et pratiqué en photonique de l'excitation de plasmons de surface sur des réseaux de diffraction, en l'étendant, pour la toute première fois, au régime des intensités laser relativistes (*i.e.* $I > 10^{18}$ W/cm^2).

Les plasmons de surface sont des oscillations collectives des électrons à l'interface entre deux matériaux de constante diélectrique différente. Confinées dans la direction perpendiculaire à l'interface, ces ondes permettent la concentration et la propagation de champs électromagnétiques intenses sur des distances inférieures à la limite de diffraction. Elles offrent par conséquent beaucoup d'applications à basse intensité telles que le développement de guides d'onde, nano-circuits, bio-senseurs, techniques d'imagerie, etc.

Dans le régime d'interaction relativiste les plasmons de surface sont excités lorsque le laser irradie la surface du réseau avec un certain angle d'incidence, dit angle de résonnance, qui dépende principalement du pas du réseau. D'un point de vue expérimental, le contraste temporel du laser doit être suffisamment élevé pour que l'intensité du piédestal, produit par l'amplification de l'émission spontanée le long de la chaîne laser, n'efface pas la périodicité de la cible avant l'interaction avec le pic de l'impulsion. Seulement le récent développement de techniques pour l'amélioration du contraste laser, comme le miroir plasma, a permis d'utiliser de cibles micro-structurées dans l'interaction laser-plasma à haute intensité.

C'est dans ce contexte que les expériences réalisées au CEA (Saclay, France) ont permis d'explorer l'excitation résonnante de plasmons de surface à intensités relativistes, en ouvrant la voie au tout nouveau domaine de la Plasmonique Relativiste. Des simulations numériques avaient déjà étudié les plasmons de surface dans le but d'améliorer le couplage cible-laser, montrant que l'augmentation de l'intensité du champ électrique à la surface du plasma sur-critique favorise la génération d'électrons énergétiques; ceux-ci, traversant la cible, créent des champs électriques intenses et accélèrent des faisceaux d'ions à haute énergie. En 2012, une première expérience a corrélé l'augmentation de l'énergie maximale des protons accélérés à la surface arrière des cibles réseau avec l'excitation de plasmons de surface. Cette thèse présente l'étude expérimentale et numérique de deux autres effets: l'accélération d'électrons à la surface de la cible, produite directement par les champs du plasmon, et la génération d'harmoniques d'ordre élevé de la fréquence laser.

Dans le premier cas, les électrons extraits de la surface de la cible par le champ électromagnétique du laser peuvent être injectés dans le plasmon et accélérés par la composante longitudinale du champ électrique. Puisque le plasmon a une vitesse de phase proche de la vitesse de la lumière, les électrons restent en phase avec l'onde et atteignent des énergies relativistes. Les expériences réalisées au cours de cette thèse ont montré la présence de paquets d'électrons collimatés, stables, avec des énergies d'une dizaine de MeV, accélérés le long de la surface des cibles réseau irradiées à l'angle de résonnance pour l'excitation des plasmons de surface. La charge contenue dans le faisceau d'électrons varie de 40 à 700 pC en fonction du type de réseau utilisé. Par comparaison, l'émission électronique des cibles constituées par des simples feuilles minces est environ ~ 20 fois moins intense et diffusée sur une grande région autour de la réflexion spéculaire de l'impulsion laser.

L'accélération d'électrons provoquée par les plasmons de surface se distingue pour sa robustesse (le paquet d'électrons a été observé avec plusieurs types de réseaux) et la facilité de sa mise en œuvre (les cibles réseau peuvent être intégrées dans des géométries complexes et ils ne demandent aucune ultérieure modification de leur état de surface, à différence d'autres mécanismes qui sont très sensibles à la présence de gradients de densité à la surface de la cible). Le pic d'énergie à ~ 10 MeV est aussi prometteur pour les applications qui utilisent de paquets d'électrons de modeste énergie et courte durée ($\sim$ fs), tel que la diffraction d'électrons pour des expériences pompe-sonde ou la générations des photo-neutrons.

Au même temps, l'interaction non-linéaire entre l'impulsion laser et le plasma sur-critique aboutit à la génération d'harmoniques de la fréquence laser. En particulier, les électrons du plasma qui oscillent à travers l'interface avec le vide réfléchissent le champ laser incident et provoquent un décalage en fréquence par effet Doppler. Puisque le plasmon augmente le champ à la surface, on s'attend à ce que les électrons étant énergétiques produisent un spectre harmonique plus intense et étendu en fréquence. Le manuscrit présente ainsi la toute première observation expérimentale de cet effet : l'excitation d'un plasmon de surface s'avère être corrélée avec une augmentation des harmoniques émises le long de la tangente du réseau (jusqu'à $\sim 35\omega$). L'augmentation des harmoniques associée à la séparation angulaire de la fréquence laser fondamentale encourage le développement d'une source quasi-monochromatique d'intérêt pour des applications d'imagerie et spectroscopie XUV.

De plus, puisque le processus de génération des harmoniques est optimisé via la création d'un gradient de densité, ces résultats démontrent la possibilité de modifier le profil transverse du réseau à l'échelle nanométrique, sans en abîmer la périodicité et donc sans empêcher l'excitation du plasmon de surface. La mesure des électrons accélérés le long de la surface de la cible, effectuée au même temps que celle des harmoniques, confirme l'excitation des ondes de surface même en présence d'un pré-plasma.

En conclusion, cette thèse présente l'étude expérimentale et numérique de l'excitation des plasmons de surface en régime relativiste sur des cibles réseaux. Les résultats détaillés dans le manuscrit montrent la possibilité d'étendre la plasmonique à des champs très intenses et soutiennent le développement de sources compactes d'électrons et de rayonnement XUV.

Riassunto in italiano

L'interazione di un impulso laser ad alta intensità con un bersaglio solido o gassoso richiama un notevole interesse per la possibilità di generare sorgenti di radiazione secondaria (elettroni, ioni, raggi X o gamma) energetiche e ad alta brillanza. Tali sorgenti sono studiate da ormai decine di anni come alternativa agli imponenti acceleratori convenzionali, tra le cui limitazioni spiccano i costi di ampliamento sempre più proibitivi.

I più moderni sistemi laser oggi forniscono impulsi con potenze dell'ordine del PW, energie di decine di Joule e durata di pochi femtosecondi, che possono essere focalizzati fino a raggiungere intensità dell'ordine di $\sim 10^{22}$ W/cm^2. Qualsiasi materiale irradiato in questo regime si trasforma in un plasma fortemente ionizzato, i cui elettroni possono essere accelerati a velocità relativistiche nel corso di pochi cicli ottici dell'impulso laser. A seconda della densità del plasma, diversi regimi di interazione permettono agli elettroni di raggiungere energie che spaziano da pochi MeV fino a qualche GeV lungo distanze di qualche millimetro.

In questo contesto, i plasmi sovradensi sono caratterizzati da densità che superano la cosiddetta densità critica, *i.e.* la densità per cui il plasma risulta opaco ad un impulso laser di una specifica lunghezza d'onda. Tipicamente, questi plasmi sono ottenuti in laboratorio quando un impulso laser intenso ionizza un bersaglio solido; dunque il plasma ha una densità confrontabile con quella del solido ($n \sim 10^{23}$ cm^{-3}) e può sostenere la propagazione di correnti elevate. Poiché le onde elettromagnetiche sono evanescenti all'interno di tale mezzo, l'assorbimento dell'energia laser da parte del plasma è mediato da una popolazione di elettroni del plasma che sono accelerati dal campo laser in prossimità dell'interfaccia con il vuoto e poi re-iniettati nella regione sovradensa. Di conseguenza, ottimizzare sia l'accoppiamento laser-bersaglio sia tutti i processi secondari che dipendono dalla dinamica di tali elettroni richiede di sviluppare nuovi regimi di interazione che risultino nella generazione di elettroni più energetici, più numerosi e, in alcuni casi, più direzionali.

A tal fine, una delle strategie più indagate consiste nell'utilizzo di bersagli micro-strutturati. Nel lavoro descritto in questa tesi, in particolare, si adotta lo schema ben noto e largamente applicato in fotonica dell'eccitazione risonante di plasmoni di superficie su reticoli di diffrazione, esportandolo al regime di intensità laser relativistiche (*i.e.* $I > 10^{18}$ W/cm^2).

I plasmoni di superficie sono oscillazioni collettive degli elettroni presenti all'interfaccia tra due materiali aventi constanti dielettriche diverse. Essendo confinati nella direzione perpendicolare all'interfaccia, permettono la concentrazione e la propagazione di forti campi elettromagnetici su distanze inferiori al limite di diffrazione; hanno quindi numerose applicazioni a bassa intensità nello sviluppo di guide d'onda, nanocircuiti, biosensori, tecniche di imaging, ecc.

Fra i vari metodi di accoppiamento per eccitare i plasmoni di superficie con un impulso laser, lo schema basato sull'uso di reticoli di diffrazione è l'unico applicabile anche al regime relativistico, in cui la rapida ionizzazione del bersaglio impedisce di ricorrere alle classiche combinazioni di materiali dielettrici differenti. Con questo approccio, il plasmone di superficie è eccitato quando il laser irradia la superficie del reticolo a un preciso angolo di incidenza, detto angolo di risonanza, che dipende in primo luogo dal solo periodo del reticolo. Ciononostante, è essenziale che il contrasto temporale dell'impulso laser sia sufficientemente alto affinché l'intensità del piedistallo, prodotto dall'amplificazione dell'emissione spontanea lungo la catena laser, non cancelli la periodicità del bersaglio prima dell'interazione con il picco dell'impulso. E' solo di recente che l'implementazione di tecniche per il controllo del contrasto laser, come lo specchio al plasma, ha reso possibile l'impiego di bersagli micro-strutturati nelle interazione laser-plasma in regime relativistico.

Combinando questi elementi, gli esperimenti realizzati al CEA (Saclay, Francia) hanno inaugurato l'esplorazione del nuovo filone della Plasmonica Relativistica. Precedentemente, solo le simulazioni numeriche ne avevano incoraggiato lo studio per migliorare l'accoppiamento laser-bersaglio. In particolare, l'aumento dell'intensità del campo elettrico alla superficie del plasma sovradenso favorisce la generazione di più elettroni energetici; questi ultimi, una volta attraversato il bersaglio, danno luogo a campi elettrici intensi che possono accelerare fasci di ioni ad alta energia. Risale al 2012 il primo esperimento in cui l'aumento dell'energia massima dei protoni accelerati dalla superficie posteriore di reticoli sottili è stato correlato all'eccitazione di plasmoni di superficie. In questa tesi si presenta lo studio sperimentale e numerico di altri due effetti: l'accelerazione di elettroni alla superficie del bersaglio, prodotta direttamente dai campi del plasmone, e la generazione di armoniche della frequenza laser.

Nel primo caso, gli elettroni estratti alla superficie del bersaglio dal campo elettromagnetico del laser possono essere iniettati nel plasmone e accelerati dalla componente longitudinale del campo elettrico. Poiché il plasmone ha una velocità di fase confrontabile con la velocità della luce, gli elettroni restano in fase a lungo con l'onda e possono raggiungere energie relativistiche. Gli esperimenti realizzati nel corso di questa tesi hanno rivelato la presenza di pacchetti di elettroni collimati, stabili, di energie intorno alla decina di MeV, accelerati lungo la superficie dei reticoli irraggiati all'angolo di risonanza per l'eccitazione dei plasmoni di superficie. La carica contenuta nel fascio di elettroni spazia dai 40 ai 700 pC a seconda del tipo di reticolo utilizzato. In confronto, bersagli costituiti da semplici fogli piani producono un'emissione ~ 20 volte meno intensa, distribuita in un'ampia regione intorno alla riflessione speculare dell'impulso laser.

L'accelerazione di elettroni causata dai plasmoni di superficie risalta per la sua robustezza (il pacchetto di elettroni è stato osservato con diversi tipi di reticoli) e facilità di implementazione: infatti il reticolo può essere integrato in geometrie complesse e non è necessario manipolare la densità del bersaglio per accelerare il fascio di elettroni (come invece è richiesto in altri meccanismi fortemente sensibili alla presenza di gradienti di densità alla superficie del bersaglio). Il picco di energia a $\sim$ 10 MeV è anche promettente per applicazioni che richiedono pacchetti di elettroni a energie modeste, ma di breve durata ($\sim$ fs), come la diffrazione di elettroni per esperimenti pompa-sonda o la generazione di foto-neutroni.

Allo stesso tempo, l'interazione non lineare tra l'impulso laser e il plasma sovradenso risulta nelle generazione di armoniche della frequenza laser. In particolare, gli elettroni del plasma che oscillano attraverso l'interfaccia con il vuoto riflettono il campo elettrico incidente, causando uno shift in frequenza per effetto Doppler. Poiché il plasmone aumenta il campo alla superficie, è possibile che gli elettroni più energetici generino uno spettro armonico più intenso più esteso in frequenza. Il manoscritto presenta la prima osservazione sperimentale di questo effetto: l'eccitazione di un plasmone di superficie è correlata a un aumento delle armoniche emesse lungo la tangente del reticolo (fino a $\sim 35\omega$). L'aumento delle armoniche combinato con la separazione angolare dalla frequenza laser fondamentale supporta lo sviluppo di una sorgente quasi-monocromatica, di particolar interesse per applicazioni di imaging e spettroscopia XUV.

In più, poiché il processo di generazione delle armoniche è ottimizzato in presenza di un gradiente di densità, questi risultati dimostrano la possibilità di modificare il profilo trasverso del reticolo su scala nano-metrica, senza alterarne la periodicità e quindi senza ostacolare l'eccitazione del plasmone di superficie. La misura degli elettroni accelerati lungo la superficie del bersaglio, svolta contemporaneamente alla rilevazione delle armoniche, fornisce un'ulteriore prova dell'eccitazione efficace delle onde di superficie anche in presenza di un pre-plasma.

In definitiva, questa tesi presenta lo studio sperimentale e numerico dell'eccitazione in regime relativistico di plasmoni di superficie su reticoli di diffrazione. I risultati discussi nel manoscritto dimostrano la possibilità di estendere la plasmonica agli alti campi e incoraggiano lo sviluppo di sorgenti compatte di elettroni e radiazione XUV.

Relativistic plasmonics
for ultra-short radiation sources

Introduction

Laser-based radiation sources promise to tackle the physics and applications which are currently prerogative of large-scale conventional facilities, be they electron [1] or ion accelerators [2], X [3] and γ-ray [4] sources. Leading the progress in laser technology, PW-class laser systems can now deliver pulses with energy of tens of Joules and duration of few femtoseconds, attaining focused intensities in the range of $\simeq 10^{22}$ W/cm^2, able to turn any material into a fully ionized plasma. Depending on its density, this environment allows the excitation of nonlinear plasma waves in the wake of the intense laser pulse, which are associated to accelerating fields of over 100 GeV/m. Under such high fields, electrons are accelerated at relativistic velocities within few laser cycles, achieving GeV energies over extremely short distances [5]. In return, these acceleration schemes require the plasma to be *underdense*[1], in order for the external laser beam to excite the plasma wakes. As drawback, less than 100 pC of charge are typically obtained in these regimes.

On the other hand, *overdense* plasmas usually result from focusing an intense laser pulse on a solid target. They supply, hence, charge densities comparable to the solid ones ($n_e \sim 10^{23}$ cm^{-3}) and can potentially generate very high currents. The main inconvenient in this case is that electromagnetic waves cannot propagate inside the plasma. Then, energy absorption occurs when the plasma electrons are efficiently accelerated at the vacuum-plasma boundary by the external laser field and then re-injected into the overdense region. The optimization of both the laser-target coupling and whatever process is mediated by the electron dynamics (*e.g.* ion acceleration, XUV emission) requires, in the first place, to develop new interaction regimes aiming to the generation of more energetic, more numerous, and in some cases more directional, *hot* electrons.

In this context, aside to the development of even more powerful laser systems, a popular, challenging approach, which brings together plasma physics, materials science, engineering and photonics, is the use of microstructured targets. In particular, transposing a successful concept, well-

---

[1] Consistently with the definition provided in chapter 1, the value of the electronic plasma density n_e discriminates underdense and overdense plasmas in relation to the critical density $n_c = 1.1 \times 10^{21} \lambda_{[\mu\mathrm{m}]}^{-2} \mathrm{cm}^{-3}$ (with λ the laser wavelength). For overdense plasmas, it is $n_e \gg n_c$.

known to photonics, to the high-field regime, this thesis presents in-depth experimental studies on the resonant excitation of Surface Plasmons (SPs) at relativistic laser intensities (*i.e.* $I > 10^{18}$ W/cm^2) on grating targets.

Plasmonics is the branch of photonics that studies how the electromagnetic radiation couples with the collective oscillations of the electrons inside a conductor. Surface Plasmons, in particular, are confined across the interface between the conductor and a dielectric, and achieve strong enhancement of the local EM field over sub-wavelength dimensions. In the low-intensity regime, they find many applications involving light propagation along waveguides and focusing below the diffraction limit, such as the development of nano-circuitry, near field optical microscopy, photodetectrors and biosensors, among others [6, 7].

Despite their extreme potential, SPs in the relativistic regime are mostly unexplored and have no real applications yet. The first drawback is that a fully relativistic, nonlinear theory on SPs does not exist. Nevertheless, numerical simulations soon disclosed the possibility of resonant SP coupling with highly-intense laser pulses even for the phase-matching conditions prescribed by the linear theory. A more serious shortcoming revolved around the experimental feasibility of such a resonant coupling. In fact, SPs can be excited by an external EM radiation provided that suitable target configurations are adopted. As all the coupling schemes based on multi-layered dielectric materials are undermined by rapid target ionization, the only reliable approach in the high field regime is the so-called grating coupling, where the laser-irradiated target has a periodically-modulated surface. In this case, the SP is excited when the laser impinges on the grating at a specific resonant angle which depends essentially on the groove spacing. Even so, in a high-power laser chain the amplified spontaneous emission gives rise to an intensity pedestal which is typically intense enough to destroy the grating structuring before the arrival on target of the peak intensity. Such issue about the laser temporal contrast was overcome quite recently with the development of pulse-cleaning techniques like the Double Plasma Mirror [8].

In this newly-adapted scenario, the experiments carried out at CEA are definitely groundbreaking. It dates back to 2012 the first demonstration of the SP-assisted increase of the cutoff energy of proton beams accelerated at the rear surface of grating targets [9]. The work described in this manuscript moves further on, characterizing the role of relativistic SPs in the acceleration of massive electron bunches along the grating surface [10] and the enhancement of the High-order Harmonic (HH) emission. Remarkably, these experimental results have no precedents in the investigation of plasmonic structures at relativistic laser intensities.

The sketch in figure 1 ancipates the most significant results. Energetic electrons pulled out from the overdense plasma by the laser field can be trapped and accelerated at relativistic energies by the longitudinal component of the SP electric field. Since the SP has a phase velocity close to speed

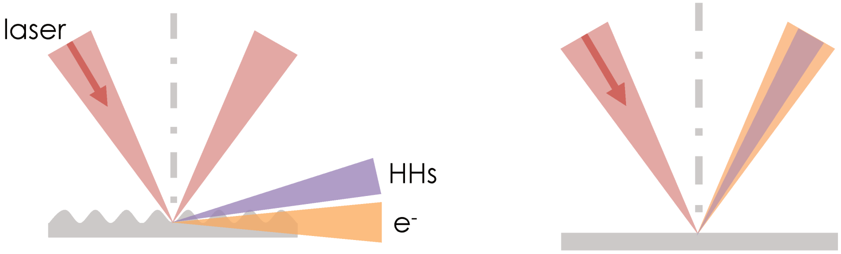

(a) grating at resonance (b) flat foil

Figure 1: Schematic description of the electron and harmonic emissions presented in this work. (a): when the grating is irradiated at the resonant angle for SP excitation, energetic electrons and broad harmonic spectra are observed along the target surface. (b): in comparison, flat targets reflect the laser pulse in the specular direction, where most of the electron signal is detected too.

of light, electrons do not overrun the wave and are accelerated for a long time. The experiments gave striking evidence of this mechanism, with the observation of stable, multi-MeV, low-divergence electron bunches accelerated along the grating surface for laser incidence at the SP resonant angle. In particular, the most efficient grating geometry produced 650 pC of charge, having a non-Maxwellian energetic distribution peaked at $\sim$ 10 MeV. In comparison, flat targets exhibited a $\sim$ 20 times weaker broad emission around the specular reflection of the laser pulse. The electron acceleration in this regime stands out for its robustness (the electron bunch was detected with different kinds of gratings) and ease of implementation: not only the grating is suitable for being integrated in complex devices, but the electron yield is pretty straightforward, without the need to manipulate the plasma density gradient as required by other acceleration mechanisms [11]. The energy peak at $\sim$ 10 MeV is also promising for applications requiring moderate energies, fs-scale electron bunches, like ultra-fast electron diffraction [12] or photoneutron generation [13].

Resonant SPs on grating targets are also studied in the context of HH generation. The plasma electrons oscillating across the target surface reflect the incoming laser light, inducing a frequency shift because of the Doppler effect. As the SP increases the local electric field at the grating surface, more energetic electrons are expected to drive the harmonic emission to broader, more intense spectra [14]. For the first time the experiment reported here proved that a relativistic SP is related to an augmentation of the harmonic orders (up to $\sim 35\omega$) along a preferred direction, close to the grating surface and well-separated by the reflection of the fundamental laser frequency. Additionally, as optimizing the HH generation requires that the laser interacts with a short gradient of plasma density, these results demonstrate the possibility to tailor the grating profile on a nano-metric scale without spoiling the excitation of the surface wave. Eventually, the harmonic enhancement combined with the angular separation of the different frequencies supports the development of a near-monochromatic source, with possible relevancy to XUV imaging and spectroscopic applications [15].

The manuscript is organized as follows.

- Chapter 1 provides the theoretical framework for the physical scenario discussed in this work. It revises the most significant concepts of highly-intense laser-solid interaction, with particular attention to the mechanisms of electron acceleration relevant to energy absorption. It develops the theory of Surface Plasmons and discusses the key points for their excitation in the high-field regime.
- Chapter 2 presents the UHI100 laser system, the experimental arrangement and targets employed throughout the thesis. The second part describes the Particle-In-Cell code PICCANTE used to realize two-dimensional simulations in support of the experimental data.
- Chapter 3 reports on SP-driven electron acceleration. This topic is presented with a theoretical model, plenty of experimental results and numerical simulations. This chapter provides compelling evidence of the excitation of Surface Plasmons at relativistic laser intensities.
- Chapter 4 is devoted to the SP-enhanced High-order Harmonic emission. The first part addresses the role of the plasma density gradient on the mechanisms of HH generation; accordingly, the experimental setup is adapted to enable the creation of controlled amounts of pre-plasma on the target surface. The second part reports the experimental and numerical results.
- Appendices A, B, C describe the procedures for the analysis of the experimental data.
- Appendix D reports the experimental observations of SP-enhanced proton acceleration from the rear surface of the grating targets. This topic is quite marginal due to previous results already obtained prior to this work [9].

Note on the author's contribution

This manuscript accounts for my scientific work on laser-driven Surface Plasmons, which ironically started few weeks before the official beginning of my PhD project. In fact, I actively took part in 2014 to the experimental campaign at CEA Saclay (France) that first observed the SP-driven electron acceleration. These results, which I contributed to obtain and analyze, were included in the PhD thesis by L. Fedeli[2] [16] and yielded a first scientific publication [10].

Since then, I carried out more than 10 experimental runs devoted to the study of different target structurings for improving the laser-target coupling. Some of them, addressing the role of carbon nanotubes on the surface of thin foils, were performed in collaboration with S. Hulin[3] from CELIA (Bordeaux, France) and researches from ILIL (Pisa, Italy). As plasmonic effects with grating targets were soon identified as the most thrilling topic of the PhD project, the results from these other experiments are not included in this manuscript.

At CEA, I was in charge of building the experimental arrangement from scratch, from delivering the laser beam to the target, optimizing the focal spot (with an intense work on the Deformable Mirror), to setting up the imaging systems and diagnostics. I was responsible for the target preparation (mounting the plastic foils on their respective holders, by paying attention to the alignement of the grating grooves) and installation inside the vacuum chamber. During the experiments I handled the target alignment, the diagnostics' records, and evaluated with my colleagues the best approach to optimize the laser-plasma interaction.

I was in charge of the calibration of the scintillating Lanex screens at both facilities PHIL and ELYSE (Orsay, France). I participated to the experimental campaign at GIST (Gwangju, South Korea) contributing to the design of the target holders and adapting the diagnostics for the detection of SP-driven electron bunches.

I personally analyzed all the experimental data concerning the electron acceleration and the High-order Harmonic emission. In the second case, I tightened a fruitful collaboration with the colleagues A. Deneoud et L. Chopineau who are specialized in HH generation within the LIDYL group at CEA.

With the precious help and supervision of A. Sgattoni[4], I learned how to use PICCANTE to run my PIC simulations on High-Performance-Computing clusters. I set up the input files and processed the outputs. I cross-checked my results with L. Fedeli, contributing to the interpretation of his exploratory work on HH generation [14].

Further details about the participation to international conferences and publications are given at the end of the manuscript.

---

[2] At the time of this experiment, affiliated to *Enrico Fermi Department of Physics, University of Pisa, Pisa*; currently at *Dipartimento di Energia, Politecnico di Milano*, (Italy).

[3] *Université de Bordeaux, CNRS, CEA, CELIA (CEntre Lasers Intenses et Applications), Talence (France).*

[4] *LULI-UPMC, Sorbonne Universités, CNRS, Ecole Polytechnique, CEA, Paris*, and *LESIA, Observatoire de Paris, CNRS, UPMC, Meudon (France).*

Chapter 1

Theoretical framework

This work ventures on the experimental investigation of Surface Plasmons (SPs) in the relativistic regime[1]. These electromagnetic waves are the cornerstone of Plasmonics, a well-established research field with plenty of applications, yet at low laser intensities. The main issue with stepping to ultra-high intensities is that any laser-irradiated material becomes a strongly conductive plasma, impairing the excitation of SPs via the usual techniques that require multi-layer systems with different dielectric properties. At the same time, the theoretical treatment of SPs in the high field regime is mostly unexplored, and non-linear effects are expected to take place.

Supported by a great deal of numerical simulations, the experimental study of SPs in the relativistic regime is now accessible thanks to the latest advances in laser and target technology. The work described in this manuscript is hence stimulated by the opportunity to analyze various SP-related phenomena at ultra-high laser intensity directly in the laboratory.

---

[1] I.e. when the EM fields are strong enough that the electron dynamics requires a relativistic description.

This chapter surveys some of the most significant concepts to highly-intense laser-solid interaction, in order to frame the physical scenario where SPs are expected to play a role. The first part focuses on basic definitions and the main electron acceleration mechanisms that ensure the absorption of the laser energy by the target. Enlightening the mechanisms behind the electron generation is of paramount importance not only to develop energetic electron sources, but also because hot electrons mediate significant secondary processes such as X-ray, γ-ray emission and ion acceleration. Evidently all these phenomena would benefit from enhanced energy absorption, which in turn requires to improve the hot electron acceleration at the target surface. Surface plasmons, thoroughly introduced in the second part of this chapter, can indeed drive the electrons to higher energies, since they increase the local field amplitude at the target surface.

1.1 Highly-intense laser-solid interaction

1.1.1 Overdense plasmas

Atoms and molecules forming a target undergo different ionization processes when irradiated by a laser pulse. The dominant one for laser intensities above 10^{14} W/cm^2 is known as *over-the-barrier* ionization: the Coulomb potential that confines the electron to the parent nucleus is so much bent by the laser field that the electron immediately escapes [17].

In the laser-solid interactions relevant to this work, the laser intensity exceeds the ionization threshold of any material by some orders of magnitude: therefore the target is highly ionized, and the resulting plasma is globally neutral, with the electron density equal to the ion density, $n_e = Zn_i$. Furthermore, laser pulses with fs duration prevent the plasma from expanding into vacuum: as a consequence, the laser interacts with a step-like density profile whose maximum density, n_0 is close to the solid density, 10^{23} electrons/cm^3. This value is greater than the critical density n_c, defined as:

$$n_c = \frac{m_e \omega^2}{4\pi e^2} = 1.1 \times 10^{21} \lambda_{[\mu\mathrm{m}]}^{-2} \mathrm{cm}^{-3}, \tag{1.1}$$

where ω and λ are the laser frequency and wavelength. For a laser with $\lambda \simeq 800$ nm, n_c is about 2×10^{21} cm^{-3}. Plasmas with $n_e > n_c$ are usually referred to as *overdense*. A distinctive property of overdense plasmas is that they do not sustain the propagation of transverse EM waves. It is useful to derive here this result, since the wave equation will be also recalled afterwards in the presentation of surface plasmons.

Combining Maxwell's curl equations gives the wave equation:

$$\left(\nabla^2 - \frac{1}{c^2}\frac{\partial^2}{\partial t^2}\right)\mathbf{E} - \nabla(\nabla \cdot \mathbf{E}) = \frac{4\pi}{c^2}\frac{\partial \mathbf{J}}{\partial t}. \tag{1.2}$$

For a cold, unmagnetized plasma, the ion response is disregarded and the velocity equation for the electron fluid can be linearized under the assumption of low field intensities:

$$\frac{\mathrm{d}}{\mathrm{d}t}(m_e\mathbf{u}_e) = -e\mathbf{E}. \tag{1.3}$$

If the electric field is expressed as plane, monochromatic wave $\propto e^{i\mathbf{k}\cdot\mathbf{r}-i\omega t}$, then the current density becomes:

$$\mathbf{J} = -en_e\mathbf{u}_e = i\frac{e^2n_e}{m_e\omega}\mathbf{E} = \sigma\mathbf{E}$$

where σ is the conductivity [2, 18]. Rearranging the wave equation leads to:

$$\left(-k^2 + \frac{\omega^2}{c^2}\varepsilon(\omega)\right)\mathbf{E} + \mathbf{k}(\mathbf{k}\cdot\mathbf{E}) = 0,$$

with the plasma dielectric function given by

$$\varepsilon(\omega) = 1 - \frac{\omega_p^2}{\omega^2} = 1 - \frac{n_e}{n_c}, \tag{1.4}$$

containing the plasma frequency $\omega_p = \left(4\pi e^2 n_e/m_e\right)$. This one represents the frequency of collective longitudinal oscillations of the plasma electrons, for which the wavevector $\mathbf{k}$ is parallel to the electric field and $\nabla \times \mathbf{E} = 0$, implying $\varepsilon(\omega) = 0$.

In the opposite case, transverse EM waves satisfy $(\nabla \cdot \mathbf{E}) = 0$ and, for plane waves, $\mathbf{k}\cdot\mathbf{E} = 0$, leading straight away to the dispersion relation:

$$k^2c^2 = \omega^2 - \omega_p^2 = \frac{4\pi e^2}{m_e}(n_c - n_e). \tag{1.5}$$

Visibly k becomes purely imaginary if $n_e > n_c$, forbidding the wave propagation: the overdense plasma acts like a mirror. Inside the plasma, the electric field will vanish over the so-called skin depth:

$$\delta_s = \frac{c}{\sqrt{\omega_p^2 - \omega^2}} \simeq \frac{c}{\omega_p} \qquad (\text{when } \omega_p \gg \omega). \tag{1.6}$$

In the high field regime, relativistic effects become significant, so the interaction between the EM wave and the plasma is altered by many nonlinear phenomena. In fact, the electrons now oscillate in the EM field with velocities close to c and the contribution of the magnetic force to the dynamics is not negligible. In this case, the equation for the electron momentum reads:

$$\frac{\mathrm{d}}{\mathrm{d}t}(\gamma m_e\mathbf{u}_e) = -e\left(\mathbf{E} + \frac{\mathbf{u}_e \times \mathbf{B}}{c}\right). \tag{1.7}$$

The relativistic factor γ is given by:

$$\gamma = \sqrt{1 + \frac{\mathbf{p}_e}{m_e c^2}} = \sqrt{1 + \langle \mathbf{a}^2 \rangle}, \tag{1.8}$$

where the dimensionless laser parameter $\mathbf{a}$ is defined as the normalized vector potential of the EM wave, *i.e.* $\mathbf{a} = e\mathbf{A}/m_e c^2$ and the angular brackets indicate averaging over an oscillation period[2] [19]. Specifying the electric field $\mathbf{E} = (-1/c)\partial_t \mathbf{A}$, it turns out that $\mathbf{a}$ is the ratio between the quiver momentum of the electron in the EM field and $m_e c$. Therefore, it is natural to assume $\mathbf{a}$ as the parameter that discriminates the onset of the relativistic regime. In correspondence to the peak amplitude of the EM wave, a_0 is related to the laser intensity and wavelength by the well-known relation:

$$a_0 = 0.85\sqrt{10^{-18} I_{[\mathrm{W/cm^2}]} \lambda^2_{[\mu\mathrm{m}^2]}}. \tag{1.9}$$

It follows that electrons oscillate at $\sim c$ if $a_0 > 1$, so that $I \sim 10^{18}$ W/cm^2 is the laser intensity required to access to the relativistic regime. The experiments described in the following chapters are characterized by $a_0 \sim 3$.

A plane wave with circular polarization allows to solve the electron motion 1.7 with the same approach of the non-relativistic regime, since $\mathbf{u}_e \times \mathbf{B} = 0$ and γ is constant. In this case the electron mass is simply replaced by γm_e, so that the relativistic dielectric function becomes $\varepsilon(\omega) = (1 - n_e/(\gamma n_c))$ with the increased critical density $\gamma n_c > \gamma$. Therefore, the laser can now propagate within the range $n_c < n_e < \gamma n_c$, an effect known as *self-induced relativistic transparency.*

In reality, other effects must be considered as well. For instance, if the laser beam is impinging on the solid target with an incidence angle ϕ_i, it is reflected at a plasma density lower than n_c. This follows from the conservation of the wavevector component $(k \sin \phi_i)$ parallel to the vacuum-plasma interface [18]. Assuming that the incidence angle ϕ_i is taken in the $(x - z)$ plane between the propagation vector $\mathbf{k} = (k_x, k_z)$ and the direction of the density gradient (*i.e.* z), the dispersion relation 1.5 becomes $k_z^2 = \omega^2 \cos^2(\phi_i) - \omega_p^2$, so that k_z assumes imaginary values for $n_e > n_c \cos^2(\phi_i)$.

But the plasma density is also modified by the ponderomotive force, originating by the slowly-varying envelope of the EM wave. It describes the motion of the oscillation center of a charged particle in an oscillating, non-uniform field, over a timescale longer than the oscillation period. Taking the cycle-average of the relativistic kinetic energy acquired by an electron moving in a EM wave described by a vector potential $\mathbf{A}(\mathbf{r}, t)$,

$$\mathcal{E}_{\mathrm{kin}} = m_e c^2 \langle(\gamma - 1)\rangle = m_e c^2 (\sqrt{1 + \langle \mathbf{a}^2 \rangle} - 1), \tag{1.10}$$

---

[2] It is important to remark that γ depends on the nonlinear motion of the electron in the EM wave, hence it is not constant (except for circular polarization). The cycle-average is adequate to describe the electron behavior also with linear polarization [2].

the ponderomotive force turns out to be [20]:

$$\mathbf{f_p} = -\nabla \mathcal{E}_{\mathrm{kin}} = -m_e c^2 \nabla(\sqrt{1 + \langle \mathbf{a}^2 \rangle}).$$

It can also be demonstrated that against the vacuum-plasma boundary the ponderomotive force corresponds to the radiation pressure caused by the EM wave which delivers its momentum to the target surface [19]: then, intuitively, the ponderomotive force piles up the plasma electrons, further steepening the density profile and creating strong charge separations where the electric field can in turn accelerate ions [21].

1.1.2 Plasma expansion

Modeling the density profile with step-like function is generally adequate to describe overdense plasmas interacting with ultra-short, intense laser pulses. However, there are many significant cases where the interaction takes place with an already expanding plasma, for example when the most intense laser pulse is preceded by a pedestal on the ns, ps time scale (poor laser contrast, as explained in chapter 2) or when the target is deliberately pre-ionized to exploit or optimize various processes (*e.g.* resonant absorption).

For its relevancy to the mechanisms involved in the generation of High-order Harmonics, discussed in 4, it is useful to report here the derivation of the gradient scale length $L = |n/\nabla n|$ for the density profile $n(z)$ of a one-dimensional, isothermal, freely expanding plasma [2, 18].

Let the plasma at $t = 0$ be a step-like density function along z, $n_{e,i} = n_{e0,i0}\Theta(z)$ (with initial densities $n_{e0} = Zn_{i0} = n_0$). On the time scale of the ion motion, the electrons can be considered in equilibrium with the electrostatic field, so that the fluid equation for the electron mean velocity gives $n_e eE = -\partial_z(n_e T_e)$. Disregarding the ion pressure, the ion's equations then become:

$$\frac{\partial n_i}{\partial t} + \frac{\partial(n_i u_i)}{\partial z} = 0, \qquad \frac{\partial u_i}{\partial t} + u_i \frac{\partial u_i}{\partial z} = -c_s^2 \frac{1}{n_i}\frac{\partial n_i}{\partial z},$$

where $c_s^2 = ZT_e/m_i$ is the ion acoustic velocity. This system allows a self-similar solution given by:

$$u_i = c_s + z/t, \qquad n_i = n_{i0} \exp\left(-\frac{z}{c_s t}\right). \tag{1.11}$$

This result shows that the $z = -c_s t$ is a rarefaction front that moves with the ion-acoustic velocity. The density profile is an exponential ramp with the gradient scale length $L = c_s t$. As a general rule, step-like plasma profiles are characterized by $L \leq \lambda$ [22].

To summarize, fully ionized solid targets result in overdense plasmas. For short laser durations ($\sim$ fs), the plasma does not expand into vacuum and retains a step-like density profile. Conventionally, these profiles are characterized by $L = |n/\nabla n| \ll \lambda$, where L is the scale length the exponential density gradient expanding towards vacuum.

The laser cannot propagate within the overdense plasma and it is reflected at the critical surface $n_e = n_c$. Relativistic effects become significant when the laser intensity exceeds 10^{18} W/cm^2(*i.e.* $a_0 > 1$), giving rise to nonlinear processes that affect the laser propagation (*e.g.* self-induced transparency, self-focusing, etc.). In addition to the rapidly oscillating motion in the EM field, the ponderomotive force also pushes the plasma electrons inwards, steepening the density profile.

1.1.3 Energy absorption

Although the overdense plasma basically reflects the laser pulse, the energy is delivered to the target by a population of energetic electrons that are accelerated by the laser EM field at the critical surface. As a matter of fact, these so-called *fast* or *hot* electrons are usually detected in laser-solid interaction experiments at ultra-high intensity: they exhibit energies of the order of the cycle-averaged kinetic energy in vacuum,

$$\mathcal{E}_{\text{hot}} \simeq m_e c^2(\sqrt{1 + a_0^2/2} - 1) \simeq \mathcal{E}_{\text{kin}}, \tag{1.12}$$

where a_0 is the dimensionless laser parameter 1.9 and the last equality refers to the ponderomotive energy 1.10. A quick estimate for the laser intensity presented in the following chapter, *i.e.* $I \sim 3 \times 10^{19}$ W/cm^2, gives $\mathcal{E}_{\text{hot}} \sim 1$ MeV.

This part reviews the fundamental mechanisms developed to explain the hot electron generation from solid targets, following the accurate descriptions given in [2, 19]. A simplified framework is given in figure 1.1. Although undeniably helpful to explain the most important features of hot electrons, none of these mechanisms is able to fully account for the extreme sensitivity of the generation process to both laser and plasma parameters. On account of several numerical and experimental observations, it is normally agreed to describe hot electrons with a Maxwellian distribution, whose temperature T_{hot} corresponds to the kinetic energy 1.12 [17].

It is worth mentioning that collisional processes are unsuited to justify the hot electron acceleration: even adding a friction term in the electron equation of motion, $-m_e\mathbf{u}_e\nu_c$, so that the dielectric function 1.4 acquires an imaginary term, the collisional ion-electron frequency ν_c is proportional to $\mathbf{u}_e^{-3}$. Being the electron velocity $\mathbf{u}_e$ either the thermal speed ($\propto T_e$) or the oscillation velocity in highly-intense fields $\propto eE_0/m_e\omega$, the collisional frequency decreases as soon as the electrons gain energy.

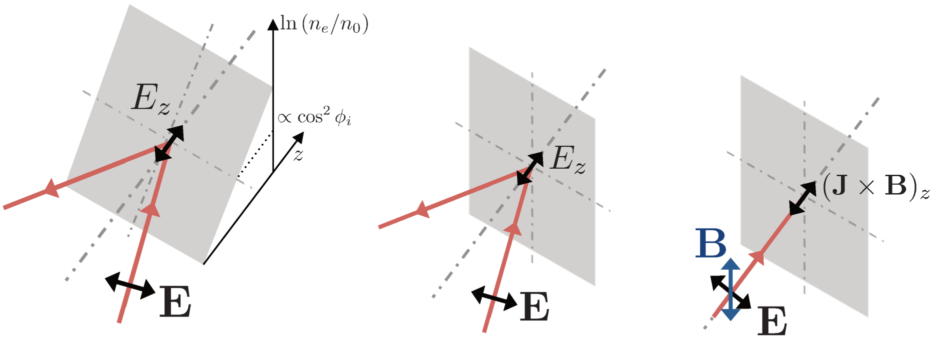

(a) Resonance absorption (b) Vacuum heating (c) J×B heating

Figure 1.1: Collisionless absorption mechanisms. Each picture shows the incoming laser beam (either at oblique or normal incidence) and the relevant components of the EM field. Hot electrons are accelerated across the surface and injected inside the overdense plasma, where the laser cannot penetrate. In the panel of resonance absorption (a), the tilted target represents the plasma-gradient; the reflection density $\propto n_c \cos^2(\phi_i)$ is also indicated.

Resonant absorption

Resonant absorption (figure 1.1a) relies on the excitation of plasma waves at the critical surface [23]. As for overdense plasmas it is $\omega_p \gg \omega$, this process typically requires a gentle density gradient at the target surface, which can be produced by the laser low-intensity pedestal (a deeper discussion about the gradient formation is provided in chapter 4.3). If the density gradient is characterized by the scale length $L = |n_0/\nabla n_0|$, with n_0 the background density, resonant absorption is efficient if $L/\lambda \simeq 1$ [23].

A straightforward description of this mechanism is obtained by solving the fluid equations of the plasma electrons within an external electrostatic field and a one-dimensional inhomogeneous background plasma $n_0 = n_0(z)$:

$$\begin{cases} \partial_t n_e + \nabla(n_e \mathbf{u}_e) = 0 \\ m_e(\partial_t \mathbf{u}_e + \mathbf{u}_e \cdot \nabla \mathbf{u}_e) = -e(\mathbf{E} + \mathbf{E}_d), \end{cases}$$

where the driver field $\mathbf{E}_d = \mathcal{R}e(\tilde{\mathbf{E}}_d e^{-i\omega t})$ represents the laser field and $\mathbf{E}$ is the electric field self-consistently generated by the density perturbation $\delta n_e = (n_e - n_0(z))$, for which Poisson's equation holds:

$$\nabla \cdot \mathbf{E} = -4\pi e(n_e - n_0(z)).$$

With the assumption that within an oscillation in the driver field the electron sees a uniform plasma density, *i.e.* $u_{e,z}/\omega \ll L$, the equation of motion can be linearized and solved for δn_e to give:

$$\tilde{\delta n_e} = \frac{1}{4\pi e}\frac{(\tilde{\mathbf{E}} + \tilde{\mathbf{E}}_d)\cdot\nabla n_0}{n_0 - n_c}.$$

Previous equation clearly exhibits a resonance when the local plasma density $n_0(z)$ equals the critical density. More importantly, the necessary condition for resonance absorption to take place is that the laser electric field must have a component in the same direction of the density gradient: this requires the laser electric field to be P-polarized and obliquely incident. With these restrictions the laser is reflected at $n_e = n_c \cos^2(\phi_i) < n_c$, so that only the evanescent field can excite the resonant waves.

Vacuum heating

High EM fields and steep density gradients are more suitable conditions for another electron acceleration mechanism, known as *vacuum heating* (figure 1.1b, [24]) . In this case electrons near the critical surface are dragged out of the plasma by the laser field, and re-injected in the target after a half cycle with the oscillation energy acquired in vacuum. Provided that the field is so intense that $u_{e,z}/\omega > c/\omega_p$, the electrons travel across the evanescent region and deliver their energy to the bulk. Interestingly, this process accounts for the pulsed generation of hot electron bunches, which are observed in experiments [25] and simulations [26, 27] at each laser oscillation. Similarly to resonant absorption, also vacuum heating needs the laser field to be P-polarized.

Without plunging into too many details, the electron motion can be analyzed with the same approach described in the previous section, combining the fluid equations and Poisson's equation [28]. However, the assumption $u_{e,z}/\omega \ll L$ is not valid anymore because of the assumption of a steep plasma gradient and the equation of motion cannot be linearized. The solutions for the trajectories of the electrons across the boundary contain a term of secular acceleration which produces a dephasing between $\mathbf{u}_e$ and $\mathbf{E}_d$, so that in evaluating the electron energy,

$$\frac{\mathrm{d}}{\mathrm{d}t}(m_e\gamma c^2) = -e\mathbf{u}_e\cdot\mathbf{E}$$

the cycle-average of the right-hand side term does not cancel out. Electrons re-enter the plasma with a velocity $u_{z,e} = u_d = e\tilde{E}/(m_e\omega)$; hence, in the relativistic regime, a reasonable estimation for their energy corresponds again to the ponderomotive energy 1.12, which scales as a_0.

Because of its relevancy to this work, it is more interesting to report the derivation of the absorption coefficient η and to point out how it depends on the laser intensity and incidence angle. Following the procedure described in [17], the normal component of the driver field at the step-like vacuum-plasma interface is $E_d = f(\eta)E_0 \sin(\phi_i)$, where ϕ_i is the incidence angle and $f(\eta)$ is a function of the plasma absorption itself, to take into account the energy depletion of the reflected field:

$$f(\eta) = 1 + (1-\eta)^{1/2}.$$

The surface density n_0 of the electrons that are pulled out by the driver and re-injected into the plasma can be estimated by balancing the driver field and the electric field set up by the charge separation:

$$f(\eta)E_0 \sin(\phi_i) = 4\pi e n_0.$$

Supposing that all these electrons re-enter into the plasma with the velocity $u_d = eE_d/(m_e\omega)$ (note that this is the quiver velocity due to the normal component of the driver field), then the average kinetic energy absorbed during a laser cycle is:

$$I_{\text{abs}} = \frac{n_0(\gamma-1)m_e c^2}{2\pi/\omega}, \tag{1.13}$$

where the relativistic kinetic energy has been used, and $\gamma = (1+u_d^2/c^2)^{1/2}$. Dividing the by the incident energy density of the driver field, $I_d = (c/8\pi)E_0^2 \cos(\phi_i)$, the absorption becomes:

$$\eta = \frac{I_{\text{abs}}}{I_d} = \frac{f(\eta)}{\pi a_0}\left[\left(1 + a_0^2 f(\eta)^2 \sin^2(\phi_i)\right)^{1/2} - 1\right]\frac{\sin(\phi_i)}{\cos(\phi_i)}, \tag{1.14}$$

with $a_0 = eE_0/(m_e\omega c)$, as usual.

This expression clearly indicates that the absorption increases with higher laser intensities (for a given wavelength), and larger incidence angles. Some solutions of the implicit equation for η are plotted as a function of a_0 in figure 1.2: the absorption peaks at grazing incidence if $a_0 \ll 1$, whereas for higher a_0 it forms a plateau that includes even smaller angles. By developing the expression 1.14 for $f(\eta)a_0 \gg 1$, it can be shown that η becomes independent of a_0 and has a maximum for $\phi_i = 73°$. However, at relativistic intensities the magnetic field is also expected to contribute to the electron dynamics, and numerical simulations show that the absorption for realistic plasma profiles is far from achieving 100% [17].

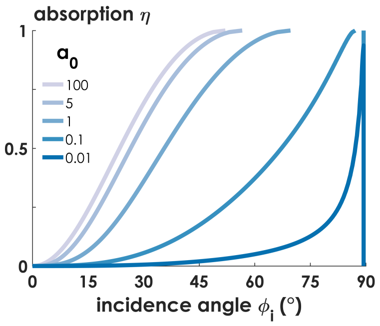

Figure 1.2: Absorption coefficient for the vacuum heating, equation 1.14.

$J \times B$ heating

For normal incidence or S-polarized pulses, both previous mechanisms are severely depressed. However, it can be demonstrated that a driving force to inject hot electrons in the overdense plasma is provided by the longitudinal magnetic force $\mathbf{u}_e \times \mathbf{B}$, as shown in figure 1.1c [29]. In this case both the electron velocity and the magnetic field oscillate at ω, so electron bunches appear every half a laser cycle (*i.e.* at 2ω). The $\mathbf{J} \times \mathbf{B}$ force has also a more favorable scaling with the laser intensity with respect to the electrostatic mechanisms, being proportional to a_0^2.

A very explicative expression for the longitudinal force acting on the sharp overdense plasma can be obtained by expressing the magnetic force as a function of the vector potential $\mathbf{A}$ of a generic plane wave, propagating along z, elliptically polarized:

$$\mathbf{A}(z,t) = \frac{A(0)e^{-z/\delta_s}}{\sqrt{1+\epsilon^2}}(\hat{\mathbf{x}}\cos\omega t + \epsilon\hat{\mathbf{y}}\sin\omega t),$$

where $\epsilon = 0, 1$ are the limit cases of linear and circular polarization. Hence it is:

$$F_z = -\frac{e}{c}(\mathbf{u}_e \times \mathbf{B})_z = -m_e c^2 \partial_x \frac{\mathbf{a}^2}{2} = F_0 e^{-2z/\delta_s}\left(1 + \frac{1-\epsilon^2}{1+\epsilon^2}\cos 2\omega t\right), \quad (1.15)$$

where $F_0 = (2m_e c^2/\delta_s)(\omega/\omega_p)^2 a_0^2$. The cycle-average of the first-term corresponds to the ponderomotive force, while the second one is responsible for the pulsed acceleration of hot electrons. However, this term vanishes for circular polarization: eventually, the lack of hot electrons turns out to assist ion acceleration mechanisms that rely solely on the radiation pressure [30].

Inserting the longitudinal magnetic force into the electron fluid equations and solving for a small electron density perturbation $\delta n_e = [\delta n_0 + \mathcal{R}e(\tilde{\delta n}_e e^{-i\omega t})]e^{-z/\delta_s}$ gives:

$$\delta n_e = n_0 \frac{2F_0}{m_e \delta_s \omega_p^2} e^{-2z/\delta_s}\left(1 + \frac{1-\epsilon^2}{1+\epsilon^2}\frac{\cos 2\omega t}{1 - 4\omega^2/\omega_p^2}\right) \qquad (z > 0).$$

The first term represents the density increase caused by the ponderomotive force. The other one shows that at resonance, *i.e.* at $\omega_p = 2\omega$, the electron density within the plasma has decreased ($\delta n_e < 0$ because of the oscillating term), indicating that some electrons have been dragged into vacuum. The later dynamics, with electrons oscillating in the laser field and re-entering the plasma, is typically depicted as in the vacuum heating mechanism.

What else?

Beyond all the subtleties imposed by each acceleration mechanism, it should be evident enough that hot electron generation strongly depends on both the laser and plasma parameters: intensity, incidence angle, polarization for the former, and density, gradient profile, thickness for the latter. By deforming the plasma surface, the radiation pressure can induce local changes of the laser incidence angle and convey the electrons currents along preferred directions of the target [31]; effects of recirculation depending on the target geometry might also increase the energy acquired by the electrons that manage to experience the acceleration from the laser field for more than one optical cycle [Sentoku2003].

Several recent works have focused on target manipulation to increase the energy absorption, typically adding micro-structures to improve ion acceleration [32–36]. Despite numerous experimental results, there are seldom conclusive arguments on the theoretical mechanisms involved: generally speaking, surface roughnesses increase the area available for the laser to interact with the plasma electrons, and induce local field enhancement [37]. More often, the fundamental picture of vacuum heating is adapted to account for strong electron acceleration along geometrical structures (micro-pillars [38], cone walls [39]) and across clusters [40], supporting charge recirculation [41]: each configuration depends primarily on the size and spacing of the micro-structures, which is typically of the order of λ. Collisional processes also come back on stage because the collisional frequency ν_c increases in presence of clustered ions [42–44].

In this work, a very simple structured target is exploited to enhance the energy absorption via the resonant excitation of a normal mode of the plasma-vacuum interface: it is the case of Surface Plasmons excited on grating targets. As detailed in the next section, these waves are localized at the surface, thus increasing the local intensity of the laser electric field. Electrons oscillating in this field behave similarly to the vacuum heating, depositing high energy into the target and eventually concurring to the development of intense space-charge electric fields that in turn accelerate ions [9, 45, 46]. Besides, the longitudinal component of the SP's electric field is suitable for direct electron acceleration along the target surface, supporting the development of a compact, bright electron source [10] that will be discussed in chapter 3.

1.2 Surface Plasmons

Surface Plasmons Polaritons (SP) are collective oscillations of the electrons of a metal at a sharp interface with a dielectric medium. These electromagnetic excitations propagate along the surface remaining confined in the perpendicular direction. This section deals with the derivation of their dispersion relation, a discussion of their properties and the methods to excite them[3]. The final part is reserved to briefly overview some applications of SPs and their possible relevancy to the relativistic regime. A model for SP-driven electron acceleration is deliberately postponed to chapter 3, closer to the experimental results.

1.2.1 The dispersion relation

The simplest configuration to infer the dispersion relation of a SP is a flat interface between two media with different dielectric constants. Referring to the geometry illustrated in figure 1.3a, the boundary is located at $z = 0$, there are no spatial variation along y and the SP propagates along x. The SP's dispersion relation is obtained by solving the wave equation for the electric and magnetic field in both regions, and matching the solutions at the interface [52].

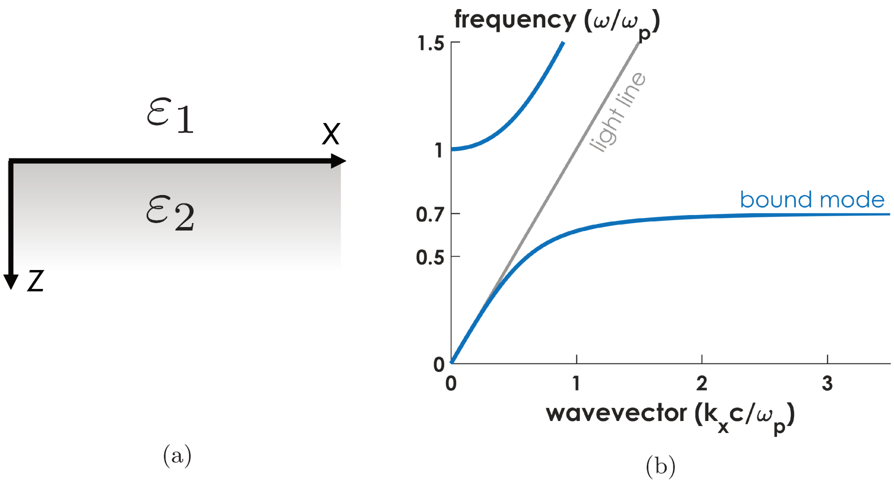

(a)

(b)

Figure 1.3: Geometry of the flat interface (a) adopted for the calculation of the SP's dispersion relation (b).

The starting point is the wave equation

$$\left(\nabla^2 - \frac{1}{c^2}\frac{\partial^2}{\partial t^2}\right)\mathbf{E}_i = \frac{4\pi}{c^2}\frac{\partial \mathbf{J}_i}{\partial t},$$

valid in each plane $i = (1, 2)$ with the assumptions that there are no external sources and the interesting solutions are transverse waves (*i.e.* $\nabla \cdot \mathbf{E}_i = 0$). Analogously to the derivation presented in the previous section, the electric

---

[3] It is worth mentioning that strong EM pulses propagating along the surface of laser-irradiated solid targets can also be excited by the transient charge separations caused by the hot electrons transport [47–49]. As these motions typically evolve on a fs-ps time scale, these processes may be relevant for the generation of THz radiation [50, 51].

field is specified as a plane, monochromatic wave, but with the additional condition that it is evanescent along z: $\mathbf{E}_i(\mathbf{r},t) = E_{0,i}e^{-k_i z}e^{jk_x x - j\omega t}$. Assuming that in both media $\varepsilon_i(\omega,\mathbf{k}) = \varepsilon_i(\omega)$, the wave equation reduces to:

$$k_i^2\mathbf{E}_i + \Big(\varepsilon_i(\omega)\frac{\omega^2}{c^2} - k_x^2\Big)\mathbf{E}_i = 0. \tag{1.16}$$

An equivalent expression is defined for the magnetic field, $\mathbf{B}$. Expanding Maxwell's curl equations, the components of the EM field give rise to two distinct solutions: TM waves (defined by E_x, E_z and B_y) and TE waves (defined by B_x, B_z and E_y). Each of them needs to be continuous across the interface, leading to:

$$\text{TM conditions}\begin{cases} E_{0,1} = E_{0,2} \\ \dfrac{k_1}{k_2} = \dfrac{\varepsilon_1}{\varepsilon_2} \end{cases} \qquad \text{TE conditions}\begin{cases} E_{0,1} = E_{0,2} \\ k_1 = k_2. \end{cases}$$

For evanescent solutions to exist on both sides of the interface, *i.e.* for $z \to \pm\infty$, k_1 and k_2 must have opposite signs: as a consequence, there are no surface waves with TE polarization. On the contrary, the TM system satisfies this condition provided that $\varepsilon_1\varepsilon_2 < 0$, which is true if one medium is a dielectric and the other one is a metal (specifically, $\varepsilon_D > 0$ and $\mathscr{Re}(\varepsilon_M) < 0$). Obviously, both k_i are real so the solutions are bounded to the interface.

Inserting the interface conditions into the wave equations and solving for k_x, the dispersion relation of the SP is finally:

$$k_x(\omega) = \pm\frac{\omega}{c}\sqrt{\frac{\varepsilon_1\varepsilon_2}{\varepsilon_1 + \varepsilon_2}}.$$

The most significant case to this work consists of $\varepsilon_{1,2}$ respectively describing vacuum and a laser-produced plasma. Hence $\varepsilon_1 = 1$, while ε_2 is the dielectric function of a free electron gas of number density n_e neutralized by an equal number of fixed ions (limit of cold plasma). Neglecting any dissipation and far from the absorption region, ε_2 is given by the expression 1.4 on page 9. In this way, the SP's dispersion relation becomes:

$$k_{\mathrm{SP}}(\omega) = \pm\frac{\omega}{c}\sqrt{\frac{1 - \omega_p^2/\omega^2}{2 - \omega_p^2/\omega^2}}. \tag{1.17}$$

This expression is valid in the linear regime, *i.e.* when the plasma electrons are non-relativistic [53], and discards any effect of non-steplike interfaces [54].

The dispersion relation 1.17 for $k_{\mathrm{SP}} > 0$ is plotted in figure 1.3b. The upper branch, characterized by $\omega > \omega_p$, corresponds to the transparency regime where high frequency modes propagate into the metal. The bound mode is limited to frequencies $\omega < \omega_p/\sqrt{2}$, while in the range $\omega_p/\sqrt{2} < \omega <$

ω_p there is no propagation since $k_{\rm SP}$ is purely imaginary. Also, the bound mode always lies below the light line $\omega = kc$, with the consequence that the SP cannot be excited by a EM wave in vacuum. Suitable phase matching techniques are discussed in the following section. Overdense plasmas are characterized by $\omega \ll \omega_p$, so that $k_{\rm SP}$ becomes close to (ω/c) and the phase velocity of the SP approaches the speed of light: this is the so-called electromagnetic limit.

In the other limit, when ω tends to $\omega_p/\sqrt{2}$, the SP's wavevector goes to infinity and the group velocity $v_g \to 0$: the mode becomes electrostatic. Typically, this mode is known as surface plasmon to be distincted from electromagnetic mode, which is called surface plasmon polariton [52]. However, in this manuscript, SP generally identifies the bound mode described by the dispersion relation 1.17. This in agreement with the fact that the electrostatic limit means $n_e = 2n_c$, whereas for overdense plasmas it is rather $n_e \gg n_c$.

The evanescent lengths across the boundary are defined for both regions $i = (1, 2)$ by $L_i = k_i^{-1}$, where k_i satisfies the wave equation $k_i^2 = k_x^2 - (\omega^2/c^2)\varepsilon_i$. By substituting the dielectric function for the vacuum-plasma interface, the results is:

$$L_1 = \left(k_{\rm SP}^2 - \frac{\omega^2}{c^2}\right)^{-1/2} \qquad\qquad L_2 = \left(k_{\rm SP}^2 - \frac{\omega^2 - \omega_p^2}{c^2}\right)^{-1/2}.$$

In the electromagnetic limit, the evanescent length in the vacuum region can extend over few λ, whereas the evanescent length inside the plasma is comparable with the skin depth 1.6 [55]. These conditions are favorable to the electron injection and acceleration, as presented in chapter 3. In the opposite limit, $k_{\rm SP} \to \infty$ so both L_i tend to 0, achieving a strong confinement across the interface. In reality, the dielectric function of a free-electron metal has also an imaginary part $\mathscr{I}m(\varepsilon_2)$ to take into account all sort of damping mechanisms affecting the wave propagation. In this way, the SP will be evanescent also along the surface, with L_x ranging from tens to hundreds of μm depending on the material and the frequency ω. Another consequences of k_x having an imaginary part is the presence of a maximum, finite wavevector in the electrostatic regime (*i.e.* $k_x \to \max[\mathscr{R}e(k_x)]$ as $\omega \to \omega_p/\sqrt{2}$), meaning that also the maximum possible confinement across the boundary will be reduced [52].

1.2.2 The coupling problem

An EM wave that impinges on the metal-dielectric interface with a generic incidence angle ϕ_i can excite a SP provided that the following phase matching conditions are satisfied:

$$\omega = \omega_{\rm SP} \qquad \text{and} \qquad k_{\parallel} = k \sin\phi_i = k_{\rm SP},$$

where ω and k are the frequency and wavevector of the EM wave (which must be P-polarized). The SP's dispersion relation plotted in figure 1.3b exemplifies that k_{SP} is always larger than $k_{\|}$, since the phase velocity of the surface wave in the metal is always smaller than the speed of light in vacuum.

Referring to figure 1.4, the gap Δk between the wavevectors of the SP, k_{SP}, and the laser $k_{\|}$ at ω must be compensated by proper coupling techniques in order to obtain the phase matching.

In the so-called prism coupling method, the light cone is bent towards the SP curve by "slowing down" the EM wave inside a material. Basically, a thin metallic layer is sandwiched between two different insulators; the EM wave transmitted through the first insulator and reaching the metallic surface has a parallel wavevector $k_{\|} = k\sqrt{\varepsilon}\sin\phi_i$ which can be high enough to match k_{SP} at the interface between the metal and the second dielectric [52]. However, only the evanescent component of the electric field that crosses the metallic layer reaches the interface, causing severe energy losses throughout the mechanism. More importantly, this method requires the three materials to have different dielectric constants: but any metal or dielectric becomes strongly conductive in the interaction with an ultra-intense laser pulse. As a consequence, the prism coupling is inadequate to study the SP excitation as soon as the laser intensity overcomes the ionization threshold.

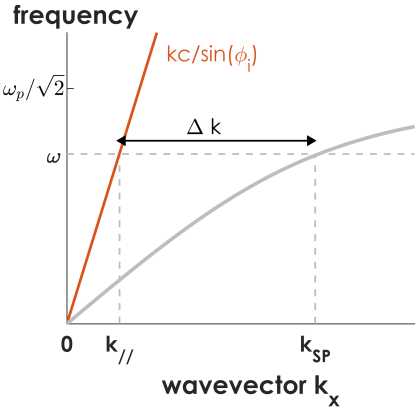

Figure 1.4: Matching the wavevector of the external EM wave and the SP requires to compensate Δk.

A most suitable technique is known as grating coupling. The interface is structured with a periodic pattern of shallow grooves (or even holes) spaced by a regular step Λ. As a consequence of the Floquet-Bloch theorem, the solutions of the wave equation take the form of plane waves modulated by a periodic function with the grating periodicity [56]. At the same time, the dispersion relation of the SP can be represented only within the first Brillouin zone $[-\pi/\Lambda, \pi/\Lambda]$, folding back the curve when k_{SP} reaches its edges. Each branch of the folded SP curve corresponds to the SP's dispersion curve k_{SP} displaced by $\Delta k = nq$, where n is an integer $(0, \pm1, ...)$ and $q = 2\pi/\Lambda$ is the grating wavevector [57]. The phase matching condition then becomes:

$$k_{\|} = k_{\text{SP}} + nq, \tag{1.18}$$

which can be satisfied for the proper combination of n and q. The folded SP's dispersion relation is shown in figure 1.5 for the choice of angles shown in the left panel: measuring positive angles from the grating normal in the counterclockwise direction, $\phi_i > 0$, so that the light line lies in the first quadrant of the $k - \omega$ plane; the SP propagates on the surface towards $-90°$, hence k_{SP} is individuated by the left branch of the dispersion relation. In the graph, this branch is folded back inside the first Brillouin zone, intercepting the light line at $\omega_{\mathrm{SP}} = \omega$ and at $k_{\mathrm{SP}} - q = k$, as in figure 1.4 (note that the phase matching condition 1.18 refers to the magnitude of the wavevectors k_{SP} and $k_{\parallel}$).

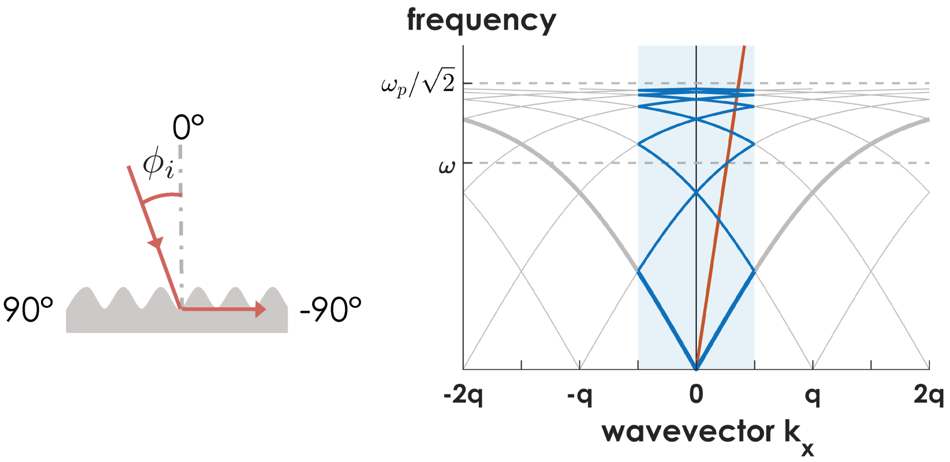

(a)

(b)

Figure 1.5: (a): geometry for the SP propagation. (b) folding of the SP's dispersion relation in the first Brillouin zone (region filled with light blue color). The light line is drawn in red, the original branches of the surface bound modes are in thick gray; the replicas $k_{\mathrm{SP}}(\omega) + nq$ are drawn with thin lines. The folded branches are underlined with blue. Matching at $\omega = \omega_{SP}$ is achieved at the intercept between the light line and the folding of the left SP's branch, which corresponds to a displacement $\Delta k = nq$ with $n = -1$ of $k_{\mathrm{SP}}(\omega)$.

Using the expression 1.17 and rearranging the phase matching condition to isolate the incidence angle, the SP occurs when

$$\sin(\phi_{\mathrm{R}}) = \pm\sqrt{\frac{1 - \omega_p^2/\omega^2}{2 - \omega_p^2/\omega^2}} + n\frac{\lambda}{\Lambda}, \tag{1.19}$$

where ϕ_{R} denotes the so-called resonant angle. For a strongly overdense plasma, the condition is further simplified:

$$\sin(\phi_{\mathrm{R}}) = \pm 1 + n\frac{\lambda}{\Lambda}. \tag{1.20}$$

The resulting formula reminds the well-known grating equation, which relates the incidence angle of a monochromatic beam to the emission angles of the diffracted orders and to the grating period:

$$\sin(\phi_i) + \sin(\phi_n) = n\frac{\lambda}{\Lambda}. \tag{1.21}$$

For the geometry chosen in figure 1.5, +1 on the right-hand side indicates the SP propagating towards −90°. In this sense, the SPs may be interpreted as diffraction orders propagating on the grating surface (naturally this description applies only in the limit of $\omega_p \gg \omega$). As a matter of fact, it can be demonstrated that SPs are particular solutions of the EM field diffracted by a grating, characterized by the confinement perpendicularly to the interface and by wavevectors that automatically satisfy the equation 1.18 [56, p. 24].

As a consequence, a natural strategy to achieve a high efficiency coupling between the external EM wave and the SP would be to choose ϕ_i and Λ such that the resonant condition 1.20 is verified for a specific $n = \tilde{n}$ and, at the same time, the grating equation 1.21 has no solutions for any $n \neq \tilde{n}$ except for the specular reflection [58]. Note that this happens only with sub-wavelength gratings (*i.e.* $\Lambda < \lambda$), giving rise to a surface wave that propagates backwards, *i.e.* $\mathbf{k}_{\mathrm{SP}} = -\mathbf{k}_{\parallel}$. In fact, assuming that ϕ_i is positive, the resonance condition gives in this case $\sin(\phi_i) + 1 = \tilde{n}\lambda/\Lambda > 1$. Inserting for example $\tilde{n} = 1$ in the grating equation 1.21, the diffraction angles are $\sin(\phi_n) = n + (n-1)\sin(\phi_i)$, which has no solutions but $n = 0$ (specular) and $n = 1$ (backward SP). On the contrary, if the resonant condition is $\sin(\phi_i) - 1 = \tilde{n}\lambda/\Lambda$, $\tilde{n}$ must be negative and $\Lambda > \lambda/2$ (for $\tilde{n} = -1$). Then, the grating equation is rewritten as $\sin(\phi_n) = n - (n+1)\sin(\phi_i)$, which has various solutions depending on n.

Sub-wavelength gratings are usually adopted in the so-called grating coupler, which is a configuration employed to study the efficiency of the SP excitation in various regimes [58]. The measurements described in this manuscript, however, always exploit the SP propagating in the same direction of the impinging laser beam (−90° in figure 1.5a). Not only sub-wavelength gratings are generally more expensive and harder to produce, but the experimental setup for the back-propagating SP would have been regrettably complex.

1.2.3 Limits of the resonance condition and of the linear theory

The resonant condition 1.20 has been employed throughout the work described in this thesis to assess the SP excitation in the relativistic regime. However, it relies on significant assumptions that are worth mentioning.

First of all, the dispersion relation of the SP (equation 1.17) derives from a linear treatment of the optical response of the laser-generated plasma. Moving to the regime of ultra-high laser intensity requires to deal with the non-linear motion of the relativistic plasma electrons, with the result that the dielectric function 1.4 depends on the amplitude EM field itself [2]. Considering the temporal evolution of the plasma density under the effect of the laser ponderomotive force is also expected to modify both the SP's wavevector (k_x in the wave equation 1.16) and both evanescent lengths across the interface [53].

Effects of finite temperature or mild inhomogeneities on the surface also modify the dispersion relation according to $k_{\mathrm{SP}}(\omega) = k_{\mathrm{SP}}^{\mathrm{lin}}(1-f)$, where $k_{\mathrm{SP}}^{\mathrm{lin}}$ is the cold plasma, linear dispersion relation 1.17 and f is either a correction $\propto T_e/c$, with T_e the thermal electron velocity, or $\propto \partial n_e(z)/\partial z$, where $n_e(z)$ describes an inhomogeneous density profile along the perpendicular to the interface [54].

Further on, the phase-matching condition has been fulfilled resorting to a periodically modulated surface without taking into account how this choice affects the SP's dispersion relation [58]. A detailed treatment of the boundary conditions at the grating surface finds the EM fields to be expressed as a plane wave with the same periodicity of the grating and modulated by a term which is function of the boundary shape [56, p. 19]. This approach relies on the assumption that the groove depth d is small enough to be considered as a perturbation to the flat interface (*i.e.* $d \ll \Lambda$). Then, it is possible to demonstrate that the correction to the SP's dispersion relation is infinitesimal of (d^2/Λ^2). A consequent shift of the SP's frequency might require to adjust the incident angle ϕ_i in order to still satisfy the resonant condition 1.19. Beyond this assumption, a numerical treatment of the boundary conditions of Maxwell's equations at the grating interface allows to show that grooves deeper than the grating period lead to the formation of large band gaps in the SP's dispersion relation [59]. Also in this case, however, the approach is entirely non-relativistic. Moving to the regime of high fields, the groove depth might represent a crucial parameter for optimizing the SP excitation, as it will be investigated numerically in chapter 3. In particular, as the fully-ionized target is expected to rapidly expands, deeper grooves might be needed to preserve the periodical modulation. The appearance of band gaps could be also revealed if, as soon as the groove depth is increased, the matching with the laser frequency is suppressed.

Interesting effects lie also on the laser dependency of the resonance condition. The expression 1.20 predicts a unique incident angle for the successful excitation of the SP, ϕ_{R}, yet there is both experimental and numerical evidence of surface waves occurring within some angles from the resonant one. As investigated in [60], such *resonance width* can be provoked by the curvature of the laser wavefronts and by its spectral bandwidth. As a consequence of the first effect, the local incidence angle defined by the wavefronts and the grating normal varies along the transverse size of the laser pulse, allowing to verify the resonance condition even for $\phi_i \neq \phi_{\mathrm{R}}$. The angular spread of the pulse wavefronts is of the order of $\sim \lambda/w_0$, where w_0 is the beam waist, hence this effect is more pronounced for smaller focal spots.

Secondly, the laser bandwidth affects λ in formula 1.20: shorter pulses may excite the SP at $\phi_i \neq \phi_{\mathrm{R}}$ because their bandwidth contains the proper λ to fulfill the resonance condition.

A final remark about the resonance condition concerns the efficiency of SP excitation. Indeed, equation 1.19 does not give any clue as to how much energy of the impinging EM wave is expected to be yielded to the surface wave. Besides reducing the number of diffraction orders as explained in the previous section, tailoring the grating period is far from achieving the purpose, and great effort is spent in the understanding and optimization of other grating parameters to increase the coupling efficiency. Generally, the best coupling is obtained when the dissipation inside the conductor is matched to the radiative loss in the grating [58]. However, these elements depend not-trivially on numerous factors like the grating profile, the groove depth, and not ultimately the roughness of the surface, so that the grating efficiency is usually addressed experimentally. In the same spirit, the measurements presented in this work deal with a collection of different gratings to explore which characteristics might be relevant to SPs in the relativistic regime.

1.2.4 Examples of plasmonic applications

Surface Plasmons are a resourceful means to study the interaction between light and matter and, as such, they come with plenty of applications. This section picks into the teeming domain of Plasmonics to hint to the great variety of phenomena and applications where SPs are involved [61].

As already introduced in the theoretical description of SPs, strong confinement of the EM field can be achieved across a surface by properly choosing the SP frequency and dielectric properties of the material [6]. In this way, the usual diffraction limit $\propto \lambda/2$ is easily overcome, allowing the natural development of *plasmonic concentrators* and their applications in imaging techniques with high spatial resolution (*e.g.* near field optical microscopy), plasmon-enhanced photodetectors, modulators [7], miniaturized electronic circuits [62] and long-distance waveguides [63].

Enhanced field intensities are achieved via nano-focusing [64, 65] and light confinement in metallic structures with sub-wavelength size, giving access to different nonlinear phenomena (*e.g.* harmonic generation [66]). With this regard, increased fluorescence [67] and Raman scattering [68] signals induced by resonating molecules in the locally-enhanced EM field are successfully employed to design biosensors [69] and to temporally resolve the molecular dynamics [70]. Matching SPs to different materials is also studied as a way to increase the absorption efficiency of different devices (*e.g.* solar cells [71], graphene p-n junctions [72]).

With regard to the domain of laser-solid interaction, exploratory tests of enhanced laser absorption (up to 93% of the incident light) and boosted ion acceleration (×2 increment of the cutoff energy on the laser-irradiated half-space) have been reported for weak laser intensities, $\sim 10^{15}$ W/cm^2 [45, 46]. Both these works exploit sub-wavelength gratings to excite the SPs with the minimum energy coupled to high diffraction orders; the SP-related absorption is monitored by inferring the fast electron temperature 1.12 from the Bremmstrahlung X-rays emission. Fewer studies focused on electron acceleration in the same conditions, with fairly modest results (presented in chapter 3).

Stepping to the relativistic regime is quite a challenging goal. As anticipated in the previous discussion, high intensity laser fields simply ionize any target, preventing on one side to employ schemes that rely on different dielectric materials, and on the other to ensure the survival of micro-structured surfaces, which may be washed out even by the long pedestal preceding the most intense laser pulse (as explained in the following chapter). Luckily the experimental work presented in this manuscript accounts for a different scenario: ultra-high contrast laser pulses allow for resonant excitation of relativistic SPs, resulting in higher laser absorption, strong electron acceleration and enhanced high order harmonic generation[4]. The issue of target survival to high laser intensities is dealt with in the next chapter, while striking evidence of SPs excitation in the relativistic regime is given in chapter 3 and 4. Although far from the most conventional plasmonic applications, these findings surely usher in the realistic opportunity to accede and explore *Relastivistic Plamonics.*

---

[4] It is worth noticing that SPs have been observed also in experiments with underdense (*i.e.* $\omega_p \ll \omega$) plasmas [73]: in this case, the ponderomotive force of a relativistically-intense laser pulse expels the electrons from the regions of higher intensity and creates a cavitated channel. Its walls are steep enough to support SP propagation. Note that in this case the SP is excited by the hosing of the laser pulse (see [74] and references therein). SP excitation by parametric instabilities can also occur in overdense plasmas [75] and lead to the rippling of the plasma surface [76] with possible detriment to the ion acceleration.

Chapter 2

Experimental and numerical tools

The main results of this work were obtained throughout several experimental campaigns performed at the Saclay Laser-matter Interaction Center Facility (SLIC) of CEA Saclay (Gif sur Yvette, France). This chapter is therefore devoted to the description of the laser installation, with particular attention to the most relevant parameters to laser-solid interaction experiments, especially the laser contrast. The setup and the list of all the different targets used in the experiments are provided as well. The last part is reserved to briefly introduce Particle-In-Cell codes and to present the main features of PICCANTE, which was employed in the numerical simulations performed alongside the experimental activity.

2.1 The laser system UHI100

UHI100 (Ultra-Haute Intensité) is a 100 TW chirped pulse amplification laser system located at CEA Saclay. With 2.5 J, 25 fs laser pulses and a repetition rate up to 10 Hz, the installation is devoted to highly intense laser-matter interaction experiments, with dedicated experimental areas for both solid and gaseous targets.

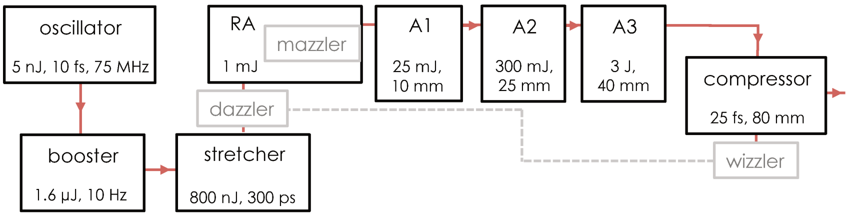

Figure 2.1: Sketch of the laser UHI100. Each element shows the relevant parameters of the output (duration, energy, repetition rate, diameter). RA indicates the regenerative amplification, followed by the other amplification (A) stages.

Figure 2.1 shows the laser layout. The front end is a Titanium:Sapphire mode-locked Synergy oscillator, delivering a train of $\sim$ 10 fs, 5 nJ pulses at 75 MHz repetition rate. The spectrum is centered at 796 nm with a bandwidth (FWHM) of 137 nm. The following element is the booster, a Ti:Sa multi-pass amplifier which increases the seed energy up to 1.6 μJ; the repetition rate of the output is lowered down to 10 Hz by a Pockels cell. The beam then passes through an Offner-type stretcher: a grating is arranged to split the spectral components of the pulse and to introduce a positive chirp (*i.e.* low-frequency components travel a shorter path than the high-frequency ones), so that the pulse duration is extended to a few hundreds of ps; at the same time, optical losses determine a 50% diminution of the pulse energy.

The subsequent amplification chain consists of four multi-pass stages, each one including a Ti:Sa crystal pumped by frequency-doubled Nd:YAG lasers. The regenerative amplification (RA) develops inside a confocal cavity controlled by two Pockels cells, where the pulse energy raises to 1 mJ. Before acceding to the following stage, the beam is sent to a pulse cleaner, *i.e.* another Pockels cell which removes undesired pre-pulses on the ns time scale. The Amplified Spontaneous Emission (ASE) is also reduced with numerous polarizers along the laser propagation. The next amplification stages (A1, A2, A3) are implemented with a bow-tie geometry; the beam diameter is duly increased at each stage to match the size of the upcoming crystals. The energy builds up to 25 mJ (A1), 300 mJ (A2), and finally to 3 J (A3). The last stage also includes a cryogenic cooling system to prevent thermal lensing and the damaging of the crystal.

At the exit of the amplification chain, the beam is further enlarged to 80 mm of diameter. The last element of the laser system is the compressor, where the pulse is brought back to 25 fs of duration by means of two parallel gratings that compensate the dispersion introduced by the stretcher. This stage implies another energy loss of $\sim$ 35%.

Three more devices, indicated in gray in figure 2.1, control the spectral phase and amplitude of the laser pulse. The Dazzler is an acousto-optic dispersive filter which corrects the spectral phase in order to achieve the shortest pulse; it is operated in a feedback loop with the Wizzler, which measures the temporal duration of the pulse at the output of the compressor. The Mazzler, located inside the cavity of the regenerative amplification, compensates the gain narrowing effect induced by the λ-dependent amplification of the crystals [77]. This acousto-optic modulator arranges the spectral amplitude of the laser pulse to achieve a flat gain on the overall bandwidth. In this way, the final spectrum has a super Gaussian profile, with 80 nm FWHM bandwidth.

2.2 The experimental area salle chaude 1

The beam path after the compressor is shown in figure 2.2. The laser propagates through a Double Plasma Mirror (DPM), a device conceived to increase the temporal contrast. Then, it is reflected by the deformable mirror, an adaptive optic whose purpose is to correct the optical aberrations of the beam. After correction, the laser is sent inside the interaction chamber by one last dielectric mirror (reflectivity $r > 99\%$ for $\lambda = 800$ nm and 45° incidence).

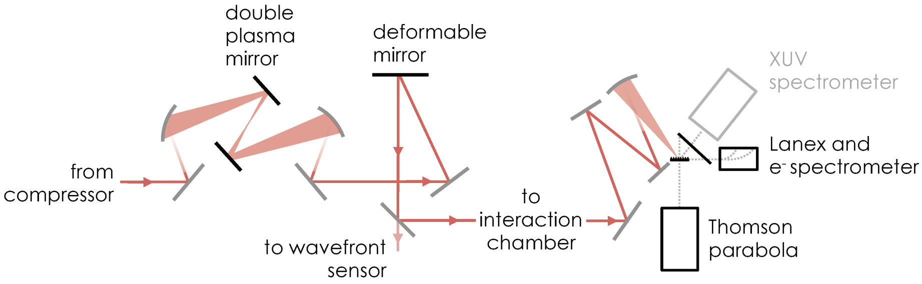

Figure 2.2: The schematic layout of *salle chaude 1*.

In the interaction chamber, the collimated beam is reflected by three protected Silver mirrors (average reflectivity $\sim 97.5\%$) before being focused at the chamber center by a $f = 300$ mm, 14° off-axis parabolic mirror. In order to supervise the focal spot optimization, a motorized 1-inch Silver mirror can intercept the laser beam before arriving at the focus position, and send it through a 10X microscope objective to a 12-bit Guppy PRO CCD camera. A typical focal spot recorded during the experimental campaign is shown in figure 2.3a.

When approximating the laser field with a Gaussian profile, the beam radius where the intensity drops to $1/e^2$ of its peak value is defined at focus by the beam waist w_0, which is given by

$$w_0 = 0.85\lambda\frac{f}{D}, \tag{2.1}$$

where D is the beam diameter (80 mm). This expression comes from the fair approximation of the central lobe of the Airy disk with a gaussian profile. An area containing 95% of the beam energy would rather be defined by $r_{95\%} = 1.2\lambda f/D$, where $r_{95\%}$ is $\sqrt{2}w_0$. Substitution of the UHI100 parameters results in $w_0 = 2.5$ μm and $r_{95\%} = 3.6$ μm. Still, a typical focal spot measures 4.6 μm FWHM (*i.e.* $w_0 = 3.9$ μm), as shown in figure 2.3a. This indicates that the Gaussian approximation cannot truly represent the beam profile of UHI100, which is actually top-hat. The M^2 factor (or beam quality factor) partially accounts for this discrepancy: it is defined by the product of the beam waist and the beam divergence, divided by λ/π (*i.e.* the beam parameter product for a diffraction-limited Gaussian beam). Being the measured M^2 factor for UHI100 equal to 1.2, the effective beam waist becomes M^2 times w_0, which is ~ 3 μm. In the end, despite the deformable mirror further improves the beam wavefront, residual optical aberrations still cause the focal spot to be larger than the M^2-times diffraction limit. Also the Rayleigh length z_R, which represents the distance from waist where the beam radius has increased by a factor of $\sqrt{2}$, is modified by the beam quality factor as:

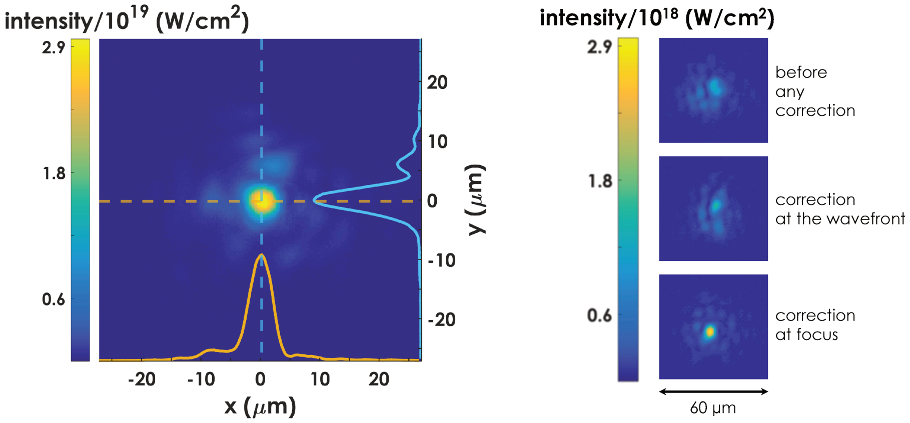

(a) Full energy beam (3 J)

(b) Attenuated beam (0.3 J)

Figure 2.3: Pictures of the experimental focal spot. The typical profile and size after the wavefront optimization at full beam energy are shown in (a): both FWHM measure ~ 4.5 μm and the peak intensity is $\sim 3 \times 10^{19}$ W/cm^2. In (b), the evolution of the focal spot during the deformable mirror loop: before correction, with correction at the wavefront sensor and after correction at focus. The lower intensity indicated in the color bar is the result of the loop carried out at low energy (~ 300 mJ before compression).

$$z_R = \frac{1}{M^2}\frac{\pi w_0^2}{\lambda}. \tag{2.2}$$

As a consequence, the farther the beam is from the Gaussian approximation, the faster it diverges at a given beam radius. For UHI100, the effective Rayleigh length is ~ 60 μm.

Considering all the energy losses caused by the compressor, the double plasma mirror and the optical components, the target is finally irradiated by a ~ 700 mJ laser pulse. Taking into account the $1/e^2$ spot size and the $1/e^2$ pulse duration, the peak intensity ranges from ~ 1.8 to $\sim 3.4 \times 10^{19}$ W/cm^2 depending on the incidence angle.

2.2.1 The deformable mirror

Achieving the highest laser intensity requires to accurately control both the spectral and spatial phase of the laser pulse. While the first one is cared for by the Dazzler along the laser chain, the spatial phase is optimized by an adaptive optic system which removes most of the wavefront aberrations introduced by nonlinear effects and optical components along the beam propagation to the chamber center, allowing to obtain nearly diffraction-limited focal spots [78]. The principle of the wavefront correction is illustrated in figure 2.4. In the first place, the 1% leak from the dielectric mirror is sent to a Shack-Hartmann wavefront sensor, which uses an array of micro-lenses to measure the beam aberrations with $\lambda/150$ accuracy: for a planar

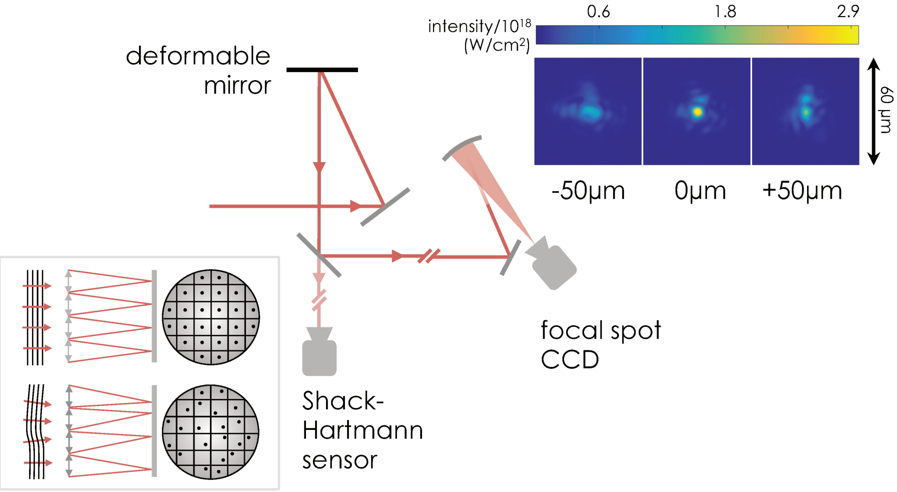

Figure 2.4: Scheme of the wavefront correction loop: the leak is analyzed by the the wavefront sensor, which in turn instructs the deformable mirror to adapt its surface. Residual aberrations downstream of the mirror are measured by the focal spot imaging system and corrected by a Phase Retrieval algorithm. Insets show the principle of the Shack-Hartmann wavefront sensor and images of the beam transverse profile recorded at three positions along the focal axis (0 and ±50 μm with respect to focus) at low laser energy.

wavefront, each micro-lens focuses the beam along its optical axis on a CMOS sensor, forming a regular grid of spots on the detector; on the contrary, a distorted wavefront is deviated on the detector depending on the phase tilt it possesses at the entrance of the micro-lens, resulting in an irregular grid of spots. The measurement of the displacement of each spot from the micro-lenses centers allows to reconstruct the aberrations of the wavefront [79]. The dielectric surface of the deformable mirror (ILAO Star, by Imagine Optic), which is controlled by a matrix of 37 mechanical actuators [80], is consequently modified to compensate the measured aberrations. The loop from wavefront measurement to deformable mirror reshaping is repeated until the Strehl ratio (*i.e.* the ratio between the intensity at the center of the aberrated image and the intensity from an ideal source diffracted by the system's aperture) sets around 80%. Next, all the aberrations introduced by the optical elements downstream of the wavefront sensor are analyzed by a Phase Retrieval algorithm [81] which infers the laser wavefront from the images of the focal spot: the appropriate correction is sent once again to the deformable mirror.

An example of the focal spot development along these steps is shown in figure 2.3b: from the uncorrected wavefront before the deformable mirror to the focal spot after the Phase Retrieval algorithm, the size is reduced from 6.5 to 4.5 μm (FWHM), corresponding to an intensity gain of ~ 2. The procedure described so far is always performed when averaging over a lot of laser shots recorded at 10 Hz frequency and low intensity, *i.e.* bypassing the last amplification stages, in order to reduce shot-to-shot fluctuations that would hamper the wavefront measurement and the reconstruction algorithm. However, in the course of the experiments described in this manuscript it became evident that corrections applied in the low power mode did not ensure the same quality of the focal spot at maximum energy, as shown in figure 2.3. Thus, the last phase of focal spot optimization consists in repeating both the aberration measurements and corrections, but in a single shot, high power mode, provided attenuating the laser beam with high optical densities. The final focal spot, regularly achieved over the experimental campaigns, appears as in figure 2.3a.

2.2.2 The Double Plasma Mirror

The laser temporal contrast is defined as the ratio between the peak intensity of the main pulse and its background at a certain time t. Laser-solid interaction experiments at ultra-high intensity usually require to accurately control this parameter, as many physical mechanisms become efficient, or even accessible, only for steep plasma density gradients (*i.e.* $L \ll \lambda$, with L defined in section 1.1.2). These processes, such as harmonic generation [82] or proton acceleration [83, 84], closely depend on the solid target ionization, heating and, ultimately, deformation. For a peak intensity of 10^{19} W/cm^2, a typical laser contrast of 10^8 tens of ps before the main laser pulse means irradiating the target with 10^{11} W/cm^2, which is already above the ionization threshold of many dielectric materials [8]: the plasma would then expand into vacuum, altering the interaction conditions for the main laser pulse.

A poor laser contrast is intrinsic to CPA laser systems, where a temporal pedestal due to Amplified Spontaneous Emission (ASE) is formed on the ns time scale, and pre-pulses on the sub-100 ps time scale originate from misalignment of the optical components in the laser chain, multiple reflections, flaws in the Pockels cells operation or in the compression stage. Finally, scattering of the laser light produced in the pulse stretcher leads to an exponentially-rising pedestal within 10 ps of the main pulse, which is known as coherent contrast region [85]. Electro-optic modulators typically remove ns-scale pre-prepulses, as it happens along the UHI100 laser chain after the regenerative amplification. Additionally, the booster includes a saturable absorber, which reduces the intensity ASE pedestal by a factor of $\sim 10^{-8}$ in the ps times scale (compare figure 2.5 here below).

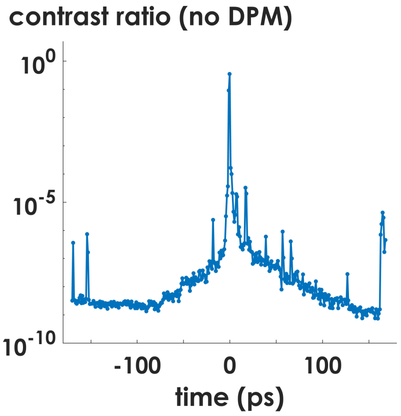

Figure 2.5: Measured contrast on UHI100 after the saturable absorber (and without DPM).

Self-induced plasma shuttering [86], or plasma mirror, is a well-established technique to further increase the laser contrast. The laser beam is focalised on an anti-reflective dielectric material, whose conduction electrons are gradually excited with the beam intensity increasing with time. The beam is transmitted across the material as long as the electron density does not exceed the critical density at the laser wavelength (n_c in equation 1.1), whereupon it is reflected. The fluence of the incoming beam on the dielectric surface sets the plasma mirror trigger time, in order to have only the main pulse reflected. This also inhibits plasma expansion, preventing detrimental distortion of the wavefront. Reflectivity up to 70% [82] and a contrast enhancement of $\sim 10^2$ are achieved for S-polarized laser beams with duration below ~ 500 fs, with little dependence on the incoming fluence in a range between 50 and 500 J/cm^2 [87].

The experimental area *salle chaude 1* is equipped with a double plasma mirror (DPM), composed by two BK7 bars with an anti-reflecting coating ($r \sim 0.3\%$ at 800 nm) arranged in a confocal setup (figure 2.2). A motorized stage shifts the DPM to provide a fresh surface after each laser shot, so that ~ 800 shots are easily collected before replacing the BK7 bars. When the laser beam is focused halfway between the two bars, both the overall energy transmission (50%) and the contrast gain (10^4) are maximized [8].

Figure 2.5 reports the initial contrast of UHI100 after the saturable absorber, measured with a third order correlator (SEQUOIA, by Amplitude Technologies) having a dynamic range of $\sim 10^{10}$. The curve shows that between 200 and 50 ps before the pulse peak, the temporal contrast is higher than 10^8, decreasing to $\sim 10^7$ at 10 ps. A measurement after the DPM has only been performed in 2007, before the upgrade of the laser system to 100 TW [88]. However, numerical simulations [87] suggest that the contrast enhancement reported at 10 TW is expected to be maintained also in correspondence with the higher pulse fluence achieved by the 100 TW laser system. Hence, the temporal contrast attained after the DPM is expected to be of the order of $\sim 10^{12} \div 10^{11}$ on the same time scale of figure 2.5.

2.2.3 Diagnostics in the interaction chamber

The optical elements for the laser transport and focalization, and the focal spot and target imaging systems, are confined within a small sector of the interaction chamber, so that most of the space is available for the diagnostics. Different ones are implemented to investigate electron, ion or XUV emissions, and they will be thoroughly described in the corresponding chapters. Nevertheless, a brief presentation of their arrangement is given here, to complete the description of the experimental setup.

A scintillating Lanex screen and an electron spectrometer are mounted on a powered platform which rotates around the chamber center. The Lanex screen is tilted by 45° with respect to the target surface in order to detect the electron emission from the target tangent to its normal. The electron spectrometer is aligned behind the Lanex and it is designed to bend the electron trajectories by 90° in the energy range $1.5 \div 16$ MeV: dispersed electrons are then imaged on another piece of Lanex screen. Two cameras, fixed outside the interaction chamber, record the Lanex emission from both the 45° screen and the electron spectrometer. Ion detection is provided by a Thomson parabola, where a micro-channel plate (MCP) coupled to a phosphor screen is imaged by a 12-bit CCD camera. In a very compact arrangement, the whole instrument is installed on a circular rail, where it can shuffle via an externally-motorized timing belt, and aligned along the normal direction of the target rear surface. In this way, both electron and ion diagnostics can be displaced around the target by remote control without opening the interaction chamber, reducing the time required to fit the experimental configuration to different incidence angles, and ensuring a stable setup. The XUV spectrometer, also designed with a MCP and a phosphor screen but with an external CCD, is the only diagnostic too heavy and cumbersome to be placed on a motorized stage: its position is therefore manually set and modified each time the incidence angle is changed.

Motorized rails and platforms allowed to scan the laser-grating interaction for incidence angles spanning from 10 to 60° within single days. However, the signal measured by fixed cameras is strongly affected by geometrical parameters such as the collection angle, which in turn depends on the position of the rotating platforms. Starting from reference pictures taken for each position of the rotating platforms, a correction factor was calculated for all the different configurations: details of this calculation are described in appendix A.

2.3 Targets

The experimental investigation covered not only the basic distinction between gratings and flat targets, but also many different grating parameters in order to fully explore how different geometries could affect the SP excitation and the coupling with the incident laser pulse. Among the grating targets, two families are easily identified: thin and solid gratings. *Thin* gratings have a sinusoidal profile, heat-embossed with a Nickel master on 13 μm thick, commercially available Mylar foils. They were produced at the Czech Technical University of Prague (Czech Republic) and by the company HoloPlus, also located in Prague. A picture of a thin grating target obtained by atomic force microscopy is shown in figure 2.6a, together with a measurement of its period. *Solid* gratings were bought from the company EdmundOptics.

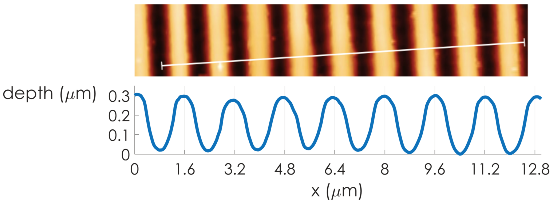

(a) AFM scan of a thin grating. The period 2λ (*i.e.* 1.6 μm) and the depth ($\sim$ 300 nm) clearly appear from the image lineout.

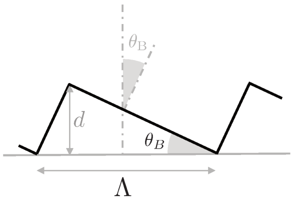

(b) Profile of a blazed grating.

They are produced by depositing a substrate of epoxy-coated float glass over an Aluminum-coated ruled master. The thickness of the protective layers is ~ 1 μm and ~ 50 μm for, respectively, the Aluminum and epoxy coatings, whereas the substrate is 9.5 mm thick. All solid gratings have a sawtooth profile with a 90° apex angle. The angle between the longer side of the sawtooth profile and the substrate is known as blaze angle, θ_B. Consequently, it corresponds to the angle between the substrate normal and the facet normal, as shown in figure 2.6b. The grating depth, d, is related to the blaze angle and to the grating period Λ by the simple relation $d = \Lambda \cos\theta_\mathrm{B} \sin\theta_\mathrm{B}$.

Thin gratings have different periods and depths, as shown in table 2.1a. They were specifically chosen to satisfy the resonance condition for SP excitation (equation 1.20 on page 22) at different laser incidence angles. Their thickness also allows for proton detection at the rear surface of the target. On the other hand, solid gratings share the same period (*i.e.* 2λ, for a resonant angle of 30°), but have different blaze angles, as listed in table 2.1b. These gratings were chosen to assess geometrical effects on electron acceleration. In order to elucidate the role of the Aluminum coating on the target efficiency, also a thin sinusoidal grating was produced on a commercially-available, 12 μm thick Aluminized Mylar foil.

Name	period Λ (λ)	depth d (nm)
G15	1.35	170
G30	2.00	290
G45	3.41	370
G30$_{\mathrm{Alu}}$	2.00	280

(a) thin gratings

Name	blaze angle θ_{B} (°)	depth d (nm)
SG4	4.18	121
SG6	6.33	183
SG13	13.00	365
SG22	22.01	579
SG28	28.41	698

(b) solid gratings

Table 2.1: List of grating types and parameters. Thin gratings (a) have a 13 μm thick Mylar substrate, and sinusoidal profile. All solid gratings (b) have a 2λ period and 9.5 mm thick Aluminized-glass substrate.

Flat targets consist of the same Mylar foils were thin gratings were embossed. In the following of the manuscript, flat targets might be indicated by F, while thin gratings by G followed by the resonance angle (*e.g.* G30). For solid gratings, the abbreviation will be SG followed by the blaze angle (*e.g.* SG13).

2.3.1 Note on the grating efficiency

The percentage of monochromatic light diffracted into a specific order by a diffraction grating is known as absolute efficiency. This one depends on many parameters, including the power and polarization of the incident light, the incidence angle, the refraction order of the grating material, the groove spacing and, ultimately, their profile. The study of the energy distribution into the different spectral orders digs into the resolution of the Maxwell equations on corrugated surfaces and the implementation of accurate boundary conditions typically relies on numerical treatments [89, 90]. Nevertheless, it is worth describing some basic notions to outline the expected behavior of the gratings employed in the experiment.

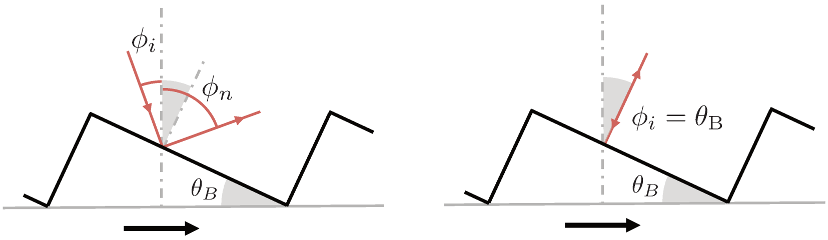

(a) Generic incidence angle to maximize the n^th order

(b) Littrow configuration

Figure 2.6: Diffraction at a blazed grating. In (a), the facet normal bisects the angle between the ϕ_i and ϕ_n, satisfying the blaze condition. In this way, the n^th order efficiency is maximum. With the Littrow configuration (b), the incident ray is perpendicular to the facet surface.

Blazed gratings are specially designed to maximize the energy concentrated into a specific diffraction order for a specific wavelength. This happens when the chosen n^th order corresponds to the specular reflection of the incident light with respect to the facet normal, as shown in figure 2.6a. With the same convention used in figure 1.5a on page 22, angles are measured with respect to the substrate normal (or grating normal), and the counterclockwise direction is positive. Hence, the so-called *blaze condition* implies that $(\phi_i + \phi_n) = 2\theta_\mathrm{B}$, so that the grating equation 1.21 reads:

$$2 \sin \theta_\mathrm{B} \cos(\phi_i - \theta_\mathrm{B}) = n \frac{\lambda}{\Lambda}. \tag{2.3}$$

For fixed ϕ_i, θ_B, Λ and n, this expression defines the blaze wavelength λ_B where the efficiency is maximized [91]. However, blazed gratings are generally manufactured and characterized in a special configuration where the incidence angle and the diffraction angle overlap. This is known as Littrow configuration, and for a blazed profile it implies $\phi_i = \theta_\mathrm{B}$. As figure 2.6b illustrates, in this case the incident light is perpendicular to the grating facet. From the expression 2.3 it follows that

$$2 \sin \theta_\mathrm{B} = n \frac{\lambda_\mathrm{B,\,Littrow}}{\Lambda}, \tag{2.4}$$

where the blaze wavelength in the Littrow configuration has been indicated with $\lambda_\mathrm{B,\,Littrow}$.

The grating efficiency is typically measured in the Littrow configuration and reported as a function of the wavelength for the first diffraction order ($|n| = 1$). The maximum absolute efficiency always occurs when $\lambda = \lambda_\mathrm{B,\,Littrow}$. The peak of the curve decreases and shifts towards shorter wavelengths for higher $|n|$, as indicated by the formula 2.3. Also departing from the Littrow configuration, *i.e.* using $\phi_i \neq \theta_\text{B}$, generally reduces the efficiency as $(\phi_i + \phi_n)$ increases; this effect depends on the blaze angle θ_B and it is more significant for wavelengths far from λ_B [92]. As a general rule of thumb, for blazed grating with $\Lambda \geq 2\lambda$ the efficiency drops by 50% outside the range $[0.6, 1.5]\lambda_\text{B}$.

The blazed gratings listed in 2.1b report an absolute efficiency of about 70% measured for $n = 1$ in the Littrow configuration, with incident unpolarized light. This value might slightly increase with light polarized perpendicularly to the grating grooves [89]. Table 2.2 indicates the blaze wavelength $\lambda_\text{B, Littrow}$ of the solid gratings employed in this work, together with the absolute efficiency at $\lambda = 800$ nm (*i.e.* the laser wavelength) deduced by the efficiency curves. It is evident that departing from the blaze wavelength has the most unfavorable effect on the grating efficiency, despite the first diffraction order corresponds to the tangent direction where the surface wave is expected to propagate. Only the SG13 is optimized for the laser wavelength, although a smaller efficiency has to be considered because of the departing from the Littrow configuration. It can be also noticed that the laser wavelength becomes the blaze wavelength for the SG28 at $n = 2$; hence, the maximum optical power is backscattered to $\phi_{n=2} = 28°$ and does not contribute to the diffraction order propagating in the tangent direction.

Name	blaze wavelength λ_B (nm)	absolute efficiency at 800 nm e (%)
SG4	250	15
SG6	400	25
SG13	750	65
SG22	1250	25
SG28	1600	5

Table 2.2: The blaze wavelength corresponds to the peak efficiency of solid blazed gratings. The efficiency at the laser wavelength 800 nm is obtained by the efficiency curves available with the technical specifications.

One further configuration is tested with the SG13. Because the sawtooth profile is asymmetric, the orientation of the blazed grating also affects its efficiency. The proper orientation to achieve the maximum efficiency is when the blaze angle points to the same side of the specularly reflected light, measured with respect to the grating normal. Obviously, reversing the grating orientation does not displace the diffraction orders but only reduces the grating efficiency [90]. Usually, blazed gratings are marked with an arrow that indicates the direction of blaze, as indicated in figure 2.6.

To conclude, sinusoidal gratings typically have smaller efficiencies with respect to blazed profiles. The efficiency curves are grouped depending on the modulation depth d/Λ: the thin gratings presented in table 2.1a belong to the low modulation range ($0.05 < d/\Lambda < 0.2$), where the efficiency is around 50% less than what is achieved with a blazed grating at the proper blaze wavelength [92]. Deeper gratings reach a 100% absolute efficiency provided that λ/Λ is higher than 0.65. These results are always obtained in the Littrow configuration, that requires $\phi_i \sim 22°$, $14°$ and $8°$ for the first diffraction order and, respectively, the groove spacing of each thin grating.

These estimates may be regarded as general guidelines to understand the experimental results. However, since the grating targets described in this work differ in material, the explicit comparison between sinusoidal and blazed profile could produce different results.

2.3.2 Target mounting and imaging

Thin targets are manually pasted with spray glue on small Aluminum slabs, where a matrix of 6×5 holes was drilled in order to allow for proton detection at the rear surface of the target. Up to three slabs can be allocated in a metallic holder to place targets in the interaction chamber; a similar one is employed to mount solid gratings in larger slots. Holders are then fixed on a motorized stage providing (x, y, z) translations, $(x - z)$ and $(y - z)$ rotations: in this way, a fresh target is set up before each laser shot. With this experimental arrangement, up to 200 shots can be gathered before opening the interaction chamber for target replacement. Rotation around the y-axis allows to easily modify the incidence angle of the laser pulse with respect to the normal to the target surface.

The interaction region at the center of the chamber is always inspected with an imaging system, whose optical path is adjusted according to the experimental configuration in use, as shown in figure 2.7. During the investigation of large incidence angles, a 1-lens system is installed on the same line as the focal spot monitoring system: a combination of motorized stages allows to interchange the optical components to swap between one another. The configuration for small incidence angles requires a more challenging setup, as there is no space available between the parabolic mirror and the electron diagnostics. In this case, a 2-lens imaging system is employed: the optical path is uplifted by tilting the lenses and arrives in a region of the interaction chamber which is free from any other encumbrance. In both imaging systems, the optical magnification is kept between 1.5 and 2 by a proper choice of lenses and the image is recorded by a triggered 12-bit, Mako G-030 CMOS camera protected with a BG-39 bandpass filter.

Target imaging is crucial not only to monitor the target surface status before and after the laser shot, but also to check its position in the chamber. In fact, target misalignment would result in wrong incidence angles or focalization of the laser pulse, impairing the study of the conditions for resonant SP excitation. Besides, a 5 mW, green laser pointer reflecting on a

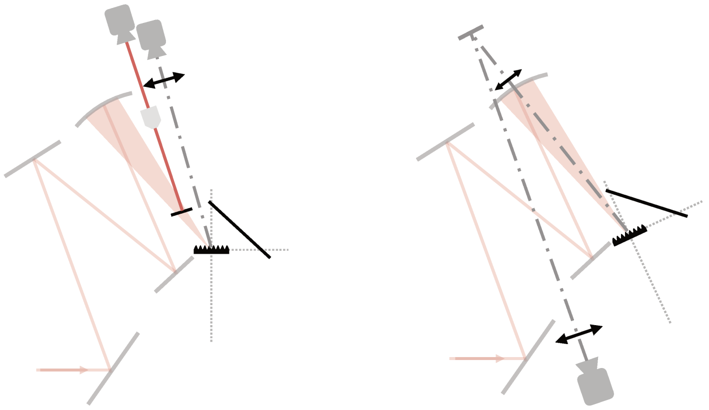

(a) Large incidence angles

(b) Small incidence angles

Figure 2.7: Optical paths for the target imaging systems. (a) also includes the monitoring line for the focal spot, with the small intercepting mirror and the microscope objective. Arrows indicate lenses.

glass microscope slide attached to the target holder is employed to align all the diagnostics: hence, target misplacing would also spoil the data collection. In order to overcome these risks, target alignment is ensured by using two green laser pointers that cross with quite a large angle at the chamber center, in the same position where the laser pulse is focused. In this way, any mistaken position along the focal axis would immediately become apparent as the separation of the two green laser spots on the target surface. This technique allowed to establish the target position with 15 μm accuracy along the focal axis (15 $\mu\text{m} < z_\text{R}$) throughout all the experimental campaigns.

2.4 Particle-In-Cell simulations

Numerical simulations are of paramount importance in the study of plasma physics, where a lot of non-linear phenomena take place in many complex scenarios. In the context of short laser pulses interacting with highly dense plasmas, Particle-In-Cell (PIC) codes [93] are best-suited for describing the plasma dynamics with a kinetic approach. For a collisionless fully-ionized plasma, the cornerstone of such kinetic description is the relativistic Vlasov equation:

$$\partial_t f_s + \mathbf{v} \cdot \nabla_\mathbf{r} f_s + q_s \Big(\mathbf{E} + \frac{1}{c} \mathbf{v} \times \mathbf{B} \Big) \cdot \nabla_\mathbf{p} f_s = 0,$$

where $f_s = f_s(\mathbf{r}, \mathbf{p}, t)$ represents the distribution function of the particle species s and $\mathbf{v}_s = (\mathbf{p}_s / m_s \gamma_s)$. The electromagnetic fields $\mathbf{E}$, $\mathbf{B}$ evolve according to the Maxwell equations, where the source terms depend in turn on the plasma particles themselves:

$$\rho = \sum_s q_s \int f_s \mathrm{d}^3p, \qquad \mathbf{J} = \sum_s q_s \int \mathbf{v} f_s \mathrm{d}^3p.$$

In a numerical approach, the self-consistent Vlasov-Maxwell system is solved on a discretized spatial grid. In particular, a PIC code resorts to sample the distribution function with a finite number N_p of charged macro-particles, with the advantage of reducing the computational effort. Hence, the distribution function f_s is expressed as:

$$f_s(\mathbf{r}, \mathbf{p}, t) = f_0 \sum_{n=1}^{N_p} \delta(\mathbf{p} - \mathbf{p}_n(t)) S(\mathbf{r}, \mathbf{r}_n(t))$$

where f_0 is a normalization constant and $\mathbf{r}_n(t)$, $\mathbf{p}_n(t)$ and $S(\mathbf{r}, \mathbf{r}_n(t))$ are, respectively, the position, momentum, and spatial shape function of the n^{th} macro-particle. The shape function spreads the charge contribution of each macro-particle over the cells of the grid and it helps to reduce numerical noise in the simulation results.

The number of macro-particles must be carefully chosen [2]. Large values of N_p imply a finer resolution of the plasma density. Intuitively, for a given initial density equal to n_0, the smallest density value that can be resolved corresponds to the contribution of a single macro-particle, which is approximately n_0/N_p. Increasing N_p allows to resolve low density regions and also to reduce statistical noise. On the other side, the available memory puts a limit to the arbitrary increase of the number of macro-particles. As a quick estimation, each macro-particle is represented by $(D + 3 + 1)$ coordinates (where D is the spatial dimensionality, 3 are the components of the momentum and 1 is the weight f_0); each coordinate requires 8 byte of memory and it is calculated on the number of grid points $(L/\Delta x)^D$, where L is the 1-dimensional grid size and Δx its resolution (also known as cell size). The choice of Δx is bound to the smallest scale length l that needs to be resolved: $\Delta x < l$ where, typically, l corresponds to the laser wavelength λ for underdense plasmas and to the collisionless skin depth c/ω_p in the overdense case. Finally, if V is the volume of the grid occupied by the plasma, then the memory requirement is $N_p \times 8(D + 3 + 1)(L/\Delta x)^D V$, without taking into account the additional $8 \times 9(L/\Delta x)^D$ needed to define the EM fields and the current density on the grid.

The PIC iterative loop works as follows: within a time step, the Lorentz force acting on each macro-particle is interpolated starting from the field values on the grid nodes; then, the particle pusher updates the position and momenta of the macro-particles; the renewed distribution determines the current density to advance the electromagnetic fields in time. Such loop is repeated for the whole duration of the simulation. Further details about the usual algorithms implemented to integrate the Maxwell equations and to advance the particle positions and momenta in time can be found in [93, 94].

The numerical simulations presented in this work have been performed with PICCANTE, an open-source, massively parallel, fully relativistic PIC code developed at the University of Pisa [16, 95]. PICCANTE is designed to allow for a great variety of simulations, ranging from 1D to 3D geometries and accessible both to laptops and supercomputing facilities.

The key features of PICCANTE are listed in table 2.3. The input file (written in the JavaScript Object Notation format) allows to set up a simulation in a very straightforward manner. The user can choose the geometry and resolution of the grid, together with some advanced options like the stretched grid and the moving window. An unlimited number of particle species (either electrons, protons or ions with specific Z/A ratio) as well as an unlimited number of laser pulses can be placed in the simulation box. There are already many target geometries implemented in the code, but the user is free to employ any density function $\rho(x, y, z)$: a nice example of this flexibility is given in [96], where a nano-structured foam target has been generated with random clusters of spheres. Outputs consist of a *.dat* file, containing the evolution of the fields and particles energies during the simulation, and binary files, which store full information about the EM field, particles phase-space, density distributions and so on. The user can select both the time and sub-regions of the simulation box in which to collect the output. PICCANTE also includes a toolkit to convert large *.bin* files into more manageable *.txts* for the visualization of the results.

Parameter	Options
input file format	*.json*
geometry	1D, 2D, 3D
parallelization	along all axes
boundaries	periodic, open
grid	rectangular, stretchable
moving window	available
particle species	electrons, protons, ions (Z/A)
temperature distributions	Maxwellian, waterbag, supergaussian
plasma geometry	box, gratings, density ramps...
laser pulse	Gaussian profile in the transverse direction, $\cos^2$ in the longitudinal one
others	radiation friction is enableable
output	density, phase-space, EM fields, current
output format	*.dat* and *.bin*

Table 2.3: Main features of the PICCANTE code.

The almost 100 two-dimensional simulations performed in this work aimed at supporting the analysis of the experimental observations, and addressing some laser-plasma parameters that become more accessible in the numerical scenario. Simulations were performed on the HPC cluster CNAF (Bologna, Italy). The specific parameters chosen in the simulations are reported in chapter 3 and 4, closer to the corresponding results. It is worth reminding that a set of 3D simulations realized with PICCANTE on the same topic has already been discussed in [16], together with the first experimental results obtained in 2014 and reported in [10]. Both the cited works are related to the present manuscript thanks to a fruitful and long-lasting collaboration between the authors. The simulations reported here are meant to extend the numerical investigation in light of the most recent and abundant experimental results obtained over three years, which still remain the main topic of this work.

Chapter 3

Surface electron acceleration

This chapter reports decisive experimental evidence of Surface Plasmon excitation in the relativistic regime.

Although many numerical works had foreseen surface field enhancement and increased target absorption with a grating irradiated at the resonant angle for SP excitation, no experiment incontestably validated the role of SPs in highly-intense laser-grating interactions, because laser systems usually lacked the necessary temporal contrast not to destroy the target surface. On the contrary, the experimental campaign performed in 2014 at CEA Saclay definitely related SPs to the acceleration of energetic electrons along the target surface: it was indeed the first pioneer result to support the experimental accessibility to *Relativistic Plasmonics*. Just as remarkably, those measurement proved the feasibility of direct electron acceleration by the SP's EM field, a process which numerical simulations had not deeply characterized yet.

At the top of a thorough experimental work stands the first observation of multi-MeV, low-divergence electron bunches emitted along the surface of a dielectric grating irradiated at the resonant angle for SP excitation by a ultra-high contrast laser pulse. Contained within less than 10° of angular spread, ∼ 100 pC of charge give rise to huge charge density for a set of different gratings, whose results are shown in figure 3.1a. Additional measurements indicate that up to 700 pC are produced by varying the grating profile and depth. These values and the remarkable reproducibility of the acceleration mechanism support the development of a bright, laser-synchronized electron source at moderate energies (∼ 10 MeV). Alongside the experimental data, two-dimensional numerical simulations reproduce the acceleration process, confirming the electron emission along the target surface and the energy measurements. An example of electron spectra in the tangent direction obtained by irradiating a grating target with various incidence angles, where 30° is the resonant one, is presented in figure 3.1b for a 2D PIC simulation.

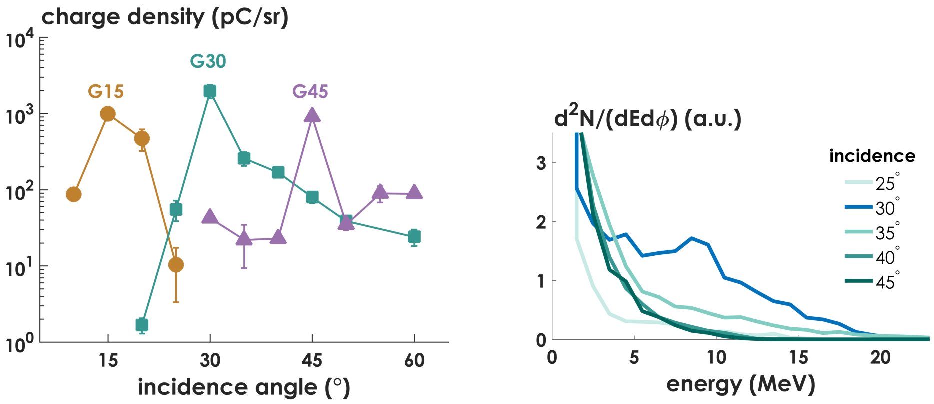

(a) experimental results

(b) 2D PIC simulations

Figure 3.1: Charge density (a) and energetic spectra (b) of SP-driven electron bunches accelerated along the target surface for different incidence angles. All signals peak at the resonance angle 1.20 on page 22, giving compelling evidence of SP excitation in the relativistic regime.

This chapter is organized to give a comprehensive picture of electron acceleration driven by SPs in the relativistic regime. The first part resumes few experimental observations of electron acceleration from solid targets reported in the literature, aiming to emphasize the rather erratic scenario against which SP-driven electron bunches stand for stability and reproducibility. Previous results on SPs in the relativistic regime are included as well. The second section anticipates how a SP is expected to affect the dynamics of a test electron: a theoretical model [97] is proposed, similar to the popular work of Tajima and Dawson about the electron acceleration in wake plasma waves [98]. The third and fourth sections contain the detailed description of the experimental and numerical results. Conclusions are summarized in the last section.

3.1 Previous results on electron acceleration and relativistic SPs

Over the past few decades, the leading mechanisms for electron acceleration from solid targets presented in chapter 1 have been enriched by numerous and sometimes contradictory experimental and numerical observations. Not only the ponderomotive scaling for the fast electron energy $\propto (I\lambda^2)^{1/2}$ (equation 1.10 on page 10) has been put into question [99, 100], but especially the spatial features of the electron emission underline the fundamental role of many different parameters: laser polarization, incidence angle, intensity and, above all, temporal contrast and plasma density scale length.

A collection of results obtained with flat targets is puzzling on its own. At low intensities ($I \sim 10^{17}\mathrm{W/cm}^2$), 45° of incidence and no pre-plasma, electrons are emitted in the specular direction [101], between the target normal and the laser reflection [102], with a peak both in the normal direction and at the specular [103]; adding a pre-plasma broadens the electron spatial distribution [101] or moves it to the normal direction [104]. For higher laser intensities ($I \sim 10^{18}\mathrm{W/cm}^2$) the scenario does not change much: emissions along the specular [105, 106] and the normal [107] directions are reported with no clear indication about their controllability. In most cases these results are also accompanied by ad hoc simulations that explain the emission angles with the interplay between the components of the EM field at the surface. For instance, the generation of quasi-static magnetic fields when the laser impinges at almost grazing angles is supposed to induce an electron current along the target surface [48, 108]. Furthermore, the electrons' initial conditions will affect how they interact with the EM distribution, determining their final energy and distribution. In a very recent work, electrons ejected in the specular direction from a solid step-like plasma have been shown to possess a specific phase with respect to the laser pulse; because of this, they interact with the reflected beam and are accelerated to high energies [11]. A possible drawback of this mechanism is the need for a sub-micrometric control of the plasma formation at the target surface, which might be difficult to realize in a stable fashion (compare section 4.3 for more details about this topic).

Sub-wavelength grating targets were employed in experiments at low laser intensity, $\sim 10^{16}$, 10^{17} $\mathrm{W/cm}^2$. In one case [109], although reporting surface electron acceleration, the grating was not irradiated at the resonant angle for SP excitation but rather at large incidence (67.5°), and no information about the energetic distribution of the fast electrons was provided. In another experiment [110], the grating was indeed irradiated at the resonant angle, but both the sketch of the experimental arrangement and the results (electron emission only in the specular direction) suggest that the significant emission angles were overlooked. As already remarked, sub-wavelength gratings allow only two diffraction orders, the specular and the back-propagating $|n| = 1$. In that case, the diagnostics covered only the half-space containing the specular reflection, hence failing to detect any SP-driven electron emission at the target surface.

On the contrary, limited, yet inspiring evidence of relativistic SP-assisted electron acceleration was reported in an experimental campaign performed at CEA in 2012 and devoted to ion acceleration [9]. As a matter of fact, the work described in this thesis aimed at enlightening some features discovered on that occasion by exploring the spatial distribution of the accelerated particles all around the target.

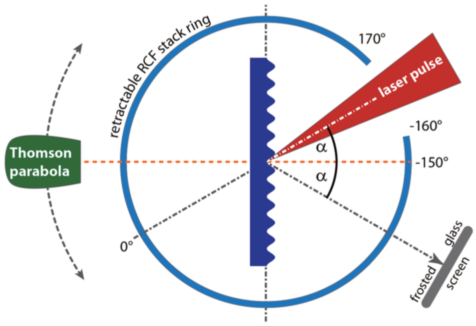

Figure 3.2: Setup of the CEA experiment in 2012, from [9].

Referring to the diagnostic arrangement illustrated in 3.2, the radiochromic film stack surrounding the target recorded a signal also in the tangent direction, when the grating (a G30 similar to the ones described in chapter 2) was irradiated at resonance. Consistently with the fact that electrons cross the radiochromic films with little energy deposition in their active layer, this signal was quite weak and was found on each film regardless of their depth within the stack (more details about these detectors and their large employment in proton radiography can be found in [111]). These observations originally stimulated to look into SP-driven electron acceleration at relativistic laser intensities.

As a matter of fact, at the time of this experiment most of the attention to relativistic SPs had been drawn by the results of two-dimensional PIC simulations which showed increased target absorption under the form of more numerous and more energetic hot electrons injected in the target, rather than direct electron acceleration along the target surface itself[1]. Large heating in this direction was explained either with the wave-breaking of the SP [112] or in terms of momentum conservation [113]. A sort of “two-dimensional’

---

[1] Riconda et al.’s detailed study of electron acceleration in the fields of a SP [55] was published pretty at the same time of the experiments described in this manuscript. Likewise, benchmarking 3D simulations reporting the spatial distribution of SP-driven electron emission were performed in 2016 by L. Fedeli [16] and are commented in section 3.4.

vacuum-heating" also accounted for the generation of strong ($\sim$ 200 MG) quasi-static magnetic fields that confine the particles near the grating surface [113].

Absorption values up to 70% were reported, with a $\sim\times 2$ times increase of the maximum electron energy (averaged on the whole space). However, the analysis of the electron spatial distribution did not exhibit any significant electron acceleration along the target surface [112]. On the contrary, the generation of hotter electrons led to a comparable enhancement of the ion cutoff energy [114].

In the wake of these simulations, the experiment of 2012 at CEA successfully reported for the grating irradiated at resonance a $\times 2.5$ increase of the maximum proton energy detected at the rear surface of the target [9]. In correspondence of the same incidence angle the reflected laser light (monitored with the CCD-imaged frosted screen in figure 3.2) showed a global minimum, supporting the enhanced laser absorption associated with the SP. In continuity with these results, also the most recent experiments focused on electron acceleration were equipped for ion detection as well. However, since this is a minor topic with respect to the electron emission, results on proton acceleration are briefly described in appendix D.

3.2 SPs for surface electron acceleration

As already introduced at the end of chapter 1, SPs enhance the amplitude of the local electric field at the target surface, improving the laser absorption. Additionally, the observation of intense electrons bunches along the target surface anticipated in figure 3.1a supports the feasibility of direct electron acceleration by the components of the SP's electric field. This section provides a helpful model [10, 55, 97] to describe such process and to give an estimation of the attainable energy and emission angle. Both these quantities are firstly inferred in the reference frame S$'$ that moves at the phase velocity of the SP, simplifying the distribution of the EM field: in fact, the field becomes electrostatic in the vacuum region. Then, the energy and momentum of one electron moving in the electrostatic potential are transformed back in the laboratory frame. The acceleration is particularly efficient for those electrons that are moving at the SP phase velocity, which is close to c if $\omega_p \gg \omega$. For high field intensities, the $\mathbf{v} \times \mathbf{B}$ force strongly contributes to the electron self-injection.

3.2.1 Structure of the SP fields

Referring to the geometry displayed in figure 1.3a, let the overdense plasma develop in the $z > 0$ region, with a density described by a step-profile $n_e = n_0\Theta(z)$. The dielectric constants for the vacuum ($z < 0$) region and for the plasma ($z > 0$) are, respectively, $\varepsilon_1 = 1$ and $\varepsilon_2 = 1 - \omega_p^2/\omega^2$. Reminding that the SP is a TM-polarized wave, the components of its EM field can be written as:

$$
\begin{aligned}
E_x(x,z) &= E_0 e^{ik_x x - i\omega t}\big[\Theta(-z)e^{k_1 z} + \Theta(z)e^{-k_2 z}\big],\\
E_z(x,z) &= -ik_x E_0 e^{ik_x x - i\omega t}\left[\Theta(-z)\frac{e^{k_1 z}}{k_1} - \Theta(z)\frac{e^{-k_2 z}}{k_2}\right],\\
B_y(x,z) &= i\frac{\omega}{ck_1} E_0 e^{ik_x x - i\omega t}\big[\Theta(-z)e^{k_1 z} + \Theta(z)e^{-k_2 z}\big],
\end{aligned}
\tag{3.1}
$$

where E_0 is the amplitude of the field parallel to the interface, $k_{1,2}$ are the wavevectors in the vacuum and plasma regions that satisfy the wave equation 1.16 on page 19. Hence, it is:

$$
k_x = k_{\mathrm{SP}} = \frac{\omega}{c}\sqrt{\frac{1-\alpha}{2-\alpha}}; \qquad k_1 = \frac{k_x}{\sqrt{\alpha-1}}; \qquad k_2 = k_x\sqrt{\alpha-1},
$$

where the parameter $\alpha = \omega_p^2/\omega^2$ has been defined for brevity. Both E_x and B_y are continuous at the interface $z=0$, while the discontinuity of E_z produces a surface charge density $\sigma(x,t) = \tilde{\sigma}e^{ik_x x - i\omega t}$, with $\tilde{\sigma}$ given by the amplitudes of the electric field at the boundary: $\tilde{\sigma} = 4\pi\big[\tilde{E}_z(0^+) - \tilde{E}_z(0^-)\big]$. It is also worth noticing from the expressions of the SP's fields 3.1 that in the limit of $\alpha \gg 1$, which is the relevant case to this work, the parallel component of the electric field in the vacuum region is negligible with respect to the perpendicular component, since it is $|E_x| = (k_1/k_x)|E_z| \simeq (\omega/\omega_p)|E_z|$. On the other hand, the magnetic field $|B_y|$ is of the same order of $|E_z|$.

Then, the field components are transformed to the S$'$ frame which moves with the phase velocity v_φ of the SP along the interface:

$$
\begin{aligned}
E'_x &= E_x,\\
E'_z &= \gamma(E_z + \beta B_y),\\
B'_y &= \gamma\Big(B_y + \beta E_z\Big),
\end{aligned}
$$

where $\gamma = (1-\beta^2)^{-1/2} = \sqrt{\alpha-1}$ and $\beta = v_\varphi/c = \omega/(k_x c)$. Moreover, the phase $(k_x x - \omega t)$ becomes $k'_x x' = (k_x/\gamma)x'$, since $\omega' = 0$. It follows that the EM field in the frame S$'$ is static.

Performing the Lorentz transformations returns:

$$
\begin{aligned}
E'_x(x,z) &= \big[\Theta(-z)e^{k_1 z'} + \Theta(z)e^{-k_2 z'}\big]E_0 e^{ik'_x x'}\\
E'_z(x,z) &= -i\big[\Theta(-z)e^{k_1 z'} - \Theta(z)\gamma^2 e^{-k_2 z'}\big]E_0 e^{ik'_x x'}\\
B'_y(x,z) &= i\frac{\omega}{c}\frac{\alpha}{k_x}\Theta(z)e^{-k_2 z'}E_0 e^{ik'_x x'},
\end{aligned}
$$

with $z' = z$. Visibly, in the moving frame there is no magnetic field in the vacuum region, hence a discontinuity that is consistent with the transformation of the charge density σ in S into a current in S$'$. At the same time, in the vacuum region the perpendicular component of the electric field has now become of the same order of the parallel component, $|E'_x| \simeq |E'_z|$.

As the SP field in S$'$ and for $z < 0$ is purely electrostatic, the electrostatic potential ϕ' is immediately defined as:

$$\phi'(x, z < 0) = i\frac{\gamma}{k_x} E_0 e^{k_1 z'} e^{ik'_x x'}.$$

3.2.2 Single-electron acceleration in the vacuum region

One electron plunged in the two-dimensional electrostatic potential ϕ' has a potential energy

$$U(x, z < 0) = -e\phi'(x, z) = e\frac{\gamma}{k_x} E_0 e^{k_1 z'} \sin{(k'_x x')}.$$

and, depending on its initial conditions, can be accelerated. Complex electron trajectories require a numerical treatment to identify the best regime for the electron to gain the highest energy from the interaction with the SP. However, a reasonable estimation for the electron energy is obtained in the following way.

Looking at the profile of the potential energy $U(x, z < 0)$ in figure 3.3, a test electron will gain the maximum energy if starting at rest at the interface ($z = 0$), on a peak ($x' = \pi/(2k'_x)$), and moving down to the region where $U \sim 0$. Note that an electron with $v'_x = 0$ in S$'$ means that it is moving with the SP phase velocity v_φ in S. Still, the electron trajectory down the potential hill will be extremely sensitive on the initial conditions, and the final energy gain will depend on the motion along both the directions x' and z in S$'$ (some more details about the electron initial conditions are given in the following section).

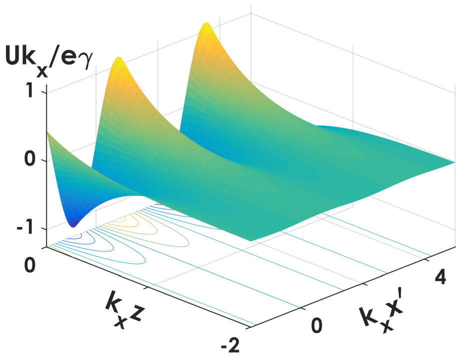

Figure 3.3: Electrostatic potential of the SP in the boosted frame.

The final kinetic energy acquired by the electron in the boosted frame can be written as:

$$W'_K = m_e c^2(\gamma_f - 1) \simeq eE_0\frac{\gamma}{k_x},$$

where $\gamma_f = [1 + (p'^2_x + p'^2_z)/(m_e^2 c^2)]^{1/2}$ is calculated with the final momentum along both x' and z. The total energy in S$'$ is therefore $\mathcal{E}' = m_e c^2 + W'_K$.

Back in the laboratory frame, the energy gain becomes:

$$\Delta\mathcal{E} = \mathcal{E} - \mathcal{E}_0 = \gamma(\mathcal{E}' + \beta c p'_x) - \gamma m_e c^2 = eE_0\frac{\gamma^2}{k_x} + \gamma v_\varphi p'_x. \tag{3.2}$$

This expression clearly shows that the energy gain depends on how the electron slides down the potential hill through both the value and sign of p'_x: if $p'_x > 0$, it means that the electron has fully explored the potential of the SP along the surface, while gaining also additional momentum in the perpendicular direction [55].

In the limit case where $p'_x = 0$, the electron has proceeded down the potential hill along a constant x' [97]. In this situation, it is possible to derive also the expression for the emission angle, by knowing that $p'_z = [(\mathcal{E}'^2/c^2)(1 - m_e^2c^4/\mathcal{E}'^2)]^{1/2}$. If $W'_K \gg m_e c^2$, then $p'_z \simeq W'_K/c$ and transforming the four-momentum back in the laboratory frames gives:

$$p_z = p'_z = \frac{W'_K}{c}, \qquad\qquad p_x = \gamma\beta\frac{\mathcal{E}'}{c} \simeq \gamma\beta\frac{W'_K}{c}.$$

Therefore, the emission angle measured from the normal to the interface is

$$\tan(\phi) = \frac{p_x}{p_z} = \gamma\beta. \tag{3.3}$$

In the same configuration, the acceleration length in the laboratory frame can be estimated as $\mathcal{L}_{acc} = \Delta\mathcal{E}/(eE_0) = \gamma^2/k_x$. When taking into account also the acceleration along the surface (*i.e.* $p'_x \neq 0$), the acceleration length is expected to increase in relation to the higher energy gain predicted by the expression 3.2.

For a comparison with the experimental parameters, it is useful to define the dimensionless parameter $a_{\mathrm{SP}} = \gamma eE_0/(m_e c\omega)$ that, in analogy to the laser field, discriminates the regime of high intensity fields (*i.e.* $a_{\mathrm{SP}} > 1$). Note that a_{SP} is written in terms of the amplitude γE_0 of the *perpendicular* component of the SP's electric field, which is the largest one in the electromagnetic limit. Assuming that the laser energy will be totally addressed to the excitation of the perpendicular component of the SP's electric field[2], then for the laser intensity of UHI100, $a_{\mathrm{SP}} \simeq 3$. For a solid target density of $n_e \sim 400n_c$, the γ factor and the phase velocity of the SP v_φ become respectively ~ 20 and $0.998c$. Then, the energy gain 3.2, emission angle 3.3 and acceleration length $\mathcal{L}_{\mathrm{acc}}$ are estimated as:

$$\Delta\mathcal{E} \simeq m_e c^2 a_{\mathrm{SP}}\gamma\frac{v_\varphi}{c} \sim 30\ \mathrm{MeV}; \qquad \phi = 87^\circ; \qquad \mathcal{L}_{\mathrm{acc}} \sim 50\,\mu\mathrm{m}.$$

These results are in strong agreement with the values found in the experiments. As already anticipated in the introduction, the emission of electrons is found

---

[2] In addition to the inaccuracy of considering that the laser energy is entirely transferred to the SP, the fact that the ratio between E_x and E_z is expected not to change when increasing the plasma density n_e is currently under study with numerical simulations.

close to the target surface, as confirmed by the value of ϕ. The maximum energy, besides being comparable with the cutoff in the numerical spectra shown in figure 3.1b, is of the same order of the experimental values reported in the following section (for example in figure 3.10). Finally, the acceleration length can be related to the size of the damage left on the targets after the laser shot, as explained later in figure 3.4.

3.2.3 Insights into the injection conditions

It is worth discussing some details about the acceleration process that are beyond the simple model presented in the previous section. As already explained, an electron needs to be injected in the surface wave with $v_x \simeq v_\varphi$ to be accelerated by the SP. But the very characteristics of the SP determine which configurations are more efficient [55].

In particular, in the relativistic ($a_{\mathrm{SP}} > 1$), electromagnetic ($\omega_p \gg \omega$) limit, the contribution of the $\mathbf{v} \times \mathbf{B}$ force to the electron dynamics turns out to be critical for the electron self-injection. As already reminded, in this case $|E_x| \ll |E_z|$ and $|B_y| \sim |E_z|$ in the vacuum region. Hence, one electron accelerated at $v_z \leq v_\varphi$ by the strong perpendicular field E_z can be bent by the magnetic field B_y and injected in the surface wave along x. Even when it reaches relativistic velocities, the electron can stay in phase with the SP for a long time ($v_\varphi \sim c$), until either it is ejected far from the surface or the SP is damped. Indeed, the wave efficiently yields its energy to the hot electrons pushed inside the overdense region by the normal component of the EM field (in a sort of enhanced vacuum heating [113]). Additional self-injection of electrons along the surface can also be caused by the wavebreaking of the SP [112].

Another significant parameter is the entry phase of the electron in the SP. It expresses the moment when the electron is injected in the surface wave, which also corresponds to a certain position along the surface. If the electron enters the SP with the optimal phase, it always interacts with an accelerating field, achieving the maximum energy gain. Numerical simulations indicate that the final electron momentum in this case is enhanced by 15% to 50% with respect to the worst entry phase, depending on the extent of the SP's evanescence length $L_1 = k_1^{-1}$: the broader L_1, the higher is the velocity acquired along the surface [55]. This is because the electron remains longtime within the region with the SP fields, despite progressively departing from the surface because of their perpendicular momentum.

3.3 Experimental results

The measurements presented in this section are the result of many experimental campaigns realized between 2014 and 2016, addressing the SP-driven electron acceleration under numerous different conditions. Firstly, the spectral and spatial distribution of the electron emission was analyzed by varying either the laser incidence angle ϕ_i or the grating period Λ, in order to explore the resonance condition 1.20 on page 22. Flat targets were always irradiated in the same configurations as a comparison. Then, more details about the acceleration mechanism and the best interaction conditions are inferred with a thorough scan of the grating properties (depth, profile, etc.). Finally, surface electron acceleration was observed at even higher intensity, thanks to some preliminary tests carried out on a PW-class laser installation, and reported in the last section.

For a given incidence angle, the target position at focus is ensured by the two green pointer lasers described in chapter 2. However, small vibrations during the air pumping could slightly displace the optics in the interaction chamber, resulting in a target misalignment. The first laser shots are therefore reserved to optimize the target position, by looking for the most intense electron emission from the flat target; then, the green lasers are re-centered and employed for all the following shots.

One immediate clue of the excitation of a surface wave is given by the aspect of the target surface after the laser shot. The fast, concentrated deposition of the laser energy, the consequent target heating and expansion leave a hole on the thin Mylar foils and a mark on the surface of solid gratings. The size of both damages is larger than the pulse focal spot ($\sim$ 800 μ in diameter), indicating that they fully develop after the laser irradiation. However, a peculiar shape is observed when gratings are irradiated at the resonant angle for SP excitation, as shown in figure 3.4. In this case, the holes

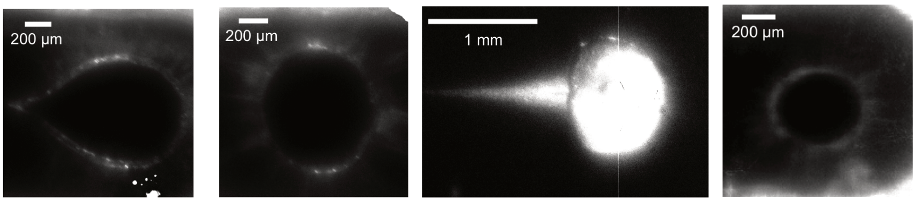

(a) G45 (b) G45, low contrast (c) SG13 (d) F

Figure 3.4: Laser-irradiated targets. All gratings were irradiated at the resonant angle for SP excitation (*i.e.* 45° in (a) and (b), 30° in (c)), the flat foil in (d) at 45°. All shots were done at high contrast, except for the image (b), where the surface of the Double Plama Mirror was not refreshed. In all images, the laser impinges from the right and the SP propagates towards left.

exhibit a tip in the direction predicted for the SP propagation. Typically, the sharper the tip, the more intense and energetic is the electron emission in the tangent direction. The marks on solid grating are slightly larger than the holes, and instead of the tip there is a long (1.3 mm in the figure) pointed streak along the SP propagation. In comparison, flat foils always show circular holes. They are smaller than the holes on gratings ($\sim 500\ \mu$m in diameter), suggesting a less efficient laser-target coupling. It is even more interesting that round holes also appear when irradiating grating targets at non-resonant angles or with a bad laser contrast. Hence, the tip denotes a significant and collimated energy propagation along several μm on the target surface; this feature appearing only when gratings are irradiated at resonance and with ultra-high laser contrast is a straightforward evidence of the SP excitation. When comparing the size of the tip with the acceleration length presented in the previous section, it is also fair to assume that the SP has enough space ahead of its propagation to accelerate electrons up to some MeV of energy.

Electron diagnostics

Electron diagnostics are designed to record both the spatial and energetic distribution of the electrons emitted in the half-space in front of the target. Both diagnostics use a Fast Lanex Screen (by Carestream) as detector.

Lanex screens are composed by layer of phosphor powder (typically Terbium activated Gadolinium oxysulfide GdS:Tb) sandwiched between two transparent coatings. Energy deposited in the screen by ionizing particles or radiation is converted into visible light sharply centered at 543 nm. Because the fluorescence decay time is quite fast (less than 10 ms [115]), imaging the scintillating screen with a triggered camera is less-demanding than, for example, processing an Image Plate: in this sense, a Lanex is particularly adapted for high repetition rate experiments.

As already shown in figure 2.2, a large Lanex screen (15×7 cm^2) is mounted on a rotating platform and tilted by 45° with respect to the target surface. Its size is adapted to cover the electron emission from the target tangent to its normal at 8 cm from the chamber center. The screen is protected by a 200 μm thick Aluminum slab to stop X-rays and electrons below 150 keV from hitting the screen. In the following, the angular directions over the Lanex screen will be indicated as ϕ on the incidence plane and θ in the vertical direction (the azimuthal and polar angle, respectively). They are inferred from the coordinates (x, y) of a generic point P on the image with the expressions C2 and C1 described in appendix C. In addition, it must be considered that the distance between the Lanex and the target varies along ϕ because of the screen tilt, subtending different solid angles: for example, at 45° of incidence, the point on the Lanex screen corresponding to the specular direction would be at $(80 \times \sin(45°)) = 56$ mm away from the target, resulting in a less dispersed, more intense signal. A proper correction is thus implemented on all measurements to fairly compare the signal as it was collected at a fixed distance from the electron source.

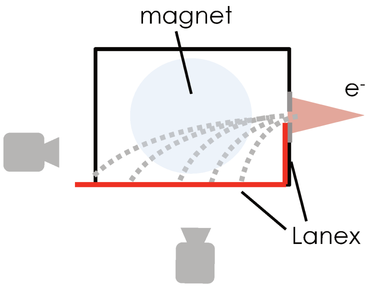

Figure 3.5: Top view of the electron spectrometer.

The electron spectrometer is aligned behind the Lanex screen, at 11 cm from the chamber center. It consists of two parallel round magnets (5 cm diameter) spaced by 2 cm of vacuum, mounted inside an iron yoke with a collimating slit of 1.5 mm at its entrance. The magnetic field is ~ 0.9 T. The trajectories of electrons with energies in the range 0.05 – 18 MeV have been accurately calculated by J. R. Marques[3], who performed a calibration of the spectrometer at the linear accelerator ELSA of CEA DAM. As shown in figure 3.5, electrons with energies above 1.4 MeV are bent by 90° and reach the Lanex screen on the side of the yoke. Electrons below this energy are curved back and hit another small piece of Lanex placed inside the yoke, right next to the slit. The screen on the outside is protected by 100 μm of Aluminum to reduce X-ray noise. The width of the entrance slit determines the energy resolution of the spectrometer, which is ~ 500 keV for ~ 10 MeV electrons.

The rotating platform is arranged along the target surface, and both the electron diagnostics are accurately aligned with respect to the target tangent with a green pointer laser. A 2 mm diameter hole is drilled in the large Lanex screen in order to correct the spectrometer orientation.

Three cameras outside the interaction chamber record the emission from the Lanex screens: 12-bit CMOS Mako cameras with f : 25 mm objectives are employed with the electron spectrometer, and a 12-bit CCD Basler camera coupled with a Computar TV Zoom objective looks at the tilted screen. All cameras are provided with band-pass filters at 546 nm and have the exposure time set to 50 ms. To avoid image saturation, the incoming signal is reduced by changing the gain of each camera and eventually by using neutral optical densities. The signal variation over the gain range is not linear and it has been accurately calibrated for all cameras with a uniform light source: the signal decreases at maximum by a factor of ~ 20 with the Mako and by ~ 40 with the Basler (this last is used in 8-bit acquisition mode).

The intensity of the light emitted by the Lanex screen is proportional to the amount of deposited energy within the phosphor layer: for electrons, this amount does not depend on the electron initial energy above 1.5 MeV [116]. Below this threshold, electrons are either slowed or stopped in the sensitive layer, making the Lanex response highly non-linear. From the

---

[3] *LULI, Ecole Polytechnique, Palaiseau Cedex, France.*

measurements obtained with the electron spectrometer throughout the experimental campaign, it turns out that a negligible amount of electrons below 1.4 MeV of energy is emitted, because no signal is ever recorded by the Lanex beside the collimator. Therefore, measuring the light intensity from the scintillating screen provides a direct estimation of the amount of charge that has reached the Lanex. To this purpose, both the Lanex and the optical system employed during the experiments were calibrated with stable electron bunches available at two different facilities located in Orsay (France): the photo-injector PHIL (Laboratoire de L'Accélérateur Linéaire, [117]), and the laser-triggered radio-frequency electron accelerator ELYSE (Laboratoire de Chimie-Physique). The screen shows a linear response to charge amounts ranging from 20 pC to 100 nC [118, 119]. Details of the calibration campaign are given in appendix B. In the same way, the homogeneous energy deposition in the sensitive layer for electrons above 1.5 MeV results in a negligible influence of the incidence angle of these electrons with respect to the screen surface [120]. As a consequence, the angular distribution of the emitted light is well described by a Lambertian cosine law, which must be taken into account when measuring the signal collected at different observation angles and distances from the cameras. The method employed in this work to estimate these two important parameters is detailed in appendix A.

3.3.1 Electron acceleration for different grating periods

The simple-Mylar thin gratings listed in the table 2.1a on page 36 are irradiated at the corresponding resonant angles ϕ_{R}: 15°, 30° and 45°. The case for G30 at 30° is shown in 3.6a and it is representative of the electron emission recorded by the Lanex screen for all the resonances. As a comparison, the result from the flat target irradiated at the same incidence angle is shown in 3.6b, with a reduced color range to make the signal stand out. Clearly, the grating emits a huge amount of electrons on the incidence plane (*i.e.* $\theta = 0°$) and in the tangent direction (*i.e.* $\phi = 0°$). On the other hand, fewer electrons from the flat foil are scattered around a quite symmetric hole, which is interpreted as the ponderomotive force of the reflected laser pulse expelling the electrons in the radial direction [11, 48, 105]. Also the emission from the grating exhibits a small hole in correspondence to the specular reflection, but more importantly another one is visible at $\phi \sim 90°$, matching the position of the first diffraction order. This persuades that the grating period has been preserved all along the interaction by the high laser contrast.

Figure 3.7 features the lineouts of these shots along ϕ, for $\theta = 0$. The signal has been rescaled to take in account the different solid angles subtended by the tilted screen along the lineouts, and also the observation angle and the distance from the CCD. The corrected profiles do emphasize that the electron emission from the flat foil is ~ 20 times weaker with respect to the grating at resonance. As explained in appendix C, the lineouts along ϕ and

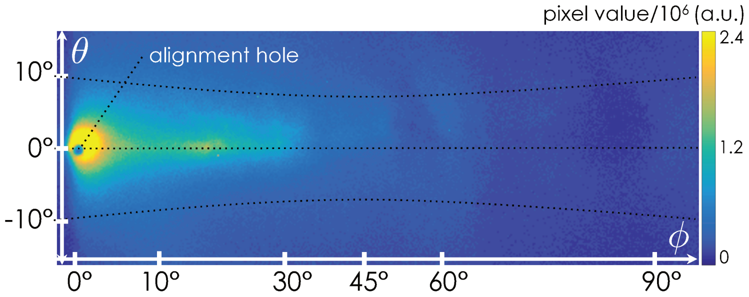

(a) G30 at resonance

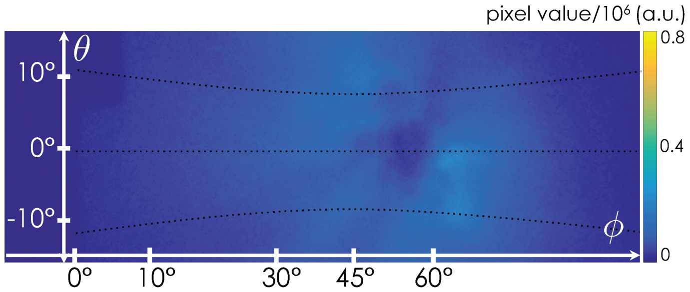

(b) F at 30° of incidence

Figure 3.6: Spatial distribution of the electron emission obtained at 30° of incidence by (a) the grating G30, which is resonant in this case, and (b) the flat foil. The color ranges are $[0, 2.4 \times 10^6]$ for (a) and $[0, 0.8 \times 10^6]$ for (b). The alignment hole drilled in the Lanex screen is clearly visible in the grating emission.

θ allow to recover the size of the electron bunch and the sum of pixel counts inside of it. For example, the angular spread in figure 3.6a corresponds to $\mathrm{FWHM}_\theta = 4.6° \pm 0.1°$ and $\mathrm{FWHM}_\phi = 5.7° \pm 0.2°$, where the uncertainties come from fitting the experimental points with Lorentzian distributions. The signal in the electron bunch is converted to charge after the Lanex calibration, resulting into ~ 97 pC for this particular shot.

The first test to verify that the electron bunch in the tangent direction is bound to the SP excitation is to change the incidence angle and to void the resonance condition 1.20. In the experiment, the target holder and the platform with the diagnostics were rotated of the same angle to preserve the alignment; the signal collected by the external CCDs was rescaled accordingly with the expression C3 and C5 given in appendix C. For completeness, some raw images of the incidence scan on a G30 are reported there as well. For each thin grating and each incidence angle, the electron emission in the tangent direction has been analyzed with the lineouts of the experimental images, leading to the resonance curves illustrated in figure 3.8. Each point represents the average of all shots, with error bars given by the standard

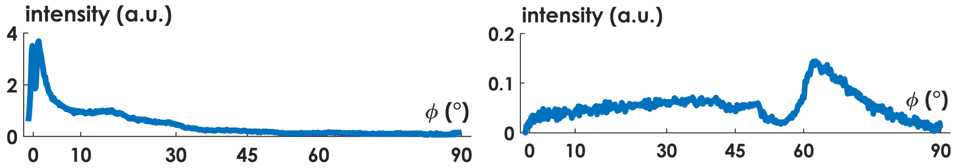

(a) Grating G30 at resonance

(b) Flat foil at $\phi_i = 30°$

Figure 3.7: Longitudinal lineouts of the signals shown in figure 3.6.

error[4]. The graphs indicate how the emission is most collimated at resonance, with similar FWHM$_\theta$ and FWHM$_\phi$ for all gratings; the size significantly increases even within ±5° of the resonant angle.

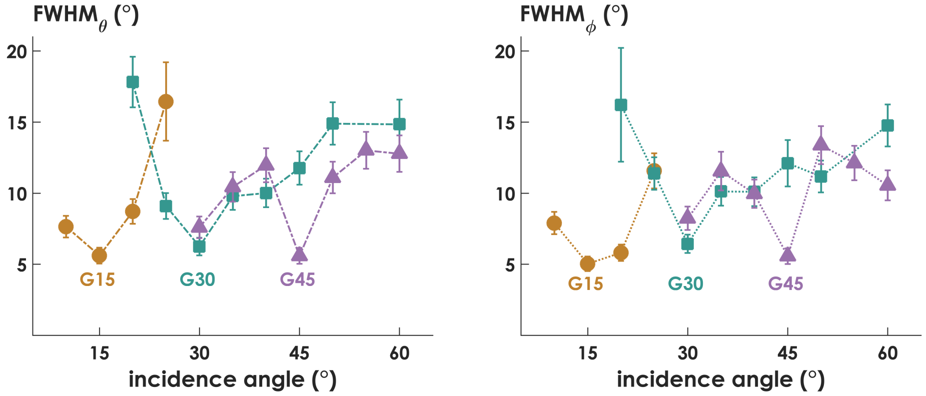

(a)

(b)

Figure 3.8: Analysis of the θ (a) and ϕ (b) lineouts for the thin gratings: the best collimation is achieved at resonance.

A similar result comes from the charge measurement, presented in figure 3.9. For each incidence angle, the Lanex signal is integrated over the bunch area estimated with the previous analysis and converted to charge. Again, each point in the plot represents the average and standard error of all the experimental images. The resonant effect on the charge acceleration is dramatically evident: when the SP is excited, the charge is at least 3 times higher than with other incidence angles, peaking at ~ 100 pC with the G30 and ~ 40 pC with the G15 and G45. Remarkably, these curves show that the resonance condition 1.20 deduced by the non-relativistic, linear theory still

---

[4] From hereafter, the *standard error* refers to the standard deviation of the sample mean. Given a set of N shots acquired in the same conditions, the standard error of the mean of the sampled x_i is calculated by $SEM = \sigma/\sqrt{N}$, where σ is the standard deviation of the sample, *i.e.* $\sigma = [(\sum_{i=1}^{N}(x_i - \bar{x}))/(N-1)]^{1/2}$.

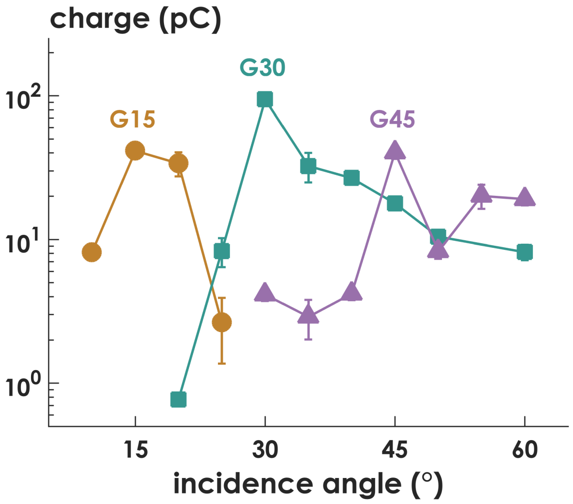

Figure 3.9: Measurement of the charge emission in the tangent direction: each grating produces the greater amount of charge when the resonance condition is fulfilled.

applies to the relativistic regime. As for the collimation, the signal changes abruptly as soon as the resonance condition is not verified, and the charge decrease is more evident when $\phi_i < \phi_\mathrm{R}$. The full trend of the points out of resonance is supposed to depend on a non-trivial ensemble of parameters. First of all, the signal may be expected to increase with the incidence angle, because of a stronger coupling between the normal component of the laser electric field and the target surface: this happens quite visibly for $\phi_i < \phi_\mathrm{R}$. But for the same reason, increasing the resonance angle should result into a greater charge compared to the other gratings, which is not the case in figure 3.9. Hence, other effects must resort to the geometry and shape of each specific grating to explain the subtle differences among them: for instance, the complex interference pattern of the diffracted pulse depends on the grating period, and the slopes of the grating profile depend on its depth (which varies for all the thin grating, as indicated in table 2.1a). Some insight on the role of these parameters is given by the 2D PIC simulations detailed in the following section.

The resonant effect is further confirmed when measuring the energy of the electron emitted in the tangent direction. The result is shown in figure 3.10. The first panel displays the non-Maxwellian[5] energetic spectra collected at resonance for every thin grating. Remarkably, no electrons below the noise level of the spectrometer are detected below 2 MeV; this is confirmed by the fact that the other Lanex screen, placed inside the spectrometer right

---

[5] Non-Maxwellian distributions have also been reported for the electron bunches accelerated in the specular direction at relativistic intensities [11, 105].

next to the collimating slit, never emitted any signal. Most of the electrons are accelerated around a peak value, indicated in the top right panel for each thin grating and incidence angle. The maximum energy E_{cutoff}, in the bottom right panel, corresponds to the point where the signal is equal to 10% of its value at the peak. A complete set of spectra recorded on the G30 is provided in appendix C and it shows that the same energetic profile is obtained for every incidence angle. At the decrease of the peak energy corresponds an equal reduction of the FWHM, so that the energetic dispersion $\Delta E/E \simeq 1.1$ is constant at least within 5° around the resonant angle (and it slightly increases further away, $\Delta E/E \simeq 1.3$). Once again,

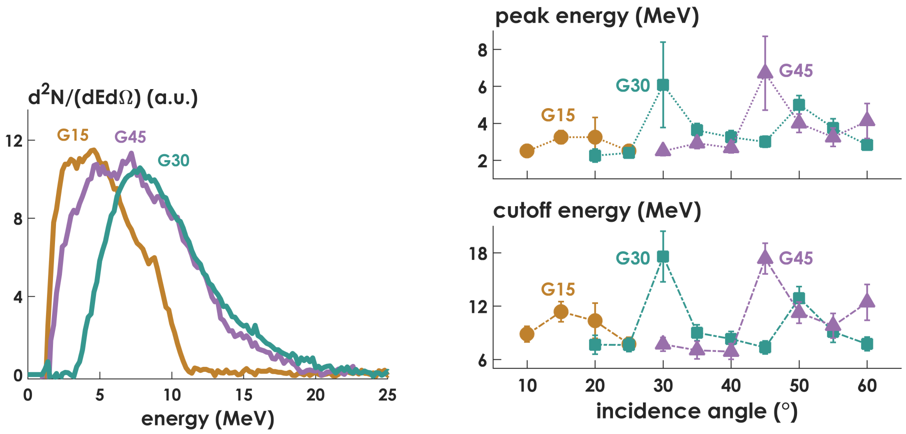

(a)

(b)

Figure 3.10: (a): energetic spectra from thin gratings at resonance. (b): peak (top) and cutoff (bottom) energies as a function of the incidence angle, showing a distinctive energy increase at the resonance angles.

the SP excitation clearly results in the most energetic electrons, with cutoff energies far above 10 MeV. As a comparison, electrons accelerated in the tangent direction were observed to reach only 2 MeV when irradiating flat targets at large incidence angles (70°) and 2×10^{18} W/cm^2 of intensity [48]. Remarkably, the G30 and G45 show a very similar behavior: both the peak (~ 6 MeV) and the cutoff energies (~ 17.5 MeV) are similar. The emission from the G15 is unsuccessfully weaker, although there are suggestions from the experimental images that the electron spectrometer could have been slightly rotated, altering the measurements. In fact, the reference images acquired for the incidence scan on the G15 do not match the position of the spectrometer, for the same incidence angles, recorded on a different day. Further support of this allegation is given by the simulations, where the cutoff energy does not appear to depend on the grating type.

Finally, the results from the gratings are duly compared to the emission from the flat target. Flat foils were mainly irradiated at incidence angles corresponding to the gratings' resonances, where the comparison is expected to be more significant. As already pointed out in figure 3.6b, in this case there is no electron acceleration in the tangent direction and electron bunches of variable size are observed in random positions around the specular reflection of the laser beam. As consequence, the raw images need to be analysed individually, bypassing the lineouts along preferred directions and the Lorentzian fits. The charge is thus estimated in the following way: the observation angle, distance from the target and from the CCD are calculated for the point of maximum signal around the specular; the rescaling factors due to the geometrical corrections are applied to all the points within the area identified by the same $\mathrm{FWHM}_{\theta,\phi}$ of the resonant grating ($\sim 5^\circ$ in both directions); the signal is then integrated over this area and converted with the Lanex calibration. The first column of table 3.1a presents the result: each value is the average of 10 shots, the uncertainty is the standard error. Despite a modest increase for large incidence angles, the charge produced by flat foils is at least 10 times smaller than the emission from resonating gratings. The other values reported in the table represent the change in position of the electron bunch along θ and ϕ. The second table compare the result from the resonating gratings. Although shot-to-shot fluctuations of the bunch position could result from local bending of the target surface, it stands out that the SP-driven electron bunches are stably accelerated in the tangent direction, compared to the higher variability of the emission from flat foils. This also motivates why the electron spectrometer has never been aligned in the specular direction to measure the energetic spectra from flat foils, since there would have been no guarantee to collect the brightest peak of the emission. At the same time, no signal above the noise level was ever detected from flat foils in the tangent direction.

$\phi_i(^\circ)$	Q (pC)	$\Delta\theta(^\circ)$	$\Delta\phi(^\circ)$
15	3 ± 1	2.1	2.2
30	4 ± 1	1.8	2.8
45	5 ± 1	2.3	2.1

(a) Flat

	$\mathrm{Q_G}$ (pC)	$\Delta\theta_\mathrm{G}(^\circ)$	$\Delta\phi_\mathrm{G}(^\circ)$
G15	41 ± 4	0.7	0.2
G30	95 ± 5	0.2	0.05
G45	40 ± 4	0.3	0.1

(b) Gratings

Table 3.1: (a) Charge and position of the electron bunch emitted from a flat target. ϕ_i is the incidence angle; $\Delta\theta$ and $\Delta\phi$ are the standard error of the bunch position on the data set. The same quantities are calculated in (b) for each grating at its resonance ($\mathrm{Q_G}$, $\Delta\theta_\mathrm{G}, \Delta\phi_\mathrm{G}$).

To summarize, surface electron acceleration demonstrates the successful excitation of surface plasmons at the incidence angle predicted by the linear theory also in the relativistic regime. Intense, stable, collimated electron bunches are observed with all the thin gratings, with similar amounts of charge and energetic distributions, regardless of the grating type. The robustness of the mechanism is even more evident when compared to the 20-time weaker, scattered electron bunches produced by flat foils around the specular reflection of the laser beam.

3.3.2 Role of some grating properties

In the attempt to look for a most efficient target and to identify which properties affect the electron acceleration, blazed and Aluminized thin gratings were irradiated at the resonant angle (*i.e.* 30°). Solid gratings (SG) were the cheapest and the handiest solution to have many targets manufactured with the same process, material and period. But in order to discriminate the influence of the Aluminum coating from the one of the blazed profile, also thin, sinusoidal Aluminized gratings were embossed with the same metallic masters as the thin G30.

Despite providing a higher electron density, metallic targets have a lower ionization threshold with respect to dielectric materials, hence they are supposed to suffer from early ionization by the laser pedestal [105]. This is possibly already revealed by the spatial distribution on the Lanex screen observed with Aluminized flat foils. The overall electron emission is more intense, yet the hole in the specular direction is barely visible, as if the target surface was damaged, rippled, or expanding.

Without any reproducible feature in the emission, it was also harder to find the best focal position to optimize the electron acceleration. Adjustments on the position of the Aluminized gratings $G30_{Alu}$ could result into a shift of ±100 μm with respect to the optimal position found for the simple Mylar flat foil. Despite such complications, $G30_{Alu}$ still produced an electron bunch in the tangent direction, as shown in figure 3.12.

	F_{Alu}	$G30_{Alu}$
$FWHM_\theta(°)$	-	7.0 ± 0.3
$FWHM_\phi(°)$	-	6.0 ± 0.2
Q (pC)	15 ± 4	28 ± 3
E_{peak} (MeV)	-	4.2 ± 0.1
E_{cutoff} (MeV)	-	10.5 ± 0.3
$\Delta\theta(°)$	2.5	0.7
$\Delta\phi(°)$	6	0.05

Figure 3.11: Distinguishing quantities of the emission from Aluminized targets.

The results of the usual bunch analysis are listed in the table 3.11 on the right-hand side. The measurements confirm that more charge is emitted from Aluminized flat foils with respect to bare Mylar foils, at the cost of a worse stability (compare table 3.1a). On the contrary, the bunch obtained with the Aluminized grating is broader along θ and it contains less charge with respect to the bare G30. A rough estimation of the total signal collected

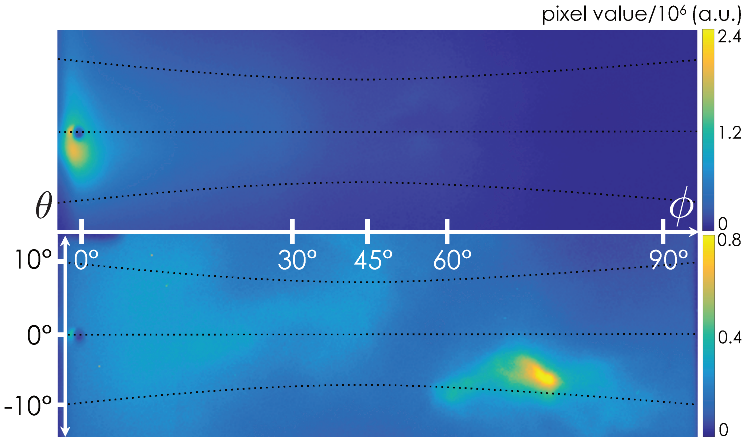

Figure 3.12: Electron emission from Aluminized targets, $\mathrm{G30}_{\mathrm{Alu}}$ (top) and $\mathrm{F}_{\mathrm{Alu}}$ (bottom). The color ranges are $[0, 2.4 \times 10^6]$ and $[0, 0.8 \times 10^6]$ as in figure 3.6.

by the whole Lanex shows that also the average emission from the $\mathrm{G30}_{\mathrm{Alu}}$ is weaker than the emission from the G30 by a factor of ~ 1.5. The maximum electron energy is reduced by a similar amount, in contrast with the theoretical model that predicts a growth of the maximum energy following the density increase ($\propto \sqrt{n_e}$ in equation 3.2 on page 52). These results suggest that a pre-plasma is likely to be created in the early moments of the laser-target interaction. Despite the Aluminized flat foils result in a higher yield of electrons, the emission is far from being reproducible, in contrast with other acceleration mechanisms that rely on an ad hoc pre-plasma generated in a controllable manner [11]. On the other hand, the pre-plasma extent may still be small enough not to wipe the grating grooves out and to allow for the SP excitation, although less efficiently. Similar evidence is presented in chapter 4, where simple G30s are pre-ionized with a low intensity laser pulse to investigate high order harmonic generation, which is known to be optimized with a suitable density gradient [121].

Solid gratings also have a thin Aluminum coating, yet the drawbacks on the electron emission are somehow mitigated by the overall higher efficiency achieved with blazed grooves. The properties of the electron bunch obtained in the tangent direction with all the solid gratings are resumed in figure 3.13 and in the table alongside. The graphs show the charge density and the cutoff energy as a function of the blaze angle. They both exhibit a peak in correspondence of 13°, which is the only angle optimized for a blaze wavelength of around 800 nm. Indeed, the curve of the cutoff energy particularly agrees with the efficiency values anticipated in table 2.2 on page 38. As a whole, solid gratings emits more charge than their thin counterpart, reaching ~ 660 pC in

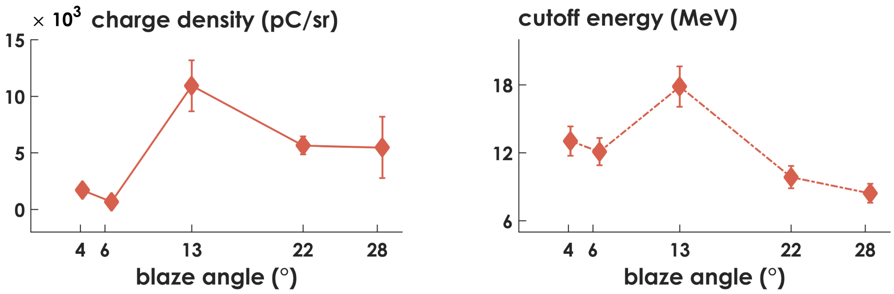

Figure 3.13: Charge density and cutoff energy as a function of the blaze angle. All solid gratings are irradiated at resonance (30°).

	SG4	SG6	SG13	SG22	SG28
$\mathrm{FWHM}_\theta(°)$	6.5 ± 0.6	9 ± 1	9.3 ± 0.9	9 ± 1	13 ± 1
$\mathrm{FWHM}_\phi(°)$	7.0 ± 0.37	5.8 ± 0.6	5.4 ± 0.5	4.7 ± 0.5	6.9 ± 0.7
Q (pC)	105 ± 10	45 ± 6	660 ± 80	330 ± 30	510 ± 100
$\mathrm{E}_{\mathrm{peak}}$ (MeV)	5.7 ± 0.6	4.3 ± 0.4	7.7 ± 0.8	3.7 ± 0.4	3.2 ± 0.3
$\Delta\theta(°)$	0.8	0.5	0.2	0.2	0.6
$\Delta\phi(°)$	0.05	0.05	0.05	0.05	0.2

Table 3.2: Properties of the surface electron bunch obtained with blazed gratings.

the best configuration (corresponding to a ×6.5 enhancement in comparison to the sinusoidal G30); on the contrary, the highest cutoff energy, ~ 18 MeV, is comparable with the results from the G30 and G45 shown in figure 3.10. Similarly to what is observed with the thin Aluminized $\mathrm{G30}_{\mathrm{Alu}}$, the electron bunches generally exhibit a poor collimation in the vertical direction (FWHM_θ) in spite of their remarkable stability in the position. Finally, table 3.3 refers to the SG13 oriented in the wrong direction, *i.e.* with the blaze arrow pointing towards the incident beam. This configuration still produces an electron bunch in the tangent direction, yet its unimpressive properties confirm the worse grating efficiency expected in this case.

	SG13 reversed
$\mathrm{FWHM}_\theta(°)$	11.6 ± 0.2
$\mathrm{FWHM}_\phi(°)$	5.8 ± 0.1
Q (pC)	19 ± 1
$\mathrm{E}_{\mathrm{cutoff}}$ (MeV)	7.6 ± 0.3
$\mathrm{E}_{\mathrm{peak}}$ (MeV)	3.8 ± 0.2
$\Delta\theta(°)$	0.5
$\Delta\phi(°)$	0.06

Table 3.3: Results for the SG13 in the wrong orientation.

By rotating the platform with the electron diagnostics around the target, the spectrometer measures the energetic distribution at different angles from the tangent. Coherently with the results presented so far, both the cutoff energy and the peak energy do not vary within few degrees from the tangent, corresponding to the FWHM$_\phi$ measured on the spatial distributions. This result supports the distinction between the region close to the target surface, $\phi < 10°$, which contains the whole electron bunch; and the region further outside, where the electron emission is significantly weaker and independent from the incidence angle of the laser pulse (whether it is the resonant one, or not). It is worth anticipating that the same angular ranges are identified in the ϕ-lineouts retrieved by the PIC simulations presented in the following sections.

To summarize this part, the experiments suggest that Aluminized gratings hamper the investigation of SP-related effects. Results obtained with bare Mylar targets exhibit better collimation and higher charge. At the same time, blazed grooves enhance the electron emission provided that the blaze angle is optimized for the laser wavelength and diffraction order propagating in the tangent direction. In this case, the Aluminum coating might still undermine the bunch divergence. Further tests with targets made of the same material could give more information about the highest efficiency achievable by playing with the grating properties. For the moment being, Mylar gratings seem to stand even higher laser intensities, as presented hereunder.

3.3.3 Electron acceleration in the PW regime

A separate experimental run was carried out in 2015 on the PW-class laser system hosted at the Gwangju Institute for Science and Technology (GIST, Republic of Korea), to assess the feasibility of SP excitation with laser intensities above 10^{20} W/cm^2. The same thin targets employed in France, G30 and flat Mylar foils, were irradiated at 30° of incidence and the electron emission was recorded by the usual Lanex screen Carestream: however, the detector was protected by a 3 mm thick Aluminum plate, so that only electrons beyond ~ 1.5 MeV reached the Lanex. The experimental setup allowed to investigate the electron emission only at 30° of incidence and without the electron spectrometer, because a distinct study on foam-attached targets was being realized during the same campaign [16]. Nevertheless, promising results on SP-driven electron acceleration were achieved.

The Ti:Sa CPA laser system PULSER (Petawatt Ultra-Short Laser System for Extreme science Research) delivers 1.5 PW, 45 J, 30 fs pulses at 0.1 Hz of repetition rate [122]. The laser chain is equipped with a DPM to reach a temporal contrast of $\sim 10^{-11}$ at 6 ps before the main pulse[6]. Taking

---

[6] This value has been reported at the output of the 100-TW beamline which bypasses the last amplification stage of the laser system [123]. A similar DPM is arranged at the output of the PW beamline [124].

into account the optical losses along the laser propagation, the final pulse contains ~ 15 J, focused by an $f/3$ off-axis parabola to ~ 4 μm FWHM. The final intensity on target is estimated to $\sim 7 \times 10^{20}$ W/cm^2.

The electron emission recorded from the G30 is shown in figure 3.14 for two different laser intensities. The spatial distribution has all the distinctive features described in the previous sections: a highly-collimated electron bunch is found in the incidence plane, along the target tangent; the trace of the specular reflection is visible in the image of the whole Lanex (not shown here). Once again, flat foils never produced any reproducible, intense electron bunch. Remarkably, the angular spread in the vertical direction is comparable with the results obtained with UHI100, *i.e.* FWHM$_\theta \simeq 5.5°$. Since a cross-calibration of the imaging systems used to record the Lanex pictures in France and in South Korea has not been realized, it is not possible to infer the amount of charge accelerated in these high-intensity laser shots. However, it is interesting to compare the maximum signal (in pixel counts) of the two shots displayed in figure 3.14, considering that the weakest one is closer to the experimental conditions of the French campaign. Direct measurements on the Lanex images indicate for the higher intensity a $\times 2.2$ increase of the maximum signal, which is of the same order of the a_0 increment (a linear scaling for the accelerated charge will be also discussed in figure 3.23b on page 77 for the measurements on UHI100).

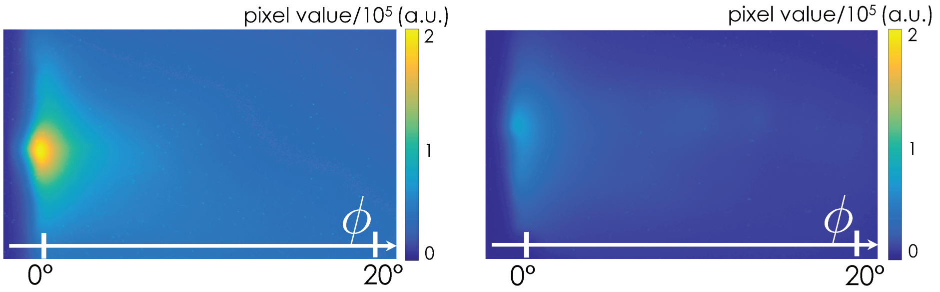

(a) $I \simeq 5 \times 10^{20}$ W/cm^2, $a_0 = 15$ (b) $I \simeq 8 \times 10^{19}$ W/cm^2, $a_0 = 6$

Figure 3.14: Electron emission from a resonant G30 measured during the experimental campaign at GIST. The color scale is normalized to the highest pixel value in image (a).

Eventually, these electron distributions suggest that the grating structure was preserved during the interaction, and support the full exploration of SPs even in the PW-regime.

3.4 Numerical simulations

The main purpose of the PIC simulations presented in this section is to examine the results of the experimental activity in a more controlled environment and to explore the role of some interaction parameters that become more accessible in the numerical scenario. Nevertheless, the choice of the initial parameters of the simulation is crucial to truly represent the phenomena under investigation. Given the numerous parametric scans performed for this work, the best compromise between the computational resources and the consistency with the experimental results was to carry out 2D simulations at moderate target density.

As already anticipated, 3D simulations are reported in [16], where they supported the very first experimental observation of surface electron acceleration [10]. Acceding all three dimensions allowed to reconstruct the whole spatial distribution of the electron emission along θ and ϕ, which reproduced remarkably well the signal collected by the Lanex screen. Other spatial features such as the emission widening for non-resonant incidence angles and the peak in the energetic spectra were obtained as well. Figure 3.15 shows the most significant results of the 3D numerical campaign. As far as this work concerns, PIC simulations are mainly required to investigate the comparison between gratings and the optimization of their characteristics. Therefore, the interest resides in addressing the maximum electron energies and the main properties of the spatial distribution, rather than reproducing the exact shape of the energetic spectra (for which 3D simulations turned out to be essential, [10]), or the finest details of the electron emission. Additionally, the predominant two-dimensional nature of SP excitation ensures that the 2D geometry is adequate for both of these purposes.

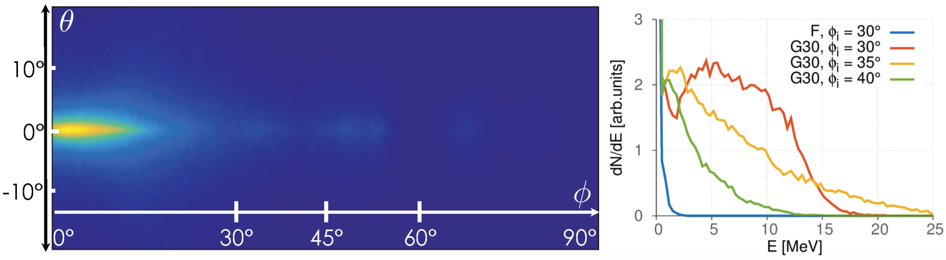

Figure 3.15: Results of 3D PIC simulations, from [16]: spatial distribution from a G30 irradiated at resonance and energetic spectra recorded at tangent for various incidence angles.

The main parameters of the simulations are listed in table 3.4.

One crucial parameter is the initial target density, $n_0 = 50n_c$, which is quite below the real value of a fully-ionized solid target ($\sim 400n_c$). In general, a smaller plasma density allows to reduce the computational cost of

Parameter	values
box size (x, y)	$100\lambda \times 100\lambda$
spatial resolution Δx, Δy	70 ppλ, 40 ppλ
boundaries	periodic
target density n_0	$50n_c$
particles per cell	128 electrons, 25 ions $(Z/A = 1/2)$
temperature distribution	Maxwellian, with temperature T
T/rest energy	10^{-8} for electrons, 10^{-10} for ions
target shape	flat, sinusoidal or blazed grating
target location	[0,thickness] $\times$ $[-50\lambda, 50\lambda]$
grating depth d	from 0.25 to 2λ
target thickness	2λ (scan from 1 to 5λ)
laser polarization	P
laser a_0	5
laser duration FWHM	$12\lambda/c$
laser waist	5λ

Table 3.4: Setup of the 2D PIC simulations.

the simulation and yet to mimic an overdense target. However, increasing n_0 would cause the SP's dispersion relation to weakly depend on the plasma density, and to narrow the range of incidence angles for which the electron acceleration takes place. This has been verified with a limited set of 2D simulations where the initial density was brought to $200n_c$ (and the spatial resolution was consequently increased by 4 times). With these simulations it was possible to ascribe some energetic electrons, observed in the low density simulations for non-resonant angles, to the target heating rather than to the excitation of a SP. The resonance curve presented at the beginning of this chapter in figure 3.1b is exactly the result of high density simulations, each one lasting $\sim$ 16 hours. For all the parametric scans presented in the following, instead, the initial density was kept to $50n_c$.

With regard to the target parameters, the selected thicknesses are once again smaller than the real value (which would be $\sim 16\lambda$). However, there is reliable evidence that electrons in the bulk do not contribute to the physical processes at the surface. Test simulations with a target thickness of 5λ were performed: the electrons from the target bulk were discriminated from the electrons within the area containing the grating. Regardless of the grating depth, the electrons from the bulk never produced a significant contribution neither to the energetic spectra in the tangent direction, nor to the spatial emission over the entire ϕ range. As a consequence, it was safe to always split the thickest targets in two regions, the grating and the substrate, and to assign fewer particle per cells to the substrate to relieve the computational load.

At the end of the simulations ($t = 55\lambda/c$), the electron phase-space is analyzed to infer the energetic spectrum in the tangent direction (centered at $2° \pm 1°$) and the angular distribution along ϕ (from 0° to 90°). Only the electrons emitted on the laser-irradiated half-space are considered (*i.e.* for $-50 < x < d/2$, with d the grating depth). Target absorption is estimated by comparing the fraction of energy possessed by all the particles in the box to the initial energy in the simulation. Other evidence of the SP-driven electron acceleration can be found by following the trajectories of some test macro-particles in the EM fields produced at the grating surface. Figure 3.16, reproduced from [16], shows two moments of the electron acceleration obtained on a G30 irradiated at resonance: at the beginning of the interaction, electrons are extracted at the grating surface by the intense laser; at the end of the simulation, high energy electrons are visibly directed towards the target tangent.

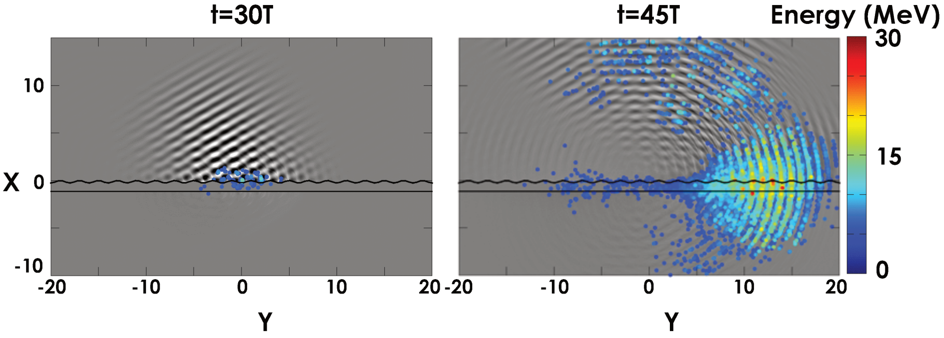

Figure 3.16: Snapshots of the surface electron acceleration obtained with a 2D PIC simulation, detailed in [16]. The $\hat{z}$ component of the magnetic field is drawn in gray, while macro-particles are represented with colored points. The color indicates the particle energy. The original grating profile is marked with black lines.

3.4.1 Influence of the grating depth

The grating depth is supposed to play a crucial role on the coupling between the target and the laser pulse. Corrugated and micro-structured targets are known to increase the laser absorption by various amounts [32], and also gratings irradiated at sub-relativistic intensities ($a_0 \sim 0.5$) have shown a ×3 increase of the electron emission with respect to flat foils [109]. In these cases, the enhanced absorption is typically explained in terms of a greater region of the target (either superficial or volumetric) than can interact with the laser pulse, giving rise to various non-linear phenomena (briefly recalled in section 1.1). In all these works, both the size and interspace between the micro-structures affect the absorption efficiency.

Simulations with variable grating depth and thickness were realized. In all of them, the grating has a period of 2λ and it is irradiated at the resonance angle 30°. Flat foils with the same thicknesses were tested as well. The number of electrons emitted in the tangent direction with energy above 5 MeV and the target absorption are shown in figure 3.17. As expected, all the flat foils produce a negligible amount of charge in the tangent direction, and the absorption is at least 2 times smaller with respect to the grating; there is no significant dependence on the foil thickness (which is within the μm range). On the other hand, gratings show two interesting trends: first of all, increasing the grating depth impairs the surface acceleration, but it improves the absorption; secondly, thicker targets produce fewer electrons without affecting the absorption. Both these results confirm that the target substrate has minor influence on the target efficiency. As far as the surface acceleration is concerned, the grating behavior agrees with the theory, where SPs are inferred in the limit of shallow gratings. Previous numerical works ascribe the drop of the efficiency also to shadow effects [112]. The slightly larger electron number obtained with the thinnest substrate can be explained in terms of electron recirculation across the target [114] (note that this effect might be negligible in the experiments, where real targets are too thick to be crossed multiple times by the electrons oscillating in the ultra-short laser pulse). With regard to the absorption, the increase with deeper gratings might be explained by geometrical effects rather than by the excitation of a SP, as already remarked in [9, 125].

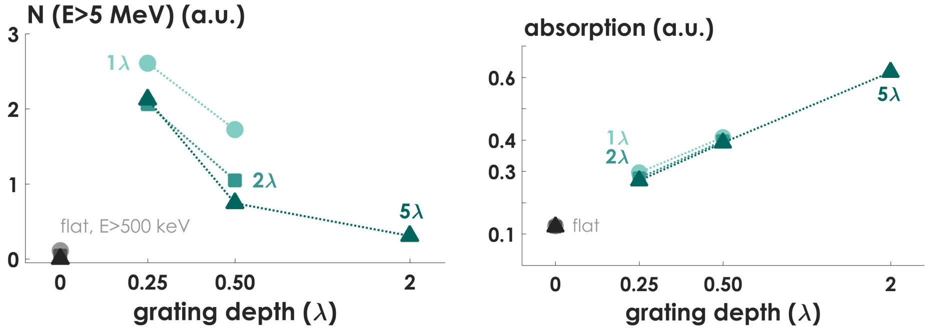

Figure 3.17: Number of electrons emitted in the tangent direction with energy > 5 MeV and absorption obtained from gratings with different depth-thickness combinations irradiated at resonance. Markers and colors specify the target thickness. Points for the flat target, with the energy filtered below 500 keV, are shown in comparison.

Further evidence in this sense comes from the peculiar electron distribution obtained from some of the aforementioned depth-thickness combinations. The angular profiles are shown in figure 3.18 with a selection of energy filters. The shallow grating irradiated at resonance (figure 3.18a) exhibits a distinctive emission in the tangent direction ($\phi < 10°$), which is quite consistent also when all the electrons below 10 MeV are filtered out. It is noteworthy that the angular extension of the most energetic electrons is limited to $\phi < 30°$, in agreement with the experimental results (compare 3.6a). On the contrary, the deep grating at resonance (figure 3.18b) produces a uniform emission in all directions; moreover, it clearly appears that the enhanced absorption only affects low-energy electrons, since no emission above 10 MeV is observed. Another missing feature is the electrons around the specular reflection of the laser pulse, which instead are quite visible on the shallow grating. This one is also shown for a non-resonant incidence angle (3.18c) to underline the huge decrease of electron signal, which remains, nevertheless, 10 times higher than the result from a flat foil (note the reduction of the vertical scale in figure 3.18d).

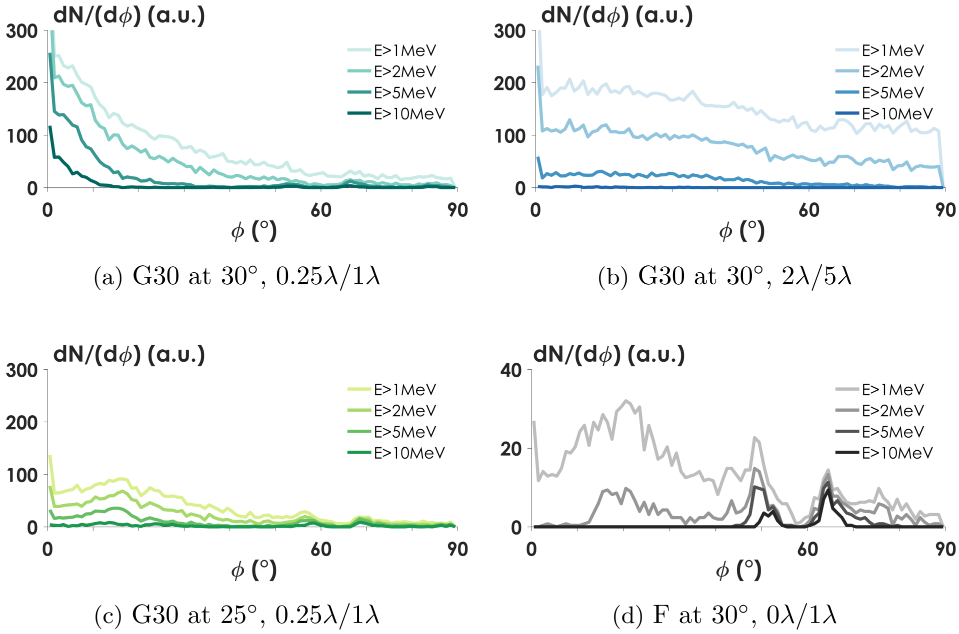

(a) G30 at 30°, $0.25\lambda/1\lambda$

(b) G30 at 30°, $2\lambda/5\lambda$

(c) G30 at 25°, $0.25\lambda/1\lambda$

(d) F at 30°, $0\lambda/1\lambda$

Figure 3.18: ϕ-lineouts of the electron emission, for various target configurations and energy filters. Each panel reports the combination of grating depth/target thickness.

Finally, the contribution of the SP is clearly revealed by analyzing the energetic spectra for different incidence angles. Figure 3.19 presents the number of electrons with energy above 5 MeV collected in the tangent direction for two different G30s. Similarly to figure 3.9, the shallow grating

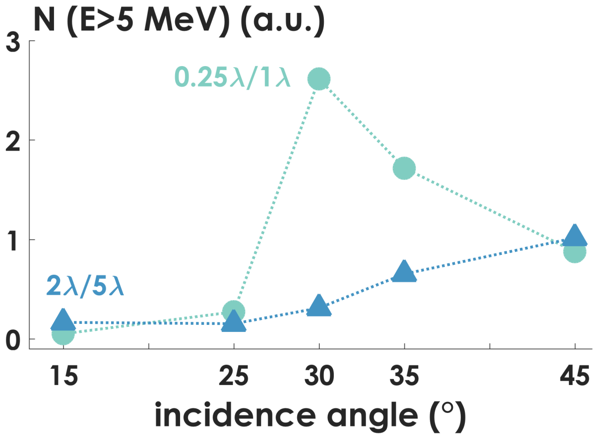

Figure 3.19: Electrons above 5 MeV accelerated in the tangent direction as a function of the incidence angle. Both targets are G30, with depth/thickness indicated next to the curves.

shows a dramatic increase of the surface electrons when the incidence angle corresponds to the resonant one; on the other side, the results for the deepest grating allow to exclude any excitation of a SP, since the number of energetic electrons only increases with the incidence angle, and no significant effects are found at 30°. Note that the number of energetic electrons injected in the tangent direction does not necessarily mean that the target absorption increases with the same trend [56]. The absorption of the shallow grating raises by little amount with the incidence angle, exhibiting a ×2 increase in correspondence of the resonant angle. With the deep grating, instead, the absorption decreases for large incidence angles, probably because the diffracted fields are impaired by the grooves (but the average absorption is still ~ 2 times higher than with the shallow grating, in agreement with figure 3.17).

In conclusion, a detailed scan of the grating depth and thickness confirms that only shallow gratings are best-suited for the excitation of SP and, consequently, for surface electron acceleration. Deeper gratings lead to higher absorption efficiencies to the detriment of the electron acceleration. The thickness of the substrate has only a minor influence to the overall target efficiency with respect the grating depth.

3.4.2 Grating comparison

In the attempt to explain the differences found in the experiments amongst the various gratings, their accurate depth was implemented in the numerical simulations: 0.21λ for the G15, 0.36λ for the G30, 0.46λ for the G45. For solid gratings, PICCANTE automatically calculates the groove depth once the blaze angle is specified. For all those cases, the target thickness was fixed at 2λ, in order to leave at least 1λ of bulk even for the deepest solid grating (SG28).

The energetic spectra and the angular distribution for the thin gratings irradiated at resonance are shown in figure 3.20. In agreement with the experimental results (figure 3.10), all the gratings exhibit a similar spectral profile, with comparable maximum energies. The tail of low-energy electrons has been observed to decrease with 3D simulations (compare [10] and figure 3.15), suggesting that a spatial selection in the θ dimension is essential to recover the experimental shape of the spectra. Furthermore, increasing the target density in the simulations would reduce the noise of the profiles, as illustrated by figure 3.1b at the beginning of this chapter.

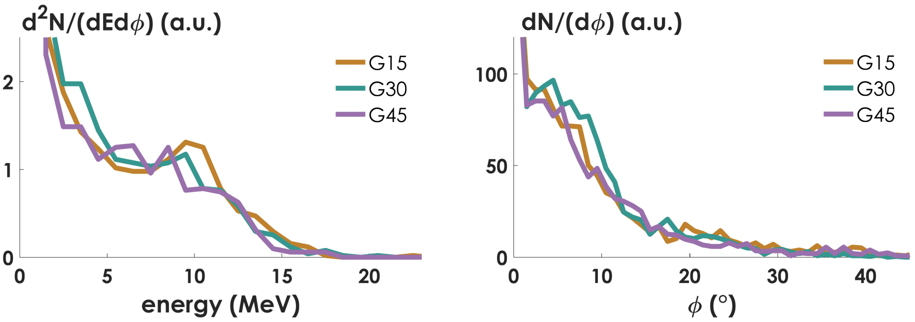

Figure 3.20: Energetic spectra and angular profiles of the electron emission from simulated thin gratings. The ϕ lineout includes only electrons with energy > 5 MeV.

More interestingly, the amount of charge emitted in the tangent direction ($0° < \phi < 10°$) appears to be independent from the grating type, *i.e.* the resonant angle does not affect the electron acceleration. To further investigate this point, a scan of the groove depth was realized for each thin grating. It turns out that the G45 needs to be deeper than the G30 and the G15 in order to produce an equivalent amount of charge, as well as to attain the same maximum energy in the spectrum. Here, the maximum energy is defined where $\mathrm{d}^2N/(\mathrm{d}E\mathrm{d}\phi)$ corresponds to 10% of its value at 1.5 MeV (this being the lower energy detected by the spectrometer in the experiments). Those results are shown in figure 3.21. Both plots indicate that there exists a definite range where the grating depth optimizes the surface wave, although there is a limit to the maximum efficiency achievable with sinusoidal gratings. Further improvement is obtained with blazed gratings, as already pointed

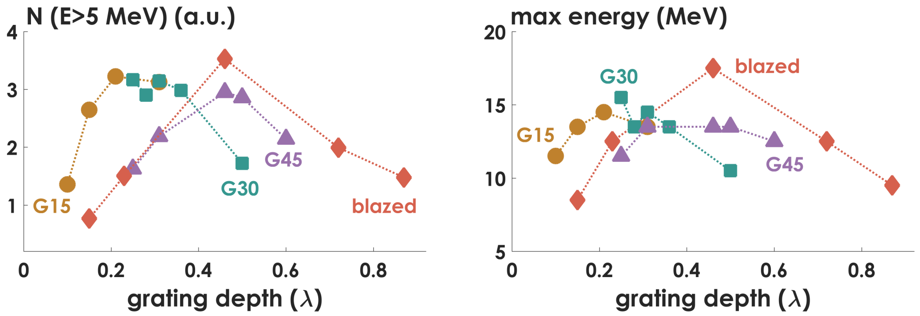

Figure 3.21: Depth scan on gratings with different periods. Both the number of electrons above 5 MeV emitted at tangent and the maximum energy attained by the spectra are optimized within a certain depth range.

out in the experiments and confirmed by the simulations shown in figure 3.21. The SG13 is again the most efficient one, with maximum energies up to 18 MeV; the number of energetic electrons is 2 times higher than what is produced by a sinusoidal grating with a similar depth ($\sim 0.5\lambda$). However, when comparing the SG13 with the best performances of the G30, the yield of the blazed grating is barely 10% higher. This suggests that reaching higher energies or charges would require more intense laser pulses, as discussed in the next section.

A final observation concerns the number of grating periods illuminated by the laser pulse, which depends both on the groove spacing of the grating and on the incidence angle. In one additional simulation, the energetic spectra from a G30 and a G45 were compared: the G45 had the same depth of the G30 and the laser waist was enlarged so that the focal spot would cover the same number of grating periods irradiated on the G30. The peak intensity was kept at $a_0 = 5$. As result, both the number of electrons emitted at tangent and their energies were lower with respect to the G30. Once the depth of the G45 was restored to the optimal value, the emission turned again equivalent to both the G30 and the G45 irradiated with fewer grating periods (as it happens in the experiment).

To summarize, implementing the real values of the significant grating properties in the simulations allows to identify the optimal conditions for electron acceleration. Regardless of the grating period, and thus of the number of illuminated lines, there exists a best groove depth where the efficiency of the sinusoidal gratings is maximum. Greater charge or higher energies are achievable with blazed gratings, provided that the blaze angle is optimized to convey the maximum diffracted power along the target surface.

3.4.3 Scan of the laser conditions

Evaluating the performances of SP excitation with different laser characteristics might unravel some experimental observations, as well as disclose engaging trends or scaling laws in support of experiments on other laser facilities.

A first set of simulations verified the influence of some experimental conditions on the laser-grating interaction, such as the target position with respect to the focal point of the laser beam, and the phase of the grating profile where the pulse strikes the target (either on a peak, on a valley, or halfway between them). The target implemented in all these simulations is a G30 irradiated at 30°, with groove depth 0.36λ and substrate thickness 2λ. It turns out that the phase has no influence on the electron acceleration over the entire ϕ range. Besides, a ± 50 μm shift of the focal position leads to $\sim 40\%$ fluctuations on the charge emitted along the tangent and ± 2 MeV on the maximum energy.

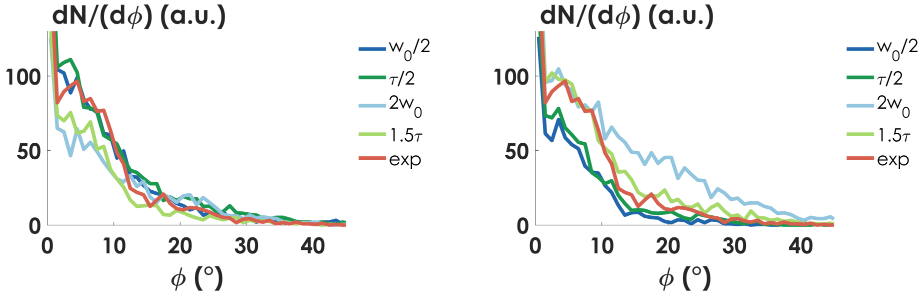

(a) fixed E_{L} (b) fixed I_{L}

Figure 3.22: Angular profiles of the electron emission from a G30 irradiated at resonance with different laser pulses. Electrons with energy smaller than 5 MeV are filtered out.

Figure 3.22 reports the angular profiles from a further group of simulations, with different beam waist (blue curves) and pulse duration (green curves). The profile obtained with the usual parameters of the experimental campaign (compare table 3.4) is added in red for comparison. The left panel shows the cases with fixed laser energy: higher intensity configurations, *i.e.* with reduced waist or duration, exhibit efficient tangent acceleration. On the right-hand side, the laser intensity is constant: visibly, the higher the energy, as required by the configurations with larger waist or duration, the higher the number of energetic collimated electrons along the surface. Basically, these results confirm that the laser energy dictates the efficiency of the SP excitation. Also, the number of illuminated grating periods is not significant: actually, figure 3.22b shows that larger focal spots degrade the angular profile, with more electrons emitted far from the tangent ($\phi > 10°$).

Finally, the electron acceleration is tested for increasing laser intensities. Figure 3.23a illustrates the results for the charge and maximum energy obtained in the tangent direction. Both quantities exhibit a linear trend for increasing a_0, in agreement with the theoretical model presented at the beginning of this chapter. In particular, electrons up to 30 MeV are obtained for a laser intensity $\sim 10^{21}$ W/cm^2 , which is far within the reach of many current laser facilities.

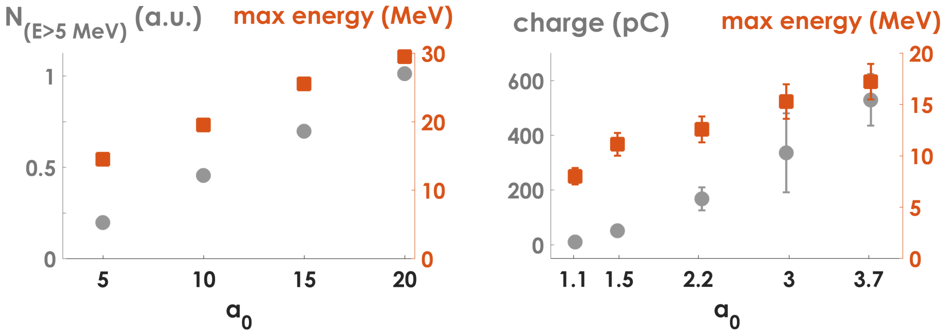

(a) simulation (b) experiment

Figure 3.23: Electron emission as a function of the laser intensity. (a): number of electrons above 5 MeV and maximum energy resulting from PIC simulations. (b): charge amount and cutoff energies measured during the experiment on UHI100.

For analogy, figure 3.23b shows a similar a_0 scan collected during the experiments with UHI100. In this case, the laser energy was reduced by an attenuator placed before the compressor; since the full laser energy corresponds to $I_L \sim 3 \times 10^{19}$ W/cm^2 delivered to the target, the range $30 - 100\%$ gives a_0 between 2 and 3.7. The target is a solid grating SG13, irradiated at resonance. The amount of charge and the cutoff energy are estimated from the images of the Lanex screens as explained in the previous section. As usual, error bars represent the standard error on the sampled images, except for the points at lowest laser energy where the extremely poor signal prevented from collecting many shots. In this case, the error bar is given by the absolute error gathered when deconvolving the experimental images into energy and charge values; for the points at $a_0 = 1.1$, 1.5 the error bars on the charge (corresponding to $\sim 25\%$ of the mean) are not visible because of the large scale of the vertical axis. The experimental results also increase linearly with a_0; it is worth noticing that the maximum energies actually measured in the experiment are well reproduced by the simulations, as already pointed out in figure 3.20.

These results, together with the ones collected at GIST, definitely encourage to pursue the experimental activity with more powerful laser installations.

3.5 Conclusions

This chapter has given striking evidence of the excitation of SPs in the relativistic regime, by analyzing their role in accelerating bunches of energetic electrons along the target surface.

It is worth reminding that prior to this demonstration [10] no other experiment had addressed plasmonic effects at relativistic laser intensities, mainly because the resonant coupling was prevented by the poor laser contrast. On the other hand, relativistic SPs had been explored by numerical simulations, with the result that the enhancement of the local electromagnetic field at the target surface was mainly suggested as a scheme to support ion acceleration (hence focusing on energetic electrons *re-injected* in the overdense plasma). In this context, the results presented here mark the first steps in the new domain of Relativistic Plasmonics.

Gratings irradiated at the resonant angle for SP excitation produce a highly-directional, bright emission of energetic electrons. Either varying the incidence angle or spoiling the laser temporal contrast nullifies the electron acceleration, clearly demonstrating the correlation with the surface waves. A thorough scan of the grating parameters (period, shape, material) allows to identify the most efficient target: the grating whose blazed angle has been optimized for the laser wavelength (in the Littrow configuration, as explained in chapter 2) results in ~ 650 pC of charge and cutoff energies of ~ 20 MeV. In comparison, flat foils emit broad electron clouds with randomly-placed bright peaks: however, the charge of these latter is rarely beyond ~ 5 pC. The grating material has a minor role provided that the laser contrast is high enough to prevent the early ionization of the modulated profile. Because of this, dielectric gratings manufactured from thin Mylar foils show a better yield with respect to Aluminized ones.

Dielectric gratings have proven to withstand even laser intensities above 10^{20} W/cm^2, in the course of preliminary measurements realized on a PW-class laser system. Although a cross-calibration with the results obtained in France was not possible, there is reasonable evidence of a linear increment of the charge amount with the laser intensity.

The same trend is predicted by 2D PIC simulations, which evaluated the role of different laser and grating parameters not available in the laboratory. The most interesting results concern the role of the grating depth, which is hardly considered in the derivation of the SP's dispersion relation. It turns out that there is a range of values for the groove depth where the electron acceleration is equally efficient; further improvement is achieved again with blazed profiles. With regard to the laser parameters, the best-quality electron bunches are obtained with highly-focused, long laser pulses.

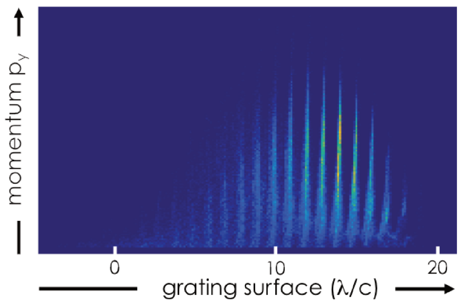

Figure 3.24: Electron phase space from the 3D PIC simulation. The output is analyzed at $25\lambda/c$, before the spatial modulations are lost due to the mixing of the trajectories.

The remarkable properties of the SP-accelerated electron bunches allow to contemplate their applicability as a bright, laser-synchronized, ultra-short electron source at modest energies. However, both the details on the acceleration mechanism and the bunch properties require further characterization and, most likely, optimization. With regard to the experimental features, measuring the bunch duration would give more insight on the acceleration mechanism, for instance on the lifetime of the SP. PIC simulations reveal from the electron phase space that the acceleration along the tangent direction has a duration comparable with the laser's one; moreover, micro-bunches of energetic electrons are clearly emitted at each laser cycle. These structures are visible in figure 3.24, which is obtained from the 3D simulation described in [16]. However, resolving the micro-bunch duration in the laboratory would pose many conceptual and technical challenges, as the broad energetic spectrum would cause electrons ejected at different laser cycles to overrun each other and erase the temporal modulation after traveling few-micron distances[7]. From the point of view of the source optimization, the energy spread is far from being competitive with common laser-plasma accelerators based on the wakefield mechanism, which report energy spreads routinely below 10% [1]. However, the same accelerators hardly provide energies be-

---

[7] An exploratory test based on the measurement of CTR was performed at CEA. CTR stands for Coherent Transition Radiation and refers to the radiation emitted when a bunch of energetic charges crosses a thin metallic foil. In correspondence of a wavelength comparable or larger than the bunch size, the intensity of the emitted radiation increases proportionally to the square number of the particles in the bunch [126]. The size of a micro-bunch accelerated at relativistic velocities within a laser cycle is comparable to the laser wavelength. Therefore, the first serious drawback of the CTR approach was that the detector (typically a high-dynamic CCD) had to be accurately shielded from the laser light reflected or transmitted by the plasma. Secondly, the estimation of the bunch broadening during the propagation required to place the thin metallic foil at less than 250 μm from the laser-irradiated point. Although adapting the experimental arrangement to this last constraint, the measurements did not provide any convincing evidence of CTR caused the micro-bunching of the SP-driven electron emission. Note that due to temporal and cost limitations, the analogous measurement in the mid-IR range (which should identify the size of the entire ~ 25 fs-bunch) has not been carried out.

low 50 MeV and charge amounts above 100 pC. For these reasons, and for the possibility to design high-repetition-rate target mountings, SP-driven electron acceleration is definitely going on for many promising applications.

Chapter 4

Enhanced High-order Harmonic generation

The nonlinear interaction between an intense laser pulse and an overdense plasma accounts for the generation of High-order Harmonics (HHs) of the incident laser frequency. According to the dominant process in the relativistic regime, nonlinear, collective electron oscillations driven by the laser field at the plasma surface act as source of high harmonics. As SPs enhance the EM field at the target surface, faster oscillations are expected to boost the harmonic spectrum to higher frequencies.

This chapter describes the very first experiment of HH generation from grating targets irradiated at relativistic intensities at the resonant angle for the excitation of SPs. In these conditions, the harmonic spectrum collected along the grating surface turns out to attain higher frequencies compared to the specular emission normally achieved with flat targets. Moreover, the intensity of the highest harmonic order is similar for both targets, with the advantage of harmonics spatially separated due to diffraction. Finally, all these results have been obtained with a short, expressly pre-formed density gradient in front of the overdense target; therefore, they demonstrate also the possibility to manipulate the grating profile on a nano-metric scale without hampering the SP excitation. In support of this, electron beams of ~ 10 MeV energy are still accelerated along the target surface.

This chapter is structured as follows. The first part introduces the main mechanisms of HH generation from overdense plasmas, with particular attention to the role of the density gradient in their efficiency. The relevancy of grating targets to HH emission is discussed in the second section, which also summarizes some results of 2D PIC simulations that firstly investigated SP-related effects and stimulated the experimental campaign [14, 16]. Sections 4.4 and 4.5 detail the experimental results and further numerical simulations realized in their support. Last section is reserved to few closing remarks.

4.1 Laser-based harmonic sources

The interaction of a laser pulse with atoms, free electrons or solids generate coherent, phase-locked harmonics of the laser frequency. For a Ti:Sa laser, having $\lambda \simeq 800$ nm, harmonic orders from $m = 8$ to $m = 80$ covers the eXtreme Ultra-Violet (XUV) range of the electromagnetic spectrum; so, provided they have enough intensity, HHs are suitable to pump and probe experiments of ultra-fast dynamical systems like atoms and molecules [127]. Broadening the harmonic spectrum to higher frequencies also allows for the generation of attosecond pulses, which have unprecedented temporal resolution [128–130]. At present, harmonic sources of isolated attosecond pulses have been demonstrated experimentally both with gaseous [131] and solid [132] laser-irradiated targets.

The main drawback of employing gaseous targets in laser-based HH sources is the low generation efficiency, which can be explained in simple terms of the same ionization threshold discussed in chapter 1. HH generation in gaseous targets relies on atomic re-collisions experienced by the electrons which, after tunneling through the Coulomb potential, are accelerated by the external laser field and, as the this one changes sign, go back to their parent ions [133]. But if the laser intensity overcomes few 10^{15} W/cm^2, re-collisions are prevented by the heavy ionization of the target electrons. Therefore, increasing the harmonic yield requires to deal with highly-ionized nonlinear media, such as overdense plasmas driven by relativistically intense laser pulses [22]. As there are no a priori limits to the incident laser intensity in this case, it expected for the current PW-class lasers to strongly enhance the HH intensity as well as to extend their overall spectral range.

4.1.1 HH generation from solid targets

As it happens for electron acceleration from overdense plasmas, also HH generation has been described in terms of various mechanisms. Generally speaking, the harmonic emission is set up by the electron motion across the vacuum-plasma boundary, which ultimately depends on the laser intensity and the plasma density gradient. In particular, the role of the latter has been identified mostly by experimental and numerical observations [22, 121]. In principle, with a small amount of pre-plasma the laser field encounters a near-critical region where to drive large electron oscillations, provided that the local plasma frequencies are close to the laser's one. Similarly, electrons within a inhomogeneous plasma are expected to have many different initial conditions, hence more chances to be in phase with the driver field and to be efficiently accelerated[1].

Following these coarse yet helpful guidelines, this section provides the main features of the most significant mechanisms that characterize HH generation with ultra-short laser pulses [2, 22, 82, 134]. A scheme of these processes is also given in figure 4.1.

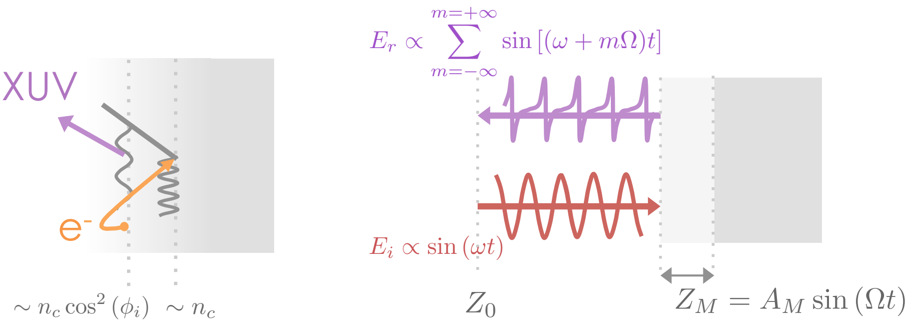

(a) Coherent Wake Emission

(b) Relativistic Oscillating Mirror

Figure 4.1: (a): in CWE, hot electrons re-injected in the overdense plasma trigger plasma waves that radiate at the local plasma frequency [82]. (b): in ROM, the reflected laser pulse contains HHs because of the retardation effect caused by the mirror displacement [135].

Coherent Wake Emission

Coherent Wake Emission (CWE, figure 4.1a) is considered the dominant mechanism at non-relativistic intensities, *i.e.* $a_0 \leq 1$ [82, 136]. This process arises from the resonant coupling between the electromagnetic waves (*i.e.* the harmonics) and electrostatic plasma oscillations driven by the hot electrons

---

[1] The advantage of adding a short pre-plasma to enhance the vacuum heating mechanism has also been explored by numerical simulations reported in [17].

that re-enter in the density gradient. As these hot electrons are provided by the vacuum heating mechanism (section 1.1), CWE is already operating at $I \sim 10^{15}$ W/cm^2, and the generation efficiency scales linearly with a_0.

Studying the electron trajectories inside a plasma density gradient $n(z) = n_0 e^{-z/L}$, with L the scale length introduced in 4.4 on page 90, it is possible to show that the frequencies of the emitted harmonics are proportional to the local plasma density $\omega_p(z) = \omega(n_e/n_c)^{1/2}$; as a consequence, the maximum attainable frequency is found when $n_e = n_0$, which is $\gg n_c$ for overdense plasmas. For example, for fully-ionized Silica it is $n_0 \simeq 400 n_c$, so that the maximum m^{th} harmonic order is $\omega_m/\omega \simeq \sqrt{400} = 20$.

The CWE occurs only when a short plasma gradient (typically below 0.1λ) precedes the overdense region. On one side, the limit $L \sim 0$ corresponds to a homogeneous plasma, where it can be demonstrated that the electrostatic oscillations do not couple into radiating light [22]. On the other side, large scale lengths decrease the efficiency of the vacuum heating process, which in turn affects the amplitude of the plasma wakes.

Relativistic Oscillating Mirror

The *Relativistic Oscillating Mirror* (ROM, figure 4.1b) accounts for HH generation in the relativistic regime [135, 137]. This mechanism owes its name to the fact that the plasma electrons oscillate across the interface with vacuum at relativistic velocities, driven by the Lorentz force associated to the incident EM field. In this way, the reflected laser pulse undergoes a frequency upshift caused by the Doppler effect.

In order to account for the nonlinear generation of higher harmonics, it is useful to mention the expression of the electric field reflected by the relativistic oscillating mirror [2, 128]. For simplicity, let the laser field $\propto E_0 \sin(\omega t)$ impinge at normal incidence on the mirror, whose position along z is described by an oscillatory function $Z_M(t) = A_M \sin(\Omega t)$. A photon starting at t from an initial position Z_0 will arrive at the mirror at $t' = [t + Z_0/c + Z_M(t')/c]$ and, after reflection, reach back Z_0 at $t'' = [t' + Z_0/c + Z_M(t')/c]$. For small oscillations, *i.e.* $A_M \ll \lambda$, the mirror displacement during $t' - t$ can be neglected, so that $Z_M(t') = Z_M(t)$. The electric field in Z_0 at t'' will be then:

$$\begin{aligned} E_r \propto E_0 \sin(\omega t'') &= E_0 \sin\left[\omega\left(t + \frac{2Z_0}{c} + \frac{2A_M}{c}\sin(\Omega t)\right)\right] \\ &\propto \sum_{m=-\infty}^{m=+\infty} J_m\left(\frac{2\omega A_M}{c}\right) \sin\left[(\omega + m\Omega)t\right]. \end{aligned} \tag{4.1}$$

In the last passage, J_m are Bessel's functions.

Therefore, the reflected field is clearly nonlinear and its spectrum contains the higher harmonics of the mirror frequency Ω. Coming back to the laser-plasma scenario, where the mirror is the overdense plasma put in motion by the incident pulse itself, Ω depends on the dominant frequency of the external driver: in case of vacuum heating (*i.e.* P-polarization and oblique incidence), the mirror oscillates at ω, and the HH spectrum will include all the harmonics; oscillations at 2ω, due to the J×B heating (compare the expression for the magnetic force 1.15 on page 16), will produce a HH spectrum of purely odd harmonics.

In any case, at a given instant t the frequency of the reflected laser pulse will depend on the velocity of the mirror $v(t) = c\beta(t)$. Hence, the relativistic Doppler factor gives an estimate of the cutoff frequency in the ROM-generated spectrum for the maximum mirror velocity $\beta_{\max}$:

$$\frac{\omega_{\max}}{\omega} = \sqrt{\frac{1+\beta_{\max}}{1-\beta_{\max}}} \xrightarrow{\beta_{\max}\to 1} 4\gamma_{\max}^2.$$

The asymptotic limit for $\beta \to 1$ confirms that the more intense the incident pulse, the faster the electron oscillations, the higher the cutoff frequency. In reality, taking into account the actual duration and spatial extent of the electron bunches during the plasma oscillations allows to infer a different scaling, where the maximum frequency is proportional to $\gamma_{\max}^3$[2]. In the same limit, the intensity of the m^{th} harmonic is expected to decrease as $m^{-8/3}$ [139]; although this trend has been reported in experiments for HHs spectra extending up to $m \sim 3000$ at $I \simeq 10^{20}$ W/cm^2 [140], there is evidence of its inaccuracy when considering even more details of the laser-plasma interaction, such as the surface deformation induced by the radiation pressure [141] or the bending of the electron trajectories due to the magnetic field. This latter effect, in particular, accounts for a slower increase of the electron γ factor with a_0 ($\gamma \propto a_0^{0.4}$ according to the simulations in [22] instead of $\gamma \propto a_0$ as in equation 1.8 on page 10). At the same time the intensity of the HHs appears to saturate for $I\lambda^2 \sim 10^{20}$ Wcm$^{-2}\mu$m^2.

As a final remark, it is important to underline that also the ROM mechanism is more efficient for a certain length of density gradient, which turns out to be around $\sim \lambda/10$. This is caused by interplay between the Lorentz force which pulls the electrons out of the plasma, and the space-charge electric field that recalls them inside the target. Since this latter is proportional to the plasma frequency $\omega_p^2 \propto n_e$, sharp solid targets (*i.e.* $L \sim 0$) "hold back" the oscillating mirror, whereas for too outstretched plasmas the mechanisms of electron acceleration become less efficient.

---

[2] A cutoff frequency $\propto \gamma^3$ also characterizes synchrotron radiation. Coherent Synchrotron Emission (CSE) is indeed another mechanism accountable for HH generation in the relativistic regime. Unlike ROM, CSE requires ultra-short density gradients, which are normally unattainable in the interaction of solid targets and multi-cycle laser pulses. Nevertheless, CSE-generated harmonics have been observed in the spectrum transmitted across ultra-thin foils [138].

Comparison of the two mechanisms

At the onset of the relativistic regime, $a_0 \simeq 1$, the HH spectrum will contain contributions from both the CWE and the ROM mechanisms.

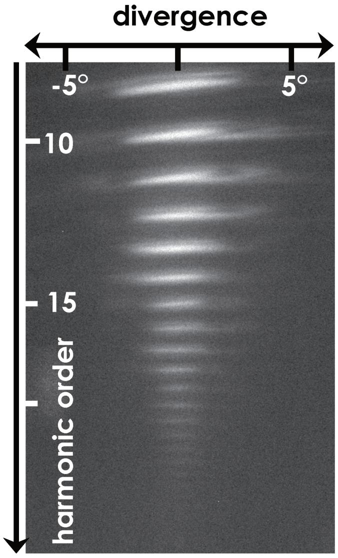

Figure 4.2: HH emission from a flat target, $I \simeq 3 \times 10^{19}$ W/cm^2.

Qualitative differences allow to discriminate the harmonics originating from each of these processes [142]: first of all, the CWE spectrum reaches at most the cut-off frequency $\omega(n_0/n_c)^{1/2}$; secondly, CWE-generated harmonics have a larger angular divergence [143]. Figure 4.2 shows an harmonic spectrum from the experimental campaign described in the following sections. The intensity delivered by UHI100 on the flat target is $\sim 3 \times 10^{19}$ W/cm^2, yet a weak CWE contribution is still visible at the lowest orders (9$^{\text{th}}$ to 15$^{\text{th}}$). Harmonics generated by the ROM process are more intense and narrower, and attain higher frequencies. Interestingly, for the harmonic orders where the CWE and ROM emission overlap, regions of destructive interference produce a dark corona around the ROM signal, as also remarked in PIC simulations [22].

Since the CWE and ROM mechanisms are optimized for different plasma density gradients, experiments usually resort to the control of the gradient scale length to split the CWE and ROM contributions [121, 144]. As this is also the approach adopted in this work, section 4.3 provides further details about the creation of a controlled pre-plasma on the target surface and the corresponding experimental setup.

4.2 Previous results about HHs from grating targets

The harmonic spectra generated with the mechanisms discussed in the previous section consist of a train of pulses whose intensity is dominated by the first harmonic order (*i.e.* the laser frequency). However, realizing near-monochromatic sources is of potential interest for various applications in the XUV range, such as photo-electron spectroscopy and coherent diffraction imaging [145]. To this aim, HH generation from grating targets has been investigated as a valid alternative to interferometric filters and expensive monochromators [15].

The very fundamental principle is that a grating will diffract the m^{th}

harmonic order according to the well-known grating equation

$$\sin(\phi_i) + \sin(\phi_{nm}) = \frac{n\lambda}{m\Lambda}, \tag{4.2}$$

where Λ is the grating period and ϕ_{nm} the angle of the n^{th} diffraction order. As a consequence of this equation, for fixed incidence and emission angles, the same diffraction orders correspond to different harmonic orders depending on the grating period [146]. Just as significantly, shaping the grating profile is expected to increase the efficiency of a chosen diffraction order, as already described in section 2.3.1 [15]. Note that because of the ratio n/m in the expression 4.2, all integers multiples of a chosen frequency will be diffracted at the same angle: however, their intensity is expected to be negligible (mainly because they are diffracted over more orders and, for ROM-generated harmonics, the intensity decreases at higher frequency).

4.2.1 Plasmonic enhancement

It is no surprise that experiments on SP-enhanced HH generation have been carried out at low ($I \leq 10^{12}$ W/cm^2) laser intensities [66, 147–150]. Generally, these works explore how small-scale metallic structures (*e.g.* bow-ties, tapered waveguides) allow for the excitation of SPs, so that the local EM field is amplified enough to generate HHs on a surrounding gas jet.

When stepping into the relativistic regime, no experimental study has yet assessed HH generation from grating targets irradiated at the SP resonance. The harmonic emission along a sub-wavelength grating surface experimentally reported by M. Cerchez et al. [146] has been formulated in terms of the constructive interference of the radiation emitted by the laser-accelerated electron across the grating grooves [151]. The interaction parameters, in any case, excluded any SP excitation. The experimental findings reported in the following sections investigate, therefore, a completely overlooked domain.

Before embarking on the experimental campaign, significant evidence of SP-enhanced HH emission was reported in fully-relativistic 2D PIC simulations performed by L. Fedeli [14, 16]. The spectral content of the EM field reflected by flat and grating targets irradiated at various incidence angles was analyzed to detect the contribution of SPs. Some meaningful results are shown in figure 4.3. The left panel compares the intensity of the $m = 10$ harmonic order obtained with a either a flat or a grating target, as a function of the incidence angle. Similar curves are reported for other harmonic orders in [14]. The grating period is 2λ, designed for a SP resonant angle of 30°; the intensity is integrated over the whole half-space in front of the target, $[-90°, 90°]$ with the same geometry presented in figure 1.5a on page 22 (compare the expression 4.6 in the following section). The grating exhibits a resonant curve in remarkable analogy with the results on the electron acceleration (figure 3.1a, for instance). The peak is found for $\phi_i = 35°$, a

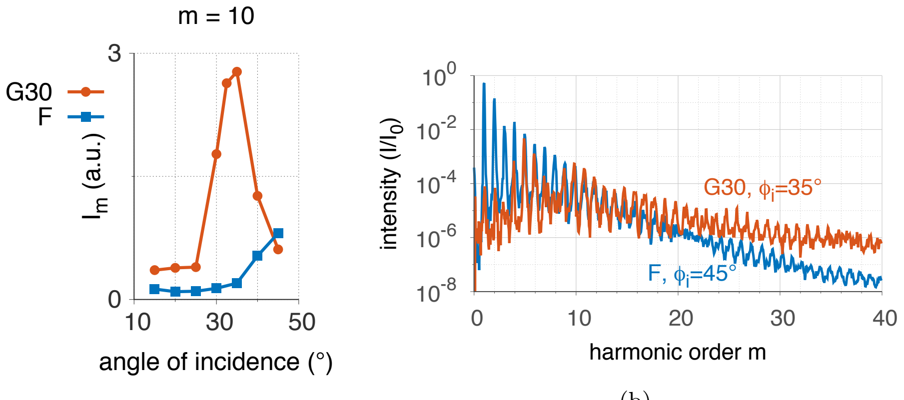

(a) (b)

Figure 4.3: PIC results for HH generation in the relativistic regime ($a_0 = 15$). (a): integrated intensity of the $m = 10$ harmonic order emitted by a grating G30 and a flat target, as function of the incidence angle. (b): harmonic spectra along preferred emission angles (82° for G30 and 45° for F) for the most efficient laser incidences. Reported from [14].

slightly larger angle than the expected resonance, where the signal exceeds by more than one order of magnitude the emission from the flat target. This one increases for larger incidence angles, consistently with the increase of the electric field component that is normal to the target surface (and accelerates the energetic electrons according to the vacuum heating model) [22].

The graph on the right, instead, shows the entire HH spectrum recorded along specific directions, integrated over an angular range of ±2.5°. For the G30, the emission is centered at 82°, *i.e.* very close to the target surface, while for the flat target all the harmonics are directed along the specular reflection. The key point of the comparison is that the emission from the grating overcomes the one from the flat target, especially at higher harmonic orders.

The combination of both plots clearly proves a SP-related HH enhancement: first of all, at the resonant angle the overall harmonic intensity is increased; secondly, higher orders in the spectrum are more intense with the resonant grating than with the flat target. Considering that such harmonics are not emitted in the specular direction, the contribution of the fundamental laser frequency is automatically ruled out.

It is worth mentioning that however promising these results might be, the simulations entirely disregarded the role of the plasma density gradient. The most challenging aspect of the experimental campaign would then be to efficiently generate HHs without hindering the SP excitation with a pre-ionized, wiped-out grating.

4.3 Creating a controlled pre-plasma

The HH generation is found to be optimized if a small amount of pre-plasma is added to the target surface. As introduced in section 1.1.2, the extension of such a pre-plasma is described by the gradient scale length L_{pp}, representing the distance from the unperturbed target surface where the plasma density has decreased by $1/e$ of its maximum, following an exponential profile along the target normal. In the laboratory, the pre-plasma is created with a low intensity laser pulse which irradiates the target some delay before the arrival of the main laser pulse. The pre-plasma formation is entirely mastered by controlling the fluence $\mathscr{F}$ and the delay τ of the low intensity laser pulse (also referred to as pre-pulse).

The experimental setup is thus modified to host a 10 mm mirror in front of the first mirror in the interaction chamber, as illustrated in figure 4.4a. A peripheral portion of the collimated laser beam is therefore intercepted and sent on the target before the remaining of the beam. The delay τ between the pre-pulse and the main pulse is determined by the distance d_{pp} between the two mirrors, according to the relation:

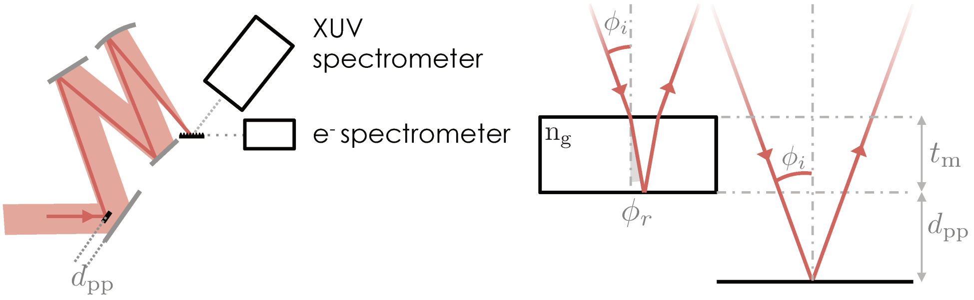

(a) (b)

Figure 4.4: Setup of the experiment on HH generation. In (a), a small mirror is introduced in the laser path to create the pre-plasma. The distance d_{pp} determines the expansion delay, which is calculated with the geometry displayed in (b).

$$\tau = \frac{2d_{\mathrm{pp}}\cos\left(45^\circ\right)}{c}. \tag{4.3}$$

It is rightly arguable that the relation 4.3 cannot result in a zero-delay value because of the mirror thickness. This has been duly considered during the design of the pre-pulse line, as illustrated in figure 4.4b. In particular, the relevant reflection from the small mirror is produced on its rear surface, which has a metallic coating; the front surface, on the contrary, is anti-reflecting. The delay between a light ray that intercepts the small mirror and a ray that propagates freely to the main mirror is hence:

$$\tau = \frac{\mathrm{n_g}}{c} 2 d_{\mathrm{pp}} \cos{(\phi_r)} - \frac{1}{c} 2 (d_{\mathrm{pp}} + t_m) \cos{(\phi_i)}.$$

Referring to figure 4.4b, t_{m} is the mirror thickness, ϕ_i and ϕ_r are respectively the incidence the refraction angles and $\mathrm{n_g}$ it the refraction index of glass (1.5). This delay turns to zero if $d_{\mathrm{pp}} = t_m (\sqrt{\mathrm{n_g^2} - \sin^2{(\phi_i)}} / \cos{(\phi_i)} - 1)$. Inserting $\phi_i = 45°$ gives $d_{\mathrm{pp}} \simeq 0.9 t_m$. In the experiment, the position d_{pp} of the small mirror is accurately controlled by a motorized stage and calibrated to take into account this correction due to the mirror thickness.

The pre-pulse intensity, I_{pp}, can be estimated considering the fraction of energy contained in the small beam and the size of the pre-pulse focal spot produced on target by the $f = 300$ mm parabola. For the same parameters described in chapter 2, the pre-pulse energy is about 10 mJ and the focal spot waist measures ~ 25 μm. This leads to a pre-pulse intensity I_{pp} of $\sim 10^{16}$ W/cm^2, which is still above the ionization threshold of the target. Although the pre-plasma expansion certainly depends on the the transverse profile of I_{pp}, the pre-pulse focal spot is much larger than the main pulse waist. As a consequence, it is safe to assume that the pre-plasma is uniform over the main pulse focal spot, so that L_{pp} only depends on z [121, 134]. The overlapping and centering of the main focal spot with the pre-pulse is verified with the imaging system described in chapter 2. With the same system, the intensity the pre-pulse focal spot is confirmed to be uniform over the same area covered by the focal spot of the main laser beam.

The pre-plasma gradient scale length L_{pp} is inferred by the pre-pulse delay τ and the expansion velocity:

$$L_{\mathrm{pp}} = v_{\mathrm{pp}} \tau. \tag{4.4}$$

Modeling a semi-infinite, isothermal pre-plasma (as in chapter 1), the expansion velocity turns out to be the ion acoustic velocity $c_s(T_e)$: in its turn, the electron temperature T_e depends on the amount of energy deposited in the target, *i.e.* on the fluence $\mathcal{F}$. This model does not take into account either the plasma cooling during the expansion or the energy loss of the solid target all along its ionization. Hydrodynamical simulations can better represent the scenario, achieving useful parametrization of the expansion velocity thanks to a more realistic model of the evolution of the plasma density. In particular, simulations performed with the code ESTHER (EffetS Thermo-mecaniques et Hydrodynamiques Engendres par un Rayonnement, developed at CEA DAM) during the work of A. Leblanc [134] show that the expansion velocity of a solid SiO$_2$ target 30 μm thick, 2 ps after the irradiation by a 25 fs laser pulse, is:

$$v_{\mathrm{pp,[nm/ps]}} \simeq 5.6 \sqrt{\mathcal{F}}_{[\mathrm{J/cm^2}]}. \tag{4.5}$$

Moreover, the plasma density is found to follow an exponential decay as in equation 1.11 only for short scale lengths ($L_{\text{pp}} \leq 100$ nm); in the opposite limit, the plasma profile is approximated by a function $n(z) \propto n_0 \times \exp\left(-z/L_{\text{pp}} + \exp\left(-z/l\right)\right)$, with l a fit parameter, which better describes the density peak in the proximity of the ionized surface. These results were validated with the experimental measurement of the expansion velocity with the Spatial Domain Interferometry technique (SDI) [152].

In short, this technique consists in measuring the intensity of a probe pulse which is being reflected by an expanding plasma. The arrangement is such that only a part of the probe beam interacts with the plasma, undergoing a phase shift which is proportional to the plasma expansion and causes the reflected intensity to oscillate in time. The measurement determines the delays τ when the reflected intensity performs half an oscillation, which correspond to a phase shift increase of π. At the same time, the phase shift is proportional to the position of the critical surface z, expressed as a function of the plasma length scale L_{pp} once the plasma density profile is known. The expansion velocity is then obtained from the expression 4.4. In this case, the result of hydrodynamical simulations contributes to the choice of the plasma density profile $n(z)$, which is the very crucial step of this procedure [134].

Following these considerations, the expansion velocity of the pre-plasma created with the experimental setup in figure 4.4a is obtained by inserting in the equation 4.4 the values of the delay and expansion velocity found with the expressions 4.5 and 4.3. It is important to remark that the pre-pulse fluence $\mathcal{F}$ depends on the incidence angle on target ϕ_i: for 45°, $\mathcal{F} \simeq 420$ J/cm^2, giving $v_{\text{pp}} \simeq 115$ nm/ps. When the small mirror is placed at $d_{\text{pp}} = 250$ μm, the pre-plasma scale length corresponds to $L_{\text{pp}} \simeq 135$ nm, *i.e.* 0.17λ. This value is likely an overestimation of the real scale length, because the experimental pre-pulse is far from being diffraction-limited. For a measured waist of $\sim$ 30 μm , the fluence $\mathcal{F}$ reduces to 260 J/cm^2 giving a scale length L_{pp} of 0.13λ. This value was later compared to the outcome of the SDI technique, which was applied to the same setup during another experimental campaign. The experimental $L_{\text{pp}} \simeq 0.12\lambda$ is in good agreement with the rough theoretical estimation, resulting in an error below 10%. This one is likely to be caused both by the choice of the plasma density profile used to evaluate the phase-shift in the SDI technique and by the necessary simplifications of the hydrodynamical simulations. For the same reasons, the expansion velocity is found to depart from its expected dependence on the incidence angle ($\sqrt{\cos\left(\phi_i\right)}$), especially above 50° [134]. In the following, the results of the SDI measurements are employed to calibrate the pre-plasma scale length for the incidence angles 35° and 45°. The value for 30° is obtained by rescaling the incidence angle, since the SDI measurement was not carried out in this case.

4.4 Experimental results

The experiment aimed at investigating the HH generation from a grating irradiated at the resonant angle for SP excitation, and to compare the results with the emission from a flat target. The grating is the same thin G30 used for the electron acceleration[3], whereas the flat target is a a thick slab of silica SiO_2. Both targets are mounted on the same holder in the interaction chamber, with the same arrangement discussed in chapter 2. The harmonic emission was explored at three incidence angles: 30° (expected resonant angle), 35° (to look for possible resonance shifts), 45° (certainly out of resonance and providing a higher yield with the flat target). At every change of the incidence angle, the pre-plasma scale length is optimized by looking for the maximum HH efficiency as a function the expansion delay τ. Then, the harmonic spectrum is recorded at different observation angles ϕ (the specular and, measuring from the target normal, 78.5°, 82° and 87.5°), together with the energetic spectrum of the electrons emitted along the target surface.

HH diagnostic

The tilted Lanex screen around the laser-irradiated target is removed to make room for the XUV spectrometer. A slit placed at the entrance of the instrument selects a portion of the reflected beam, which is then dispersed by a focusing grating along y. The resolved harmonic spectrum is focused on a MCP coupled with a phosphor screen and imaged by an external Mako G-030 CMOS camera. A simple sketch of the spectrometer is given in figure 4.5. The angular acceptance in the incidence plane $(x - z)$ is set by the width of the grating, 3 cm, and its distance from target, ~ 28.5 cm: $\Delta\phi \simeq 6°$. The distance between the grating and the MCP determines the spectral range of the device, that is $[16, 80]$ nm, corresponding to the harmonic orders $[50, 10]$ of the laser frequency.

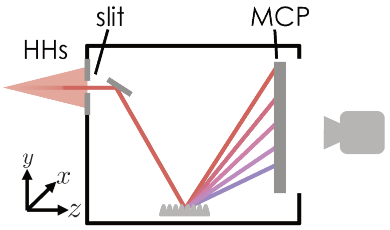

Figure 4.5: Side view of the XUV spectrometer.

For each incidence angle, the spectrometer is aligned along preferred directions, including the specular and a 10° scan around the tangent. At the same time, surface electron acceleration is still used to monitor SP excitation. Hence, the electron spectrometer described in section 3.3 is kept along the tangent direction, at a closer distance (6 cm) from target.

---

[3] The gratings used in this experiments belong to an older batch with groove depth equal to 250 nm.

4.4.1 Pre-plasma optimization

Figure 4.6 compares two HH spectra obtained with a flat target with and without the pre-plasma optimization. They are both recorded in the specular direction and displayed with the same color scale. In presence of the pre-plasma, not only the harmonic intensity increases, but also the spectrum attains higher orders of the laser frequency, as clearly shown by the lineouts that are obtained by integrating the signal over the whole angular range ($\Delta\phi = 1.6°$). These observations agrees with the prediction of the ROM mechanism described in the previous sections.

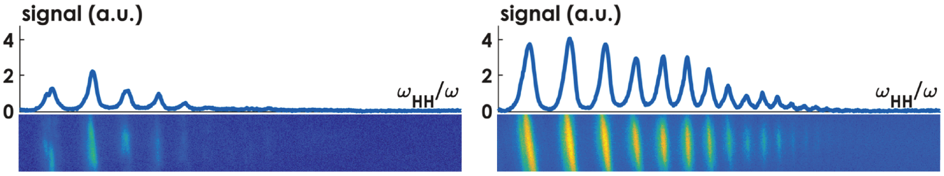

(a) no pre-plasma (b) best pre-plasma

Figure 4.6: HH emission in the specular direction from a flat target irradiated at 35°.

A full scan of the pre-plasma extent further underlines this trend, allowing to choose the best conditions to optimize the ROM process. The result is presented in figure 4.7, where the maximum order detected in the harmonic spectrum is represented as a function of the pre-plasma scale length, for both the flat and the grating target, at all incidence angles. For each measurement, the maximum order is defined as the last order in the harmonic spectra for which the signal is still above 5 times the background level; the signal is obtained by integrating over a window of ±2° around the observation angle of the spectrometer. Each point represents the average of all laser shots, with the standard error as error bars. The pre-plasma scale length is inferred from the expression 4.4, combining the experimental delay τ and the expansion velocity.

The first column reports the emission from the flat target detected in the specular direction. When the pre-plasma is optimized, the HH spectra show up to 10 orders more than without pre-plasma, depending on the incidence angle: the maximum enhancement is obtained for $\phi_i = 45°$ (third line), in agreement with the parametric study shown in [22] where the HH efficiency increases for larger incidence angles (up to 55°). It also appears that the best scale length decreases with larger incidence angles. This can be understood with the following, simple considerations. The ROM mechanisms is efficient when the electrons oscillations in the driver field are balanced by the space-charge electric field that recalls them towards the target. In the case of vacuum heating, the driver consists of the normal component of the

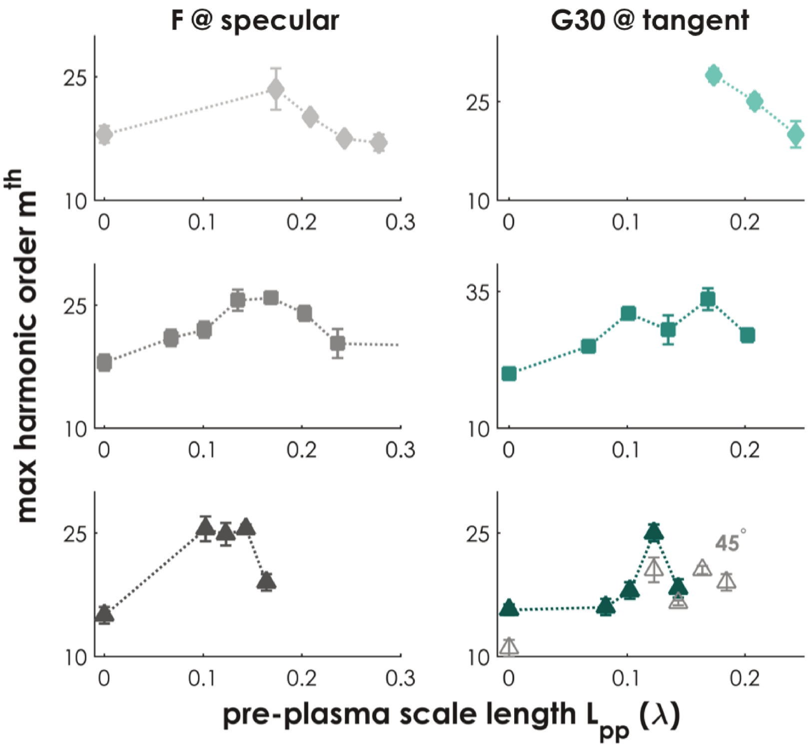

Figure 4.7: The maximum harmonic order as a function of the pre-plasma scale length, for both the flat target (first column, gray shades) and the grating (right column, in green). Each line refers to a different incidence angle; from top: 30°, 35° and 45°, respectively. The signal is recorded in the specular direction in the case of the flat target, and at 87° for the grating; for 45° of incidence, also the specular is shown with empty markers. The HH emission is optimized for a scale length around 0.15λ.

laser electric field, which increases with larger incidence angles; it is hence expected that a shorter gradient is required to set up a stronger electric field than counterbalance the oscillations.

The results from the grating target are displayed in the second column. For each incidence angle, the curves with filled markers represent the HH emission observed at 87°, where the signal is expected to be more intense than in the specular direction, as already noticed in [14]. As further proof, the graph for 45° of incidence contains also the HH signal in the specular direction (gray curve with empty markers): the specular emission is weaker than at tangent but also with respect to the flat target.

4.4.2 HH and electron detection

The configurations with the highest harmonic yield are compared in figure 4.8, which shows the lineout of one harmonic spectrum from both a flat and a grating target with the optimal pre-plasma. For the flat target, the incidence angle is 45° and harmonics are observed in the specular direction. This configuration produces the broadest spectra amongst all the investigated ones. Visibly, the intensity decreases until it reaches the noise level at $\mathrm{m}^{\mathrm{th}}_{\mathrm{max}} \sim 25$. On the contrary, the grating irradiated at 35°, which is close to the expected SP resonance, exhibits a distinct emission close to the surface (82°), extending up to the 37th harmonic order. The intensity oscillations along the whole spectrum are caused by the angular dispersion of the HHs performed by the grating, combined with the small angular range chosen to analyze the experimental images (±0.5°) [146]. Nevertheless, some orders (*e.g.* 12th to 15th) are as intense as with the flat target [15]; the comparison of the two spectra hence indicates that for a selection of harmonic orders the grating might be as efficient as a flat target; furthermore, only the grating produces a considerable signal for higher harmonic orders, in agreement with the results anticipated in figure 4.3.

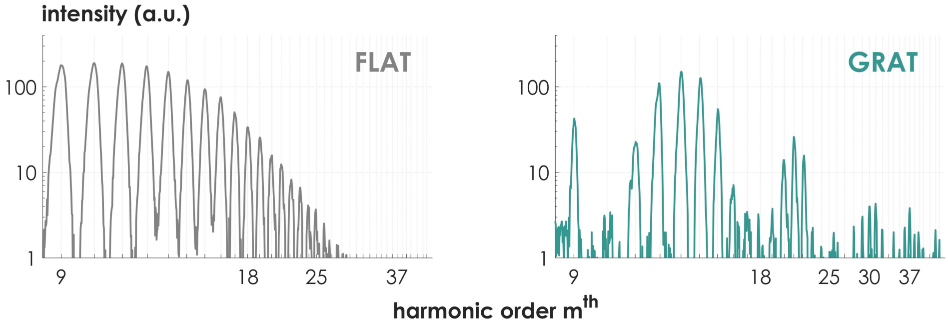

Figure 4.8: Comparison of HH generation from a flat and a grating target. The intensity is obtained by integrating the collected signal over a ±0.5° angular range. The XUV spectrometer is centered in the specular direction for the flat target (*i.e.* 45°) and at 82° for the grating, which is irradiated at 35°.

To relate the harmonic enhancement to the excitation of a surface wave, the maximum harmonic order was observed in different directions as a function of the incidence angle. The result is shown in figure 4.9. In the specular direction, the grating behaves like a flat target, with the maximum harmonic order slightly increasing at 45° of incidence. On the other hand, the emission in the tangent direction for incidence angles close to the SP resonance exhibits frequencies almost 1.5 times higher than far from resonance (*i.e.* at 45°). It should be noted that according to the grating equation 4.2, higher harmonic orders are diffracted farther from the tangent direction,

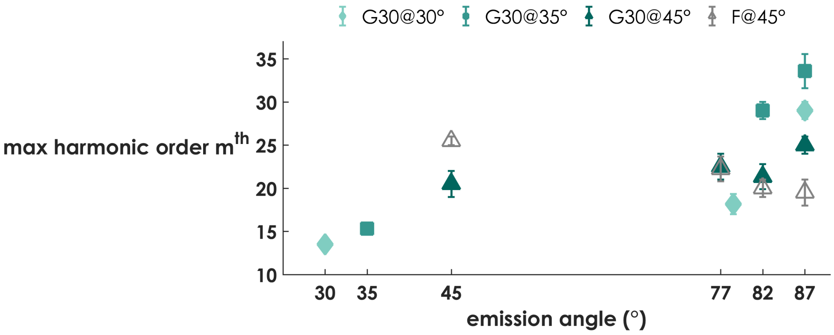

Figure 4.9: The maximum harmonic order at different emission angles, as a function of the incidence angle. For the grating, the pre-plasma has been optimized by measuring the HH emission at 87°. The signal from the flat target irradiated at 45° is indicated with empty gray markers.

regardless of the incidence angle: therefore, the harmonic observation cannot be ascribed to the simple grating dispersive effect. Already in the work by M. Cerchez et al. [146], richer HH spectra in the tangent direction were partly explained in terms of the local change of the incidence angle caused by both the ponderomotive force and the curved wavefronts of the laser pulse. In any case, since the processes underlying the HH generation are based on the motion of the electrons at the target surface, the simple geometrical description of the harmonic diffraction cannot not account for all the experimental observations. Accordingly, the harmonic orders detected in the tangent direction with the flat target are not expected with formula 4.2, yet they are also visible in PIC simulations (compare [14] and the following section).

Further evidence comes from the energetic spectra of the electrons accelerated in the tangent direction with the grating. In this case, these measurements also give some interesting information about the role of the pre-plasma. The maximum energies inferred by the electronic spectra are shown in figure 4.10 for different incidence angles and pre-plasma scale lengths. The maximum energy is taken in correspondence of a scintillating signal equal to twice the noise level.

Despite performing the usual pre-plasma scan at 45° of incidence, only two configurations produced a detectable signal. Without pre-plasma, the maximum energy is approximately one half of what is recorded at resonance. This agrees with the energy values reported as a function of the incidence angle in chapter 3 (figure 3.10). Still at 45° and at the best L_{pp}, the maximum energy does not significantly change, suggesting that the grating is not washed out for $L_{\mathrm{pp}} \sim 80$ nm (as it is expected that, in this case, slower electrons would be observed in the tangent direction). A different scenario results

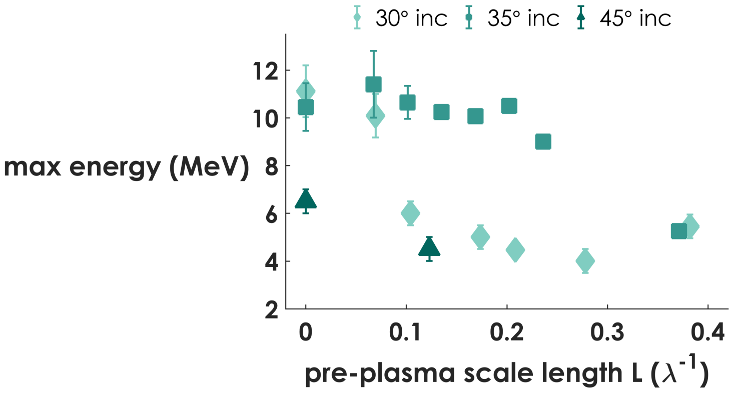

Figure 4.10: Energy of the electrons emitted in the tangent direction by the grating target, as a function of the pre-plasma scale length and the incidence angle. The values correspond to the energy where the signal is twice the noise level. The error bars are given either by the standard error in case of many shots, or by the spectrometer resolution (*i.e.* 0.2 MeV).

by irradiating the grating at 30°, which is assumed to be the SP resonant angle. Energetic electrons are emitted only without pre-plasma: as soon as L_{pp} increases, energies are as low as the case out of resonance, questioning the SP excitation and, more importantly, suggesting that a shift in the SP resonance condition might have occurred. Indeed, the electron acceleration at 35° of incidence points in this direction: the maximum energy measured at the best pre-plasma attains $\sim$ 11 MeV, close to the result obtained at resonance and with no pre-pulse. Besides, the pre-plasma is supposed to alter the SP resonance condition 1.20: the resonant angle of a grating with period 1.6 μm is 30° provided that $n_e \gg n_c$, which is true for a common solid target ($n_e/n_c \sim 10^2$). However, a ratio $n_e/n_c \sim 10$ is enough to shift the resonant angle to 34°. For a plasma density decreasing along the target normal according to $n_e = n_0 \exp{(-z/L_{\mathrm{pp}})}$, such ratio might occurr far within the grating depth and the Rayleigh length of the laser beam (for a proper choice n_0 in the range $[20, 400]n_c$ as discussed in [134]).

4.5 Numerical simulations

In light of experimental results, the harmonic emission with a pre-plasma was analyzed with 2D PIC simulations run with PICCANTE.

To this aim, an exponential density ramp along the target normal was introduced to mimic the pre-plasma expanded after the temporal delay τ. The scale length of the ramp, similarly to the definition of L_{pp} in 1.1.2, corresponds to the experimental values found for the different incidence

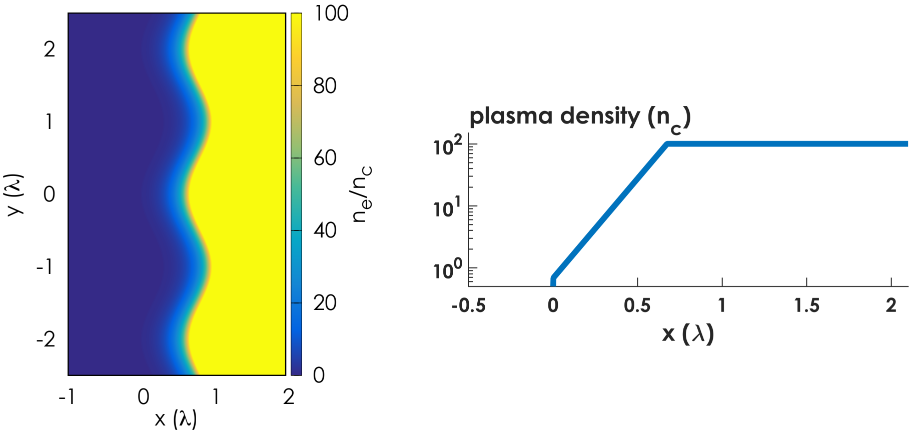

Figure 4.11: Density profile of the G30 at the beginning of the simulation. (a): 2D profile; (b): lineout in logarithmic scale at $y = 0$.

angles: 0.14 for 30°, 0.135 for 35°, 0.125 for 45°. As a convention, the density ramp is cut at $x = 0$ in correspondence of the density value $n_0/\mathrm{e}^5 = 0.0067n_0$. The target thickness is consequently increased by $5L_{\mathrm{pp}}$ to keep the thickness of the overdense region equal to 2λ. The grating (G30) has a period of 2λ and a groove depth of 0.31λ. Figure 4.11 shows an example of the density profile implemented in the simulations (with $\phi_i = 35°$).

Only the most significant configurations were tested: the flat target irradiated at $\phi_i = 45°$ and the grating irradiated at $\phi_i = 30°$ and 35°. For the analysis of the harmonic emission both the target density and the grid resolution were increased in order to resolve the EM field with at least 10 points/oscillation up to the 34^{th} harmonic order for the G30 irradiated at 35°. To reduce the computational load, the simulation box and duration were shortened to, respectively, $60\lambda \times 60\lambda$ and $35\lambda/c$. With these parameters, HH generation is expected to have fully occurred (the laser pulse has been entirely reflected at $35\lambda/c$). On the contrary, the electron acceleration along the surface emerges for longer times, so the simulation parameters for analyzing the electron emission were kept as in table 3.4 on page 69.

The full list of parameters for the HH simulations is reported in table 4.1. It should be noted that, in contrast with the simulations reported in [14], also the laser normalized amplitude a_0 was kept to the experimental value, *i.e.* $\simeq 5$. A set of pre-plasma-free simulations was also carried out for comparison.

The HH spectrum was obtained by calculating the 2D spatial Fourier transform of the magnetic field B_z in the vacuum region in front of the target at the end of the simulation ($t = 35\lambda/c$). The result is displayed in the (k_x, k_y) plane, where the emission angle ϕ is defined as $\phi = \arctan(k_y/k_x)$.

Parameter	values
box size (x, y)	$60\lambda \times 60\lambda$
spatial resolution Δx (same along y)	334 ppλ (200 ppλ for G30 at 30°)
boundaries	periodic
target density n_0	$100 n_c$
particles per cell	100 electrons, 36 ions ($Z/A = 1/2$)
target shape	flat and sinusoidal grating with exponential density ramp
ramp scale length L_{pp}	from 0.125 to 0.14λ
target thickness	$2\lambda + 5L_{\text{pp}}$

Table 4.1: Parameters of the PIC simulations for the HH analysis.

The target surface is identified by $\phi = 90°$, hence by the axis $k_x = 0$. The m^{th} harmonic order appears at the angle ϕ_m and a distance $k_m = (k_x + k_y)_m^{1/2}$ from the origin that corresponds to its wavevector. The HH spectrum along a generic emission angle Φ is then obtained by integrating the Fourier transform of each harmonic order:

$$I_m = \int_{\Phi-\Delta\Phi/2}^{\Phi+\Delta\Phi/2} \int_{k_m-1/2}^{k_m+1/2} |\hat{B}_z(k_x, k_y)|^2 k \mathrm{d}k \mathrm{d}\phi. \tag{4.6}$$

4.5.1 Harmonic emission

Figure 4.12 shows the intensity of the HH spectrum in the entire half-plane in front of the target, comparing the cases with and without pre-plasma for any tested incidence angle. It is worth specifying that although the significant part of the simulation box is located at $x < 0$, *i.e.* $k_x < 0$, the figures are displayed with positive k_x for better readability.

The first line refers to the pre-plasma-free configurations, for increasing incidence angles: from left, 30°, 35° and 45°. The flat target is easily recognizable in the third panel, since all the harmonics are emitted in the specular direction. The brightest point on the $k = 1$ circumference corresponds to the reflection of the laser pulse at $\omega = \omega_L$. The other panels show the harmonic orders diffracted by grating along some of the angles predicted by 4.2. The signal in the tangent direction is particularly intense for $\phi_i = 35°$, in agreement with the results reported at higher laser intensity in [14].

The harmonic enhancement caused by the optimized pre-plasma stands out from the second line of the figure. With the flat target, despite the intensity of laser reflection is reduced by half, harmonic orders up to the 30^{th} are clearly visible. Interestingly, the harmonics beyond $m \simeq 25$ look like a hollowed spot, which is generally not observed in the experiment once

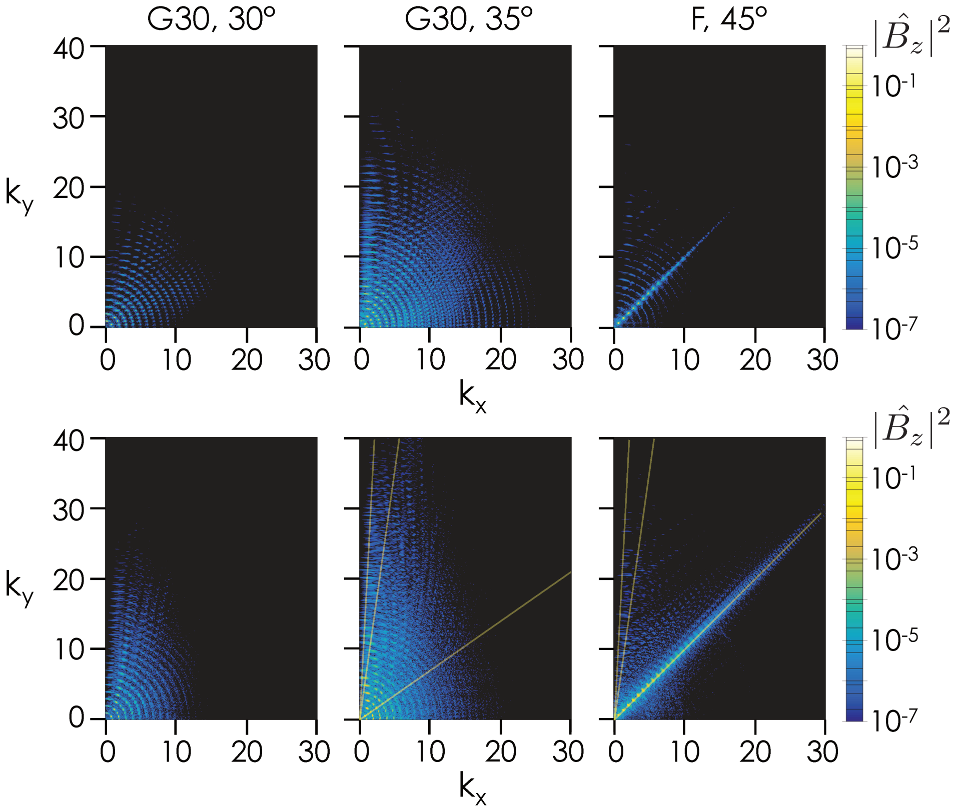

Figure 4.12: Intensity of the HH spectra in the (k_x, k_y) space, for different incidence angles, without (top) and with (bottom) pre-plasma. The first two columns refer to the grating, the third one to the flat target. Yellow lines represent favored directions: the specular and, turning counterclockwise, 82° and 87°.

the laser beam is properly focused on target. As a matter of fact, random fluctuations of the laser wavefront may produce a focal spot where the energy is distributed in more than one point. This would create stray harmonics sources, and the interference of the emitted beams would result in dashed intensity structures. Parallel filaments have also been observed in relation to a poor laser contrast and the uncontrolled ionization of the target surface.

The grating emission exhibits remarkable properties, too. The spectra extend to higher orders for both incidence angles, reaching $\omega_m = 40\omega_L$ for $\phi_i = 35°$, close to the tangent direction $(82° < \phi < 87°)$. Remarkably, the same angular range reveals harmonics around $m = 20$ even with the flat target. Despite being more intense, the overall distribution is also more noisy, which is likely to be caused by the laser pulse refracted by the expanding pre-plasma.

A better look at the intensity values of the different spectra is given in

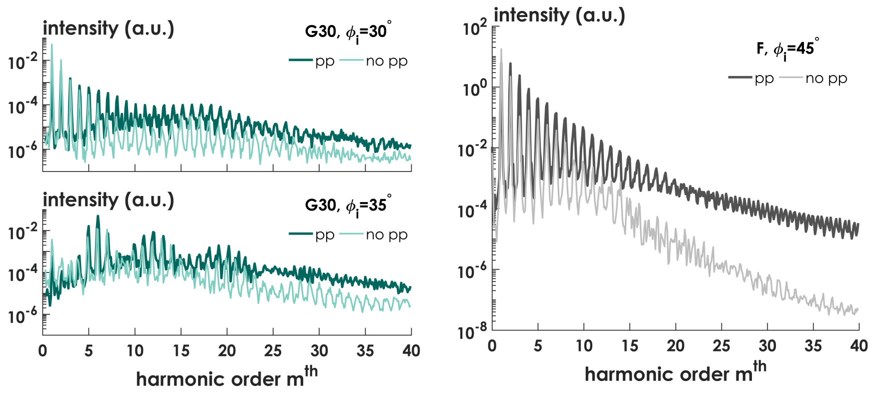

(a) grating, HHs within 84.5° ± 2.5°

(b) flat, HHs within 45° ± 2.5°

Figure 4.13: Intensity profiles of the HH spectra integrated over selected angular ranges.

figure 4.13 where, for each target, the profiles with and without pre-plasma are compared within a selected emission range: $\phi = 84.5° \pm 2.5°$ for the G30, and $45° \pm 2.5°$ for the flat target. As a consequence of the sum of the points $\propto |\hat{B}_z|^2$ across these regions, the intensity of the higher harmonic orders emerges more than in the representation of the k-space. Nevertheless, all the curves allow to appreciate the pre-plasma increasing the HH intensity: at high m, a gain factor of ~ 10 is achieved with the grating, whereas up to 3 orders of magnitude are observed with the flat target. In this case the intensity attained by the highest HHs is comparable with the signal produced by the G30 irradiated at 35°. At the same time, the trend of the light curves, *i.e.* without pre-plasma, reproduces the result of the simulations presented in 4.3 at the beginning of this chapter.

With regard to the grating, the configuration 35° of incidence is the most efficient one, in agreement with the experimental observations. From figure 4.13, the most intense harmonic order for the G30 irradiated at resonance without pre-plasma corresponds to $m = 1$, which can be also interpreted as the surface wave propagating in the tangent direction (remark from figure 4.12 that this order extends to $\phi = 90°$). With the pre-plasma, this order is damped for the benefit of the orders between 10 and 20. The same observations apply to the G30 irradiated at 35°, but the overall signal is enhanced by a factor of ~ 10.

4.5.2 Electron acceleration

The analysis of the electron emission in the tangent direction under the same conditions of pre-plasma investigated in the previous section indicates a correlation with the harmonic emission. Figure 4.14 shows the angular distributions of the electrons emitted with either the grating (left panel) or the flat target (right panel) and different values of pre-plasma. Only electrons above 10 MeV are retained; solid curves represent the configurations with the pre-plasma, dashed lines refer to the same simulations described in chapter 3. The well-known electron emission along the target surface (*i.e.* $\phi < 10°$) is found when the G30, with pre-plasma, is irradiated at 35° of incidence. By integrating the profiles displayed in the figure, the electron number is $\sim 30\%$ less than the yield with the pre-plasma-free G30 irradiated at resonance. The acceleration is visibly inefficient either at 30° of incidence with a pre-plasma (blue curve), or with the unsuitable density gradient (G30 at 35° and with twice the best L_{pp}, light red curve). The poorest result, obtained with the grating irradiated at a non-resonant angle (45°), is displayed for comparison.

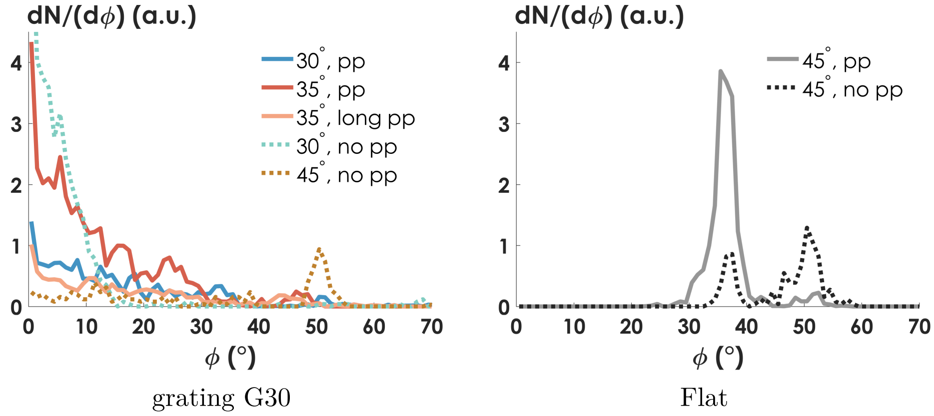

grating G30 Flat

Figure 4.14: Angular distribution of the electron emission for different pre-plasma and incidence conditions.

The flat target, displayed on the right, exhibits a collimated peak close to the specular reflection of the laser field. Such electron bunch is compatible with the vacuum laser acceleration mechanism, which has been observed to be efficient for the same density gradient as for the optimal HH generation [134].

In conclusion, 2D PIC simulations clearly emphasize the role of the pre-plasma in the optimization of the HH emission. A gain of $\sim 10^3$ is achieved on the highest harmonic orders ($m = 40$) from a flat target. In this way, their intensity is comparable with the signal from the G30 irradiated at 35° of incidence, where the gain due to the pre-plasma is limited to a factor of 10. In agreement with the experiment, harmonic orders up to the $35^{\text{th}} - 40^{\text{th}}$ are visible with the G30 irradiated at 35° rather than at the expected angle for SP resonance, 30°. The electron emission in the tangent direction is optimized for the same angle.

4.6 Conclusions

This chapter has presented the first experiment of High-order Harmonic generation from a grating target irradiated at the resonant angle for the excitation of Surface Plasmons.

This interaction scheme gathers various interesting aspects of HH generation in the relativistic regime. First of all, overdense plasmas sustain high intensities of the incident laser pulse, as the underlying generation mechanisms depend on the motion of fast electrons at the vacuum-plasma boundary: the more intense the laser pulse, the larger the frequency upshift on the reflected field. Secondly, the grating diffracting the different harmonic orders at different angles is suitable for those XUV applications requiring a monochromatic source. Finally, the SP excitation relies on the grating geometry to further enhance the EM field at the target surface.

No experimental evidence of the latter effect existed before the realization of this work, whose results, in addition, show remarkable agreement with numerical PIC simulations just recently published [14]. In particular, the enhancement of the harmonic spectrum close to the grating surface was observed close to the SP resonant angle. Not only the intensity of some harmonic orders is comparable to their counterparts in the emission from a flat target, but the whole spectrum extends to higher cutoff frequencies (35ω against 25ω observed with the flat target). The simultaneous electron acceleration along the grating surface gives further evidence in support of the SP excitation. In fact, this one was by no means guaranteed, as the grating surface had been pre-ionized by a low-intensity pre-pulse in order to increase the efficiency of HH generation. The fact that the plasmonic effects are still fairly detectable not only reinforces the feasibility of SP excitation in the high-field regime, but also confirms the capability to carefully control the pre-plasma scale length. This may light new possibilities to master the laser-target interactions by combining micro and nano-structures with fs laser pulses. Moreover, despite further studies are required to validate any favorable correlation between enhanced harmonic emission and electron acceleration, these preliminary results stretch towards challenging applications where a single laser-irradiated target acts as both an electron and an XUV source. Such a scheme could implement, for instance, a compact seed source for an XUV FEL [153]. In the short term, a thorough scan of the grating parameters, as performed in the case the electron acceleration, is the first step to define the best conditions for the harmonic enhancement. Blazed gratings are expected to combine their efficient diffraction properties [15] with the plasmonic effect and to produce higher harmonic intensities. From the point of view of numerical simulations, further developing the role of the pre-plasma (for example by mimicking the accurate hydrodynamical expansion, as done in [134]) could definitely contribute to the optimization of the XUV source in this new regime.

Conclusions

This work contributes to the physical context of the highly-intense laser-solid interaction with the experimental demonstration of a new approach to increase the target energy absorption. All in all, it provides remarkable experimental and numerical evidence of the practicability of Relativistic Plasmonics, with promising follow-ups in the development of laser-driven radiation sources.

At a fundamental level, the results described in the manuscript solidly prove that Surface Plasmons can be excited also for laser intensities beyond 10^{18} W/cm^2, a regime where relativistic nonlinearities take place. This happens in spite of several unfavorable arguments: the lack of relativistic theory for SPs, which could result in a different dispersion relation and impose different phase-matching conditions from the ones obtained with the linear, non-relativistic theory; the fewness of available coupling schemes, which compel to use grating targets in order to overcome the unavoidable fact that different dielectrics would simply turn in a sole conductor when irradiated by relativistic laser pulses; the laser temporal contrast, which must prevent the intensity of the pulse pedestal from destroying the grating structuring before the interaction with the main pulse peak.

To a good extent, all these issues have been solved by the experimental results reported here: the linear theory predicts a resonant angle for SP excitation which happens to fit also in the relativistic regime; the grating coupling works, provided that a material with a high ionization threshold, like plastic, is employed; the ASE pedestal of both 100 TW and 1 PW laser systems has proved not to wash out the grating periodicity when a device like the Double Plasma Mirror has been used to increase the laser contrast to $\sim 10^{-12}$.

The successful excitation of the SPs comes out from the characterization of two significant processes which turn to be enhanced when gratings are irradiated at the resonant angle.

The first one is electron acceleration along the target surface. In contrast with a pack of experimental observations reporting the acceleration of electron jets from solid targets at the most varied emission angles, the detection of electron bunches towards the grating tangent is highly reproducible, robust and straightforward; moreover, accurate numerical simulations and a theoretical model support the experimental data. The most significant features of the electron emission are the high charge (up to 650 pC with properly-chosen blazed gratings), the low-divergence (all emissions are spread below 8° FWHM), and the non-Maxwellian spectra, peaked at ~ 10 MeV, with cutoff energies of about 20 MeV. The electron bunches display these remarkable properties only when the grating is irradiated at the resonant angle for SP excitation. Exploring different incidence angles corresponds to a severe depletion of all these quantities. Flat targets, always irradiated for comparison, never produce such collimated and spatially-stable bunches. Other acceleration mechanisms, reported elsewhere, rely on a partial preionization of the target surface that might hinder the integration of these electron sources in more complex target geometries. All considered, the SP-driven electron acceleration is adequate for the development of ultrashort, bright, laser-synchronized electron sources at moderate energies, with potential for high-repetition rate schemes. Exploratory tests of pump and probe experiments or tapered plasmonic waveguides are already conceivable. The promising results obtained on the PW-class laser facility in South Korea also support the feasibility of this acceleration regime at even higher laser intensities.

Still, the characterization of the electron source requires to address further significant aspects of the acceleration mechanisms. Despite the accurate parametric study performed with numerical simulations, there is the need to properly characterize the SP fields and to get more insight into the electron injection conditions. This could give more information about the early-stages of the acceleration process, and help to explain the multi-energetic spectrum observed in the experiments. Indeed, this latter imposes to post-process the electron beam before proposing any application requiring a monochromatic source.

The second process presented in this manuscript is High-order Harmonic generation, which benefits from the local increase of the electric field at the target surface, caused by the excitation of the surface wave. Gratings are already appealing for HH generation because they provide a compact and handy solution to spatially-separate the different laser frequencies and obtain near-monochromatic sources that could be helpful in spectroscopy and imaging applications. The resonant SP turns out to extend the harmonic spectra collected at the target tangent up to frequencies not attained by the emission from flat targets in the same irradiation conditions (incidence angle, laser intensity and gradient scale length). The intensity of specific harmonic orders is comparable with the emission from the flat targets. Moreover, as efficient HH emission requires the control of the density gradient at the target surface, these results confirm the possibility to alter the grating profile on a nano-metric scale while preserving the necessary features (period and depth) for the efficient excitation of SPs.

This second topic leaves room for plenty of improvement and further developments. In light of the promising results on electron acceleration obtained with blazed targets, there is large interest in testing this profile for the SP-assisted HH emission. Whether this one was still related to a strong electron acceleration, laser-irradiated gratings could be used to implement compact laser-synchronized electron-XUV sources. The numerical investigation is also at its first steps. A better understanding of the grating parameters should be cross-correlated with the numerous aspects that the research community in the field of HH generation is being meticulously exploring.

In conclusion, the results discussed in this thesis bring together the domains of plasmonics and laser-plasma interactions in the relativistic regime. First in their kind, they leave stimulating perspectives to the development of laser-based radiation sources, supported by the exceptional potential of the newly-achieved Relativistic Surface Plasmons.

Appendices

Appendix A

Observation angle and distance from CCD

A characterizing point of the experiments performed in this work was the employment of motorized stages to independently displace different tools inside the interaction chamber. This made it possible to quickly modify the incidence angle of the laser beam by rotating the target and to displace all the electron and proton diagnostics accordingly, without opening the interaction chamber. Except for the Thompson parabola, external CCD cameras recorded the signal produced by both Lanex and phosphor screens (respectively, for electron and harmonics detection). For practicality, CCDs did not follow the rotation of each diagnostic, and they were kept in fixed positions around the chamber. Because of this, the recorded signal depends on both the distance and the angle between the CCD and the detector, as shown in figure A1c. It is necessary to estimate these parameters to allow for a legitimate comparison of the data acquired when diagnostics were set at different positions. This appendix describes the procedure implemented to recover the angle and distance between the CCD camera and the Lanex screen for the electron emission spatial distribution, starting from reference pictures of the experimental configuration taken during the campaign. The same calculation was performed to correct the signal from the Lanex screen of the electron spectrometer.

For a given incidence angle inside the range $10° \div 60°$, the rotating platform which accommodates the electron diagnostics is aligned so that the spectrometer points to the tangent direction of the target, as indicated in figure A1a. The Lanex screen is tilted by 45° to intercept the electron emission from the target tangent to its normal. The scheme and notation adopted for the calculation are shown in figure A2. The Lanex position is characterized by the distance between the center of the screen and the camera, CA, and by the angle the screen forms with any plane perpendicular to the camera axis (respectively ξ and c). While CA has been measured

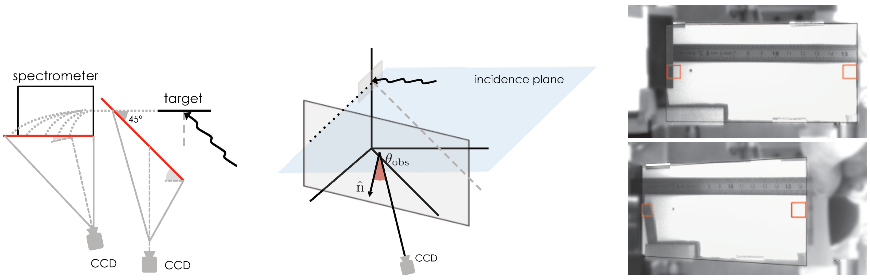

(a) (b) (c)

Figure A1: Arrangement of the Lanex screens in the electron diagnostics: top view (a), 3D view (b) and typical reference images (c). The angle between the screen and axis of the CCD camera produces an effect of perspective which appears from the different heights of the screen edges. By consequence, same areas on the screen result in distorted regions on the image (drawn in red in (c)). Rotating the platform with the Lanex screen visibly increases the perspective effect.

for each position of the rotating platform, ξ is more sensitive to any slight change of the setup and it seemed preferable to retrieve its value from the reference images. Different planes parallel to the camera chip, indicated with tiny letters, are drawn in correspondence of some characteristic points of the Lanex screen: for example a for the plane passing through the Lanex center A, o for the right edge O and so on. The image center is marked with C′. In general, points on the real Lanex screen are marked with capital letters, while their projection on the camera axis c are marked with the prime symbol. The coordinates of a generic P point of the real Lanex are expressed in the image by the pixel values $(\mathrm{x,y})_\mathrm{P}$. As a convention, the angles formed by the distances CC′ and CP are considered positive if P lies on the left of the image center C′. They are designed as α_P to be distinguished from the more generic $\hat{\mathrm{C}}_\mathrm{P}$ which denotes the angle with vertex C formed by CP and CA. For example, in the scheme A2, $\alpha_\mathrm{P} = |\alpha_\mathrm{P}| \cdot \mathrm{sgn}(\mathrm{x}_{\mathrm{C}'} - \mathrm{x}_\mathrm{P})$. Depending on the mutual position of P and A, $\hat{\mathrm{C}}_\mathrm{P}$ is defined as

$$\hat{\mathrm{C}}_\mathrm{P} = ||\alpha_\mathrm{P}| \pm |\alpha_\mathrm{A}|| \tag{A1}$$

where the sign − is considered when P and A lie on the same side from C, and vice-versa.

The screen is mounted to be perpendicular to the floor of the interaction chamber, *i.e.* it does not lean towards the target or the camera, and its vertical edges are straight in the reference image. In this way, measuring the Lanex height (in pixel) at any point on the image allows to infer the distance from the camera to the parallel plane passing across that point, by the simple relation

$$\mathrm{CP}' \cdot \mathrm{h}_\mathrm{P} = \mathrm{CA}' \cdot \mathrm{h}_\mathrm{A}, \tag{A2}$$

where a generic P has been used. At the same time, all pixel-distances measured in the image from P can be converted to mm-distances which lie in the corresponding parallel plane, by using the conversion scale $\mathrm{h_{P,pxl}}/\mathrm{h_{P,mm}}$ $=(\mathrm{pxl/mm})_\mathrm{P}$, that is valid also in the horizontal direction because the CCD pixel ratio is 1.

For each position of the rotating platform, measuring the Lanex height at points A and O, and their distances from the image center C′, are the only steps required to calculate the angle ξ. In principle, any couple of points works as well, but the position of A is well-known on the real Lanex and it can be easily located in the reference images; at the point O, being the farthest from A, the change induced by the perspective on the conversion scale pxl/mm is better resolved, giving more accurate results. All the following calculations have also been tested for different points in the reference images before confirming the choice of A and O.

From the scheme A2, ξ is found from the difference between the angle $\mathrm{C\hat{O}A}$ and $\mathrm{C\hat{O}O'}$. Each of them is defined as:

$$\mathrm{C\hat{O}A} = \arccos \frac{\mathrm{CO}^2 + \mathrm{AO}^2 - \mathrm{CA}^2}{2 \cdot \mathrm{CO} \cdot \mathrm{AO}}, \qquad \mathrm{C\hat{O}O'} = \frac{\pi}{2} - |\alpha_\mathrm{O}|. \tag{A3}$$

The first expression is Carnot's theorem applied to the triangle $\triangle$COA, where CA and AO are measured, and CO is obtained by $(\mathrm{OO'}^2 + \mathrm{CO'}^2)^{1/2}$. OO′ is the distance from the right edge of the Lanex screen to the center of the image C′, converted in mm: $|\mathrm{x_{C'}} - \mathrm{x_O}| \cdot (\mathrm{pxl/mm})_\mathrm{O}$; CO′ comes from the expression A2. With the same parameters, α_O is $(\arctan(\mathrm{OO'/CO'}) \cdot \mathrm{sgn}(\mathrm{x_{C'}} - \mathrm{x_O}))$ and it is negative because the point O lies to the right of C′.

An alternative method to calculate the Lanex angle ξ bypasses the estimation of OO′ with the conversion scale $(\mathrm{pxl/mm})_\mathrm{O}$ and rather uses the angle of view of the CCD camera, so that the angle α_O results from the relation:

$$\frac{\tan(\alpha_\mathrm{O})}{\tan(\alpha_\mathrm{CCD})} = \frac{f \cdot \tan(\alpha_\mathrm{O})}{\text{chip half-width}} = \frac{|\mathrm{x_{C'}} - \mathrm{x_O}|}{(\text{image half-width in pixels})}. \tag{A4}$$

Normally, the chip width and the focal length f of the objective mounted on the camera are well-known. In order to choose the best approach between the estimation of ξ which relies solely on measurements from the reference image and the estimation that uses the CCD angle of view, the distance AO is calculated again with Carnot's theorem applied to the triangle $\triangle$AOC. Both the side CO and angle $\mathrm{A\hat{C}O}$ depend on the estimation of α_O given with the two methods. It turns out that the estimation with the angle of view gives higher deviations from the real AO width (from 5 to 20% against deviations $< 5\%$ with the first method). To explain this result, the focal length f for both the CCDs (Lanex screen and spectrometer) was measured with the same setup as in the experiments, by imaging a calibrated piece of paper. Focal lengths differing from the nominal values of the objectives were found and the AO deviations were reduced below 10%. Still, the first approach is more robust since it relies only on the reference images, which are the closest record of an experimental setup where daily small modifications could severely affect the calculation of ξ .

Once the angle ξ is defined, it is possible to retrieve the observation angle and distance from CCD for each point of the Lanex screen. This allows to correct the collected signal coming from different points on the Lanex and to compare them as if they were acquired from a plane parallel to the camera sensor. Also, repeating this procedure for each position of the rotating platform allows to compare signals acquired from different experimental configurations, *i.e.* with different incidence angles. To give an idea, the distance between the Lanex screen and the CCD camera varies by 50 cm when displacing the platform from the alignment for 10° of incidence to 60°; the tangent direction (point Q in the scheme A2) is seen under an angle which goes from 17° to 48°.

For each point P over the Lanex screen, the observation angle is defined as the angle formed by the distance from the camera to P, CP, and the normal to the Lanex at P. It corresponds to the the azimuthal angle in the coordinate system where the Lanex screen is horizontally cut in half by the incidence plane, as shown in figure A1b. The polar angle is neglected from all the calculations since most of the analysis of the Lanex screen, for both the electron spatial distribution and the energy spectrum, was performed as the same height as the incidence plane.

From the scheme in figure A2, $\theta_{\mathrm{obs,P}} = (\pi/2 - \theta_{\mathrm{P}}) \cdot \operatorname{sgn}(\mathrm{x_A} - \mathrm{x_P})$, where θ_{P} is the angle $\mathrm{C\hat{P}A}$. The sign function comes from the fact that, for practicality, θ_{P} is always defined as the angle in front of CA in the triangle $\triangle$CPA. It means that, with the screen tilt represented in the scheme, θ_{P} increases from P to A without arriving to $\pi/2$; then, when P matches A, the triangle is not defined; when P jumps over A, θ_{P} starts from a value higher than $\pi/2$ and it decreases. The jump in A depends on the minimum distance for which P does not correspond to A, which means $|\mathrm{x_P} - \mathrm{x_A}| = 1$ pixel. From the analysis of the triangles $\triangle$CAP, where P is once on the left and once on the right of A, the jump becomes:

$$\theta_{\mathrm{P,right}} - \theta_{\mathrm{P,left}} = 2\mathrm{C\hat{O}A} - \pi + 2\hat{\mathrm{C}}_{\mathrm{O}} - \hat{\mathrm{C}}_{\mathrm{P,right}} + \hat{\mathrm{C}}_{\mathrm{P,left}}.$$

All these angles are completely defined with the expressions A1 and A3 and eventually depend only on the Lanex screen tilt.

The angle θ_{P} for each point on the Lanex screen is inferred from Carnot's theorem applied to the triangle $\triangle$CPA. Indeed,

$$\theta_{\mathrm{P}} = \arccos \frac{\mathrm{CP}^2 + \mathrm{CA}^2 - \mathrm{AP}^2}{2 \cdot \mathrm{CP} \cdot \mathrm{CA}} \tag{A5}$$

where CA has been measured for each position of the rotating platform, AP is arbitrarily chosen on the reference image (which gives both AP in mm and the coordinate x_P), and CP is obtained on the same triangle using either $C\hat{A}O$ or its supplementary $C\hat{A}Q$ (which are both defined thanks to the triangle $\triangle$COA). In this way the calculation for every point P depends only on how accurately x_P and AP are localised in the reference image.

There may be a point $P_\perp$ on the Lanex screen when the normal direction matches the distance from the camera $CP_\perp$, especially for those reference images where the screen is particularly parallel to the camera chip. As a result of the calculations described so far, the observation angles become negative when are measured beyond $P_\perp$. With the same geometry displayed in the scheme A2, this point is found by considering that $CP_\perp$ would form a right triangle $\triangle CQP_\perp$ and whether the side $QP_\perp$ is shorter than the Lanex width QO. Once the distance $QP_\perp$ is estimated from simple considerations on the triangles $\triangle$CQO and $\triangle COP_\perp$, the coordinate $x_{P_\perp}$ is easily reconstructed from the reference image.

The whole procedure described so far was validated during the experiment for the calibration of the Lanex screen (see B). The observation angle was directly measured during the setup, to be later compared with the result inferred from the reference image. A +2.5°absolute error was found on the measured value of 24.2°. The discrepancy is entirely caused by the estimations of the screen heights at points A and O: it is sufficient to correct h_O by one single pixel to reduce the absolute error to 0.2°.

Summarizing, reference images are used to infer the observation angle and distance from the CCD camera for every point on the Lanex screen. The calculation relies on basic geometrical considerations, once few parameters are measured on the reference image itself (in particular, the screen height at its center, A, and at the right edge O). With this result, it becomes possible to rescale the signal collected at different positions of the electron diagnostics by fixed external CCD cameras, and to achieve a more accurate comparison of the experimental data.

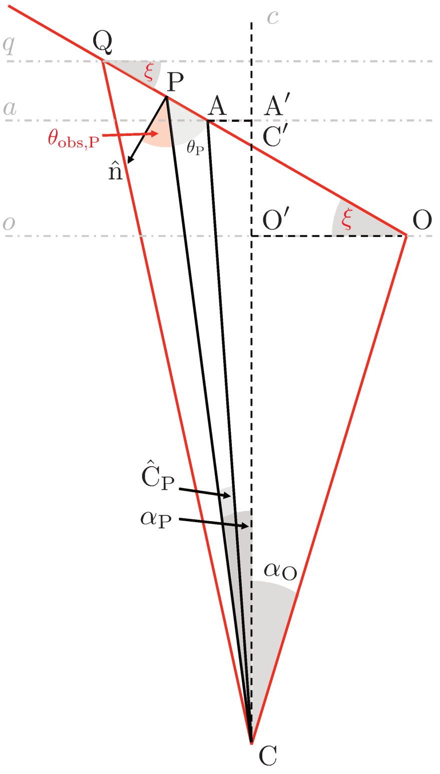

Name	Description
C	CCD Camera position
c	camera axis
C′	image center
A	screen center
O	right edge of the screen
P	generic point on the screen
Q	point aligned to the target tangent
O′	projection of O on the camera axis
A′	projection of A on the camera axis
o	parallel plane passing across O
a	parallel plane passing across A
CA	distance from the camera to the screen center (measured)
ξ	screen tilt
α_{P}	angle between CP and CC′
$\hat{\mathrm{C}}_{\mathrm{P}}$	angle between CP and CA
θ_{P}	angle in front of CA in the triangle △CPA
$\theta_{\mathrm{obs,P}}$	observation angle for P
n̂	normal to the screen

Figure A2: Scheme for the calculation of the tilt and observation angles of the Lanex screen. The actual screen is underlined with a red line, while segments CQ and CO enclose the interesting portion for the analysis. The sketch is out of scale.

Appendix B

Lanex calibration at ELYSE

The Lanex screen placed in front of the laser-irradiated targets collects important information about the spatial distribution of the electron emission. It directly gives a relative estimation of the number of electrons hitting the screen in specific directions, regardless of their energies. Calibrating the Lanex screen and the optical system allows to translate this information into amount of charge.

The calibration campaign was performed at ELYSE, a laser-triggered electron accelerator, delivering electron bunches between 200 and 2000 pC at 8 MeV of energy[4].

The electron bunch hits the Aluminum-covered Lanex screen and the emitted light is imaged with the same optical system employed in the laser-plasma experiments. The basic setup and important geometrical parameters are illustrated in figure B1. Because of the limited space available to implement the setup, it was not possible to also mount the glass viewport of the vacuum chamber in front of the CCD during the calibration campaigns. Nevertheless, its transmission factor (90%) was measured at the same wavelength of the Lanex emission, to be accounted for after the image acquisition, together with the CCD gain, the observation angle and distances. Moreover, the signal was checked to be independent from the CCD temporal exposure for times between 10 and 150 ms.

After subtraction of the dark current and residual noise, the signal recorded by the CCD is well fitted with a Gaussian distribution, resulting in $\sigma = 2.6$ mm (RMS). In this way, the charge density in correspondence of the peak of the distribution corresponds to 38 pC/mm^2 for the maximum charge delivered by the accelerator, and it is below the saturation limit found for similar Lanex screens in other calibration campaigns [118, 119].

---

[4] A former calibration had been performed at PHIL, a photo-injector with charges ranging from 15 to 60 pC, at 5 MeV of energy. In this case the Lanex was protected by 3 mm of Aluminum. For both the correspondance with the setup discussed in this manuscript and the order of magnitude of the charge densities detected in the latest experiments, only the calibration at ELYSE is presented here.

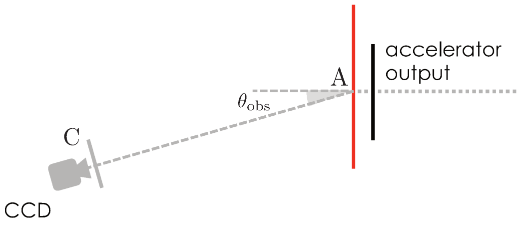

	ELYSE
CA (cm)	85.5
θ_{obs} (°)	24.2 24.3

Figure B1: Setup of the Lanex calibration campaigns. The screen (in red) is protected by 200 μm of Aluminum. In front of the camera there is the 546 band-pass filter and a 1.6 optical density. The distance from the CCD to the electron-irradiated point of the screen, CA, as well as the corresponding observation angle, are noted in the table. The values in the second line of the observation angles are obtained from the analysis of the reference images as described in section A.

The signal is then integrated over the whole size of the spot (considering a diameter of 8σ), rescaled by the proper geometrical factors, and the average signal density is represented as a function of charge. This one is measured before the accelerator output by a Faraday Cup, with fluctuations of about 10 pC for each value of charge. The uncertainty on the Lanex signal counts is calculated by standard deviation on the image sets. The result of the calibration is presented in figure B2: a power function Ax^B fits the experimental points with coefficients $A = 8.95 \times 10^5$ and $B = 0.57$.

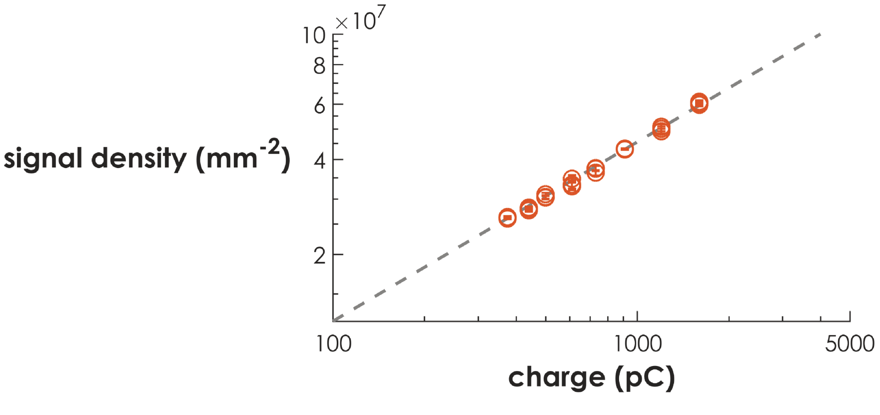

Figure B2: The result of the Lanex calibration campaigns, fitted with the power function $8.95 \times 10^5 (Q)^{0.57}$ and plotted in logarithmic scale.

Appendix C

Analysis of the electron emission

The scintillating screen is extremely resourceful when employed in moderate repetition rate experiments as the ones described in this work. A wide image of the electron emission is collected at every laser shot, allowing to immediately adjust both the target and diagnostics alignment, and to get a prompt feeling of the results. However, the extrapolation of more quantitative information requires a deeper image analysis. This chapter explains how the raw images of the Lanex screen were treated in order to infer some properties of the electron emission, notably the size of the electron bunch and its total signal (defined as the sum of counts of the pixels inside the bunch area).

For a given set of images acquired in the same conditions (*i.e.* incidence angle, Lanex position), the analysis can be split in few steps:

- estimation of the observation angle and CCD distance from the Lanex reference image, as described in appendix A.
- conversion of the (x, y) coordinates on the image into the emission angles (ϕ, θ);
- signal rescaling, to take into account the CCD gain and optical densities: each image is rescaled to a gain of 600 and to OD $= 0$;
- reconstruction of the angular spread of the electron bunch, by means of a set of orthogonal lineouts that are properly rescaled to consider the observation angle, the CCD distance and the solid angle subtended at the target: the reference distance for the CCD is 77 cm, corresponding to the position of the rotating platform when the incidence angle is 30°, and the reference distance from the target is 8 cm, which is the Lanex distance from the target tangent;
- estimation of the signal contained within the bunch, by integrating the previous lineouts;

- estimation of the charge amount, following the Lanex calibration described in the appendix B.

In parallel, the energetic distribution is inferred by the images of the electron spectrometer.

.1 Emission angles

The geometrical quantities needed to transform the image coordinates (x, y) into the emission angles (ϕ, θ) are given in figure C1. The scheme on the left shows the rear surface of the Lanex screen as seen by the CCD: the ϕ axis lies in the incidence plane (*i.e.* $\theta = 0$), and it is intercepted by the θ axis on the hole aligned with the target tangent. The hole is indicated with Q, as in the reference image of the Lanex configuration used to estimate the observation angle (figure A2 in the appendix A). The scheme on the right represents the irradiated side of the Lanex screen, with the electron source S and the azimuthal and polar angle ϕ and θ. Because the distance SP_x between the screen and the target varies along ϕ, points at the same θ happen to be connected by parabolic lines, as shown on the left picture.

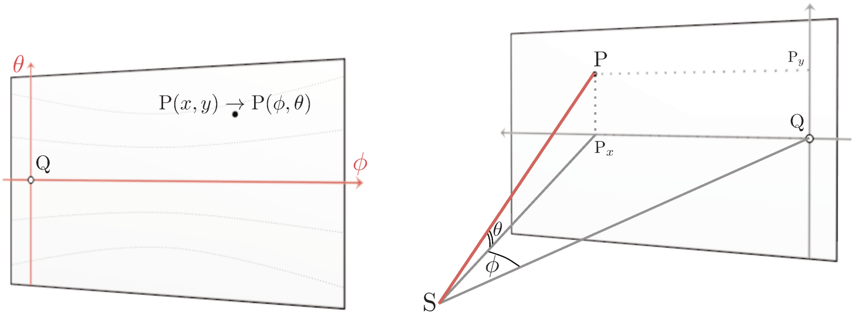

(a) Back view (b) Front view

Figure C1: Scheme of the Lanex visualization. The emission angles ϕ and θ are measured with respect to the tangent direction (line SQ) and to the incidence plane. The distance from the electron source S to a generic point P (underlined in red) is calculated to correct the signal measured in P.

The coordinates (x, y) are expressed as number of pixels, starting from the top-left corner of the image. Therefore, the position of P with respect to Q is given by $QP_x = (x_P - x_Q)$ and $QP_y = (y_P - y_Q)$. Because of the perspective induced by the screen tilt, the reference image is used to convert the horizontal distances to millimeters, while the vertical ones can be transformed knowing the conversion scale of the Lanex height, $h_{P,mm}/h_{P,pxl} = (mm/pxl)_P$.

The expression of θ immediately follows:

$$\theta = \arctan\left(\frac{-\mathrm{QP}_y \cdot (70/\mathrm{h_P})}{\mathrm{SP}_{x,[\mathrm{mm}]}}\right), \tag{C1}$$

where 70 is the Lanex height. The distance SP_x is estimated with Carnot's theorem applied to the triangle $\triangle\mathrm{SQP}_x$ in the incidence plane:

$$\mathrm{SP}_x = \sqrt{\mathrm{SQ}^2 + \mathrm{QP}_x^2 - 2 \cdot \mathrm{SQ} \cdot \mathrm{QP}_x \cdot \cos(\mathrm{S\hat{Q}P}_x)}.$$

The distance SQ is fixed to 80 mm in the setup, so as the angle $\mathrm{S\hat{Q}P}_x$ that is the screen tilt (45°); QP_x is inferred by the reference image.

The estimation of ϕ stands on the same basis:

$$\phi = \arccos\left(\frac{\mathrm{SQ}^2 + \mathrm{SP}_x^2 - \mathrm{QP}_x^2}{2 \cdot \mathrm{SQ} \cdot \mathrm{SP}_x}\right) \cdot \mathrm{sgn}(\mathrm{QP}_x). \tag{C2}$$

The sign function takes into account that the origin of ϕ axis corresponds to the hole Q, so ϕ becomes negative for points beyond the tangent direction. The expression C2 can also be extended to the configurations where the platform is not aligned with the target tangent. Knowing that the angle of Lanex hole Q corresponds to the platform rotation ϕ_0, the position of the point $\tilde{\mathrm{P}}$ where $\phi = 0$ can be estimated by recovering the distance $\mathrm{Q\tilde{P}}_x$ from the triangle $\triangle\mathrm{S\tilde{P}}_x\mathrm{Q}$.

.2 Bunch reconstruction for the grating targets

All gratings share a prominent electron emission in the tangent direction, which is highly intense and collimated at the angle expected for resonant SP excitation, but tends to spread and weaken for non-resonant incidence angles. In this work, both the size and the charge of the electron bunch are obtained after treating the raw images of the signal collected by the Lanex screen. A direct estimation of these quantities on the images is not very accurate, because many geometrical parameters involved in the measurement alter the signal by a significant amount. This section presents the procedure carried out on the experimental data to reconstruct the electron bunch properties. The various steps are explained on the Lanex image reported in figure C2, which refers to the electron emission from a thin G30 irradiated at resonance.

A first insight about the angular divergence of the electron bunch is obtained by tracing a lineout along θ; the lineout is centered on the most intense part of the signal, which might not correspond to $\phi = 0$. For each pixel P, the signal s is rescaled to take into account the geometrical parameters

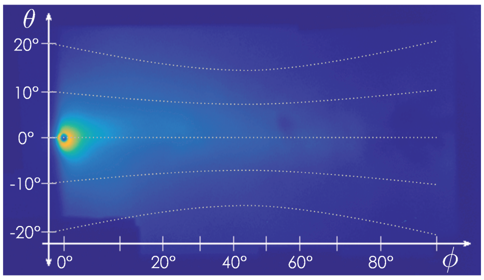

Figure C2: Electron emission from a G30 irradiated at resonance. The angular axis are obtained with equations C1 and C2. Dotted parabolic lines underline the points at the same θ. The color range is $[0, 2.4 \times 10^6]$.

imposed by the imaging system and by the Lanex tilt, according to the transformation:

$$s \quad \rightarrow \quad s \cdot \left(\frac{\sqrt{\mathrm{QP}_y^2 + \mathrm{SP}_x^2}}{80} \right)^2 \cdot \left(\frac{\sqrt{\mathrm{QP}_y^2 + \mathrm{CP}_x^2}}{769} \right)^2 \cdot \frac{1}{\cos\left(\theta_{\mathrm{obs,P}}\right)}. \tag{C3}$$

In this expression, the first term accounts for the distance of P from the target; the second one represents the distance from the CCD, with CP estimated as in A; the last one corrects the CCD observation angle. For a lineout in the tangent direction (ϕ_P =0) and when the incidence angle is 30° ($\mathrm{CP}_x = 77$ cm), the first two terms are $\simeq 1$. The rescaled lineout is then fitted with a Lorentzian distribution:

$$\mathcal{L}(y) = \frac{A_\theta \cdot (B_\theta/2)^2}{(y - C_\theta)^2 + (B_\theta/2)^2} + D_\theta \tag{C4}$$

where A_θ is the peak value, B_θ is the FWHM, C_θ and D_θ are the center the constant term of the distribution. The variable is designated as y because the lineout is along θ, but also because it must be expressed in pixels. The reason is that for more and more spread distributions (as those of the emission far from resonance), the FWHM expressed in degrees will assume non-physical values (*i.e.* $> 90°$): this is prevented by estimating B_θ in pixels and converting it to degrees immediately afterwards. The final θ-lineout from the image C2 is shown in figure C3a: the FWHM is equal to $\sim (5.9 \pm 0.1)°$. Since the lineout crosses the hole on the Lanex, only the points outside are fitted. The peak value A_θ is nevertheless verified by analyzing other images where the rotating platform was aligned at $\phi_0 = 2°$, so that the electron bunch did not intercept the hole.

The bunch width in the incidence plane is obtained with the same procedure: a horizontal lineout is traced along ϕ at the height C_θ returned by the θ-lineout and rescaled according to:

$$s \quad \rightarrow \quad s \cdot \left(\frac{\mathrm{SP}_x}{80} \right)^2 \cdot \left(\frac{\mathrm{CP}_x}{769} \right)^2 \cdot \frac{1}{\cos\left(\theta_{\mathrm{obs,P}}\right)}, \tag{C5}$$

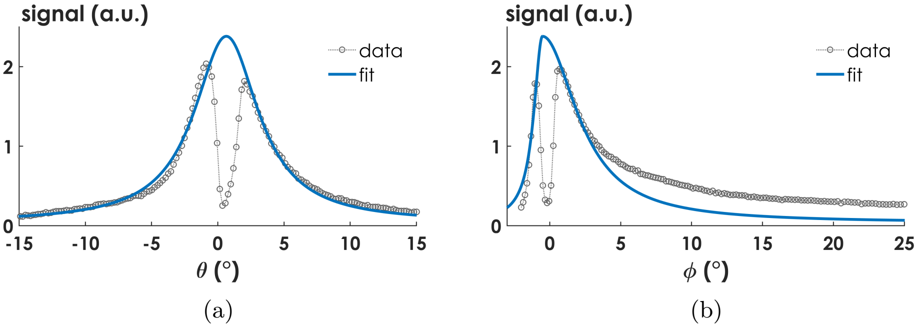

(a) (b)

Figure C3: Orthogonal lineouts of the electron bunch in figure C2. In (b), limiting the ϕ range to 25° eases the peak visualization.

where this time P denotes the pixels along ϕ. The result is then fitted with two Lorentz distributions to take into account the asymmetry of the emission:

$$\mathcal{L}_{\mathrm{l/r}}(x) = \frac{A_\phi \cdot (B_{\phi,\mathrm{l/r}}/2)^2}{(x - C_\phi)^2 + (B_{\phi,\mathrm{l/r}}/2)^2} + D_\phi$$

where (l/r) stand for (left/right) and indicate the FWHM of the distribution on each side of the peak position, C_ϕ (which might not correspond to ϕ_θ where the θ-lineout was traced). Again, the variable x is expressed in pixels. If the peak is believed to fall inside the hole, it is assumed that $A_\phi = A_\theta$. Likewise, $D_\phi = D_\theta$. The ϕ-lineout is illustrated in figure C3b, resulting in $\mathrm{FWHM_l} = 1.5°$ and $\mathrm{FWHM_r} = 6°$. Apparently, the Lorentzian distribution manages to fit the experimental points up to a certain angle ϕ, after which the curve rapidly drops despite the emission in the incidence plane being still measurable, as in figure C2. However, both the FWHMs along the two axis, *i.e.* $B_{\phi,\mathrm{l}} + B_{\phi,\mathrm{r}}$ and B_θ, are believed to provide a fair indication of angular spread of the electron emission.

The next step is to estimate the amount of signal contained in the electron bunch, with the sum of the integrals of the θ-lineouts calculated along ϕ. The ensemble of these lineouts reconstructs the complete bunch by means of the Lorentzian parameters given in equation C4. In particular, the peaks A_θ are set to correspond to the signal of the experimental points measured in the ϕ-lineout (figure C3b). The center and the constant term of the profiles are fixed by the fit of main θ-lineout, as in figure C3a. The trickiest parameters are the FWHM_θ: it cannot be assumed a priori that the bunch is perfectly round and to estimate the width of the θ-lineouts accordingly. Also figure C2 clearly shows than only the inner part of the bunch is circular, while the surrounding halo is smeared on the incidence plane. For this reason, the actual evolution of the FWHM_θ along ϕ is measured on a set of experimental images (one set for each Lanex configuration). The result is shown in figure C4. It appears from the experimental points that the bunch width increases along ϕ: the small values found around the tangent correspond to the yellow region in figure C2, where the strongest signal soars from the background. Then, the emission rapidly spreads and the Lorentzian curve gets larger: in the experimental image, this effect is masked by the perspective and it emerges only after the signal rescaling. Beyond a certain angle $\phi = \phi_{\text{bound}}$ (10° in the example) the FWHM_θ decreases because fewer electrons are emitted away from the incidence plane. This angle is arbitrarily taken as outermost boundary of the electron bunch. Two functions of the type $\text{FWHM}_\theta = (a\phi + b)/(\phi + c) + d$ are used to fit the experimental points on both the intervals $\phi < \phi_{\text{bound}}$ and $\phi > \phi_{\text{bound}}$: the coefficients are properly chosen for the whole curve to be continuous. A detailed comparison of more experimental images allows to conclude that such trends reproduce rather well all the bunches' evolution for angles $\phi < \phi_{\text{bound}}$; the behavior for further angles varies at each shot. However, as explained in the following, ϕ_{bound} is usually outside the region of the electron emission that is considered to integrate the signal. Also, the constant term of the fit, d, is adapted for each image so that the FWHM_θ returned for $\phi = \phi_\theta$ corresponds to the B_θ measured from the main θ-lineout.

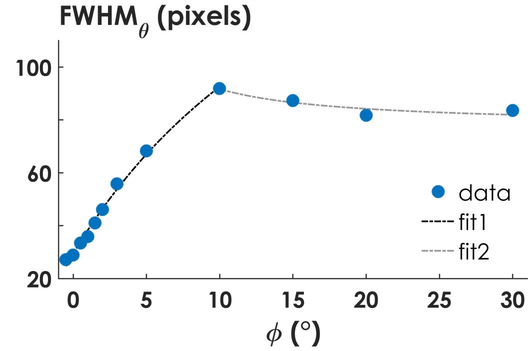

Figure C4: Evolution of the emission divergence in the θ-direction (*i.e.* FWHM_θ) measured on the image in figure C2. The lines are obtained with the function $\text{FWHM}_\theta = (a\phi + b)/(\phi + c) + d$.

A fully-defined θ-lineout is calculated for each ϕ included within the range $[C_\phi - (B_{\phi,\text{l}}/2) \cdot \sqrt{\text{e}^2 - 1}, C_\phi + (B_{\phi,\text{r}}/2) \cdot \sqrt{\text{e}^2 - 1}]$;both limits represent the value of ϕ where the Lorentz distributions along ϕ have fallen to $1/\text{e}^2$ of their peak. In the example, the upper limit is equal to 7°, which is indeed $< \phi_{\text{bound}}$. In the same spirit, each θ-lineout is integrated between $[\theta_{\min}, \theta_{\max}]$ such that the Lorentz distribution is above the same threshold A_ϕ/e^2. Figure C5 illustrates the sampling on the ϕ-lineout shown before, together with some of the θ-lineouts employed in the calculation. In the end, the sum

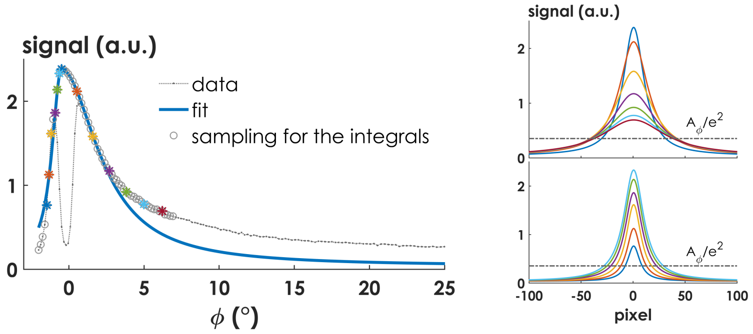

(a) (b)

Figure C5: The bunch profile in the incidence plane is sampled to reconstruct the orthogonal lineouts. (a): on the ϕ-lineout, the empty circles show the experimental points in the range retained for the calculation. (b): some θ-lineouts, for $\phi > C_\phi$ (top) and $\phi < C_\phi$ (bottom). They are reconstructed with the peaks indicated with the colored stars in (a) and the FWHM$_\theta$ from the trend given in figure C4. The horizontal axis is expressed in pixels because each profile drawn at different ϕ subtends, for the same number of pixels, a different θ-range (see equation C1 with SP$_x \propto \phi$). The threshold A_ϕ/e^2 is also indicated.

of the integrals returns the total signal of the electron bunch, expressed in pixel counts. Together with the bunch size, it provides the signal density (in pixel count/mm^2) that will be converted to charge (pC) after the calibration of the Lanex screen.

It is interesting to compare the outcome of such procedure with the direct measurement of the signal on the raw image C2. Considering an area which covers the same angular range chosen for the integrals, it turns out that the result of the direct count is $\sim$ 1.6 times smaller than the sum of the integrated θ-lineouts. This proves that the entirety of the signal corrections imposed by the geometry of the setup is not negligible, and indeed it becomes more significant when changing the incidence angle.

The procedure described so far is employed to retrieve also the characteristics of the electron emission for non-resonant angles. Although a weaker and broader signal is observed, the Lorentz distributions along θ still reproduce the experimental points, allowing to define a region where to integrate the signal. On the contrary, whenever the profiles along ϕ cannot be fitted, it is arbitrarily assumed that FWHM$_\phi$ =FWHM$_\theta$. Figure C6a shows some raw images of the incidence scan on a G30, together with its θ-lineouts and the corresponding fits.

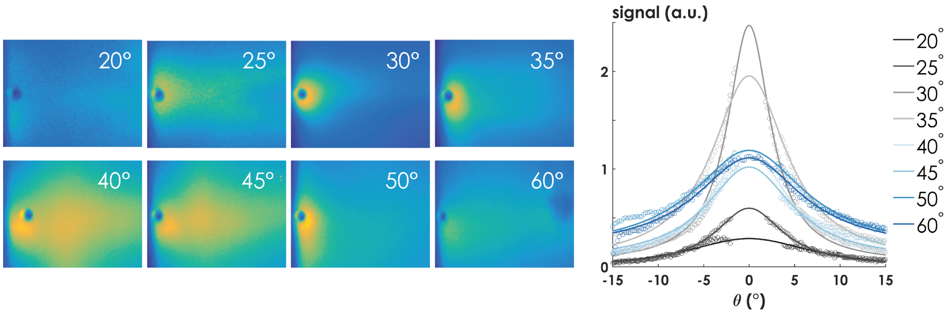

(a) (b)

Figure C6: Incidence scan on a G30: raw images (a) and θ-lineouts centered on the maximum signal (b). Different color ranges are applied to enhance the distributions: $[0, 0.6 \times 10^6]$ for 20° and 25°, $[0, 2.4 \times 10^6]$ for 30° and 35°, $[0, 1.2 \times 10^6]$ for the other angles.

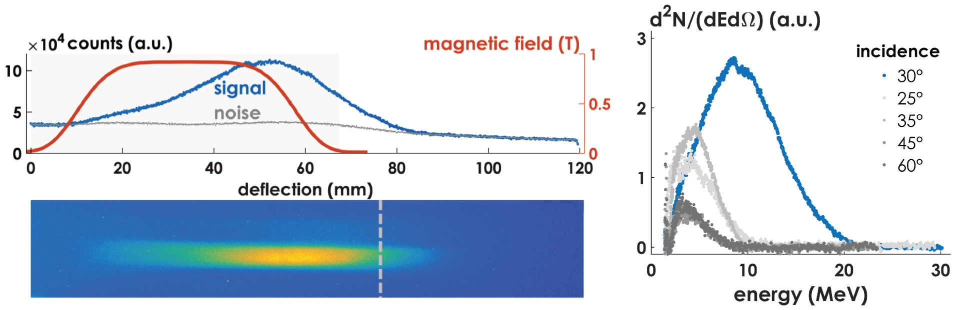

(a) (b)

Figure C7: Analysis of energetic spectra in the tangent direction produced by a G30. (a): raw image and lineout of the spectrum recorded at resonance (signal and noise); the red curve indicates the profile of the magnetic field. The grey region in the plot and the dashed line on the image mark the size of the iron yoke. (b): deconvolved and normalized spectra for different incidence angles; the blue curve corresponds to the signal shown in (a).

.3 Electron energetic spectra

Figure C7a reports the raw image and lineout of the energetic spectrum measured on the same laser shot of figure C2, that is a G30 irradiated at resonance. Because the spectrometer is aligned behind the Lanex screen, it has collected the electrons emitted in the tangent direction.

The spectrum profile is measured by averaging the signal over its whole divergence (*i.e.* the thickness of the streak in the vertical direction); the noise is obtained with a similar lineout taken immediately outside of the spectrum. Saturated pixels caused by X-rays are removed from the image using a filter which replaces the saturated pixel with the average signal of its surroundings. Similarly to what happens with the large Lanex screen, the perspective causes a slight non-linearity into the pixel-to-mm conversion, which becomes more significant when increasing the incidence angle (*i.e.* when the spectrometer moves away from the CCD). This effect clearly appears in figure C7a from the extent of the yoke, which shrinks after the conversion of the longitudinal axis. The reference images of the spectrometer's screen are therefore necessary to recover the actual spatial dispersion before getting to the energetic distribution. Likewise, the signal must be properly rescaled to take into account the observation angle and distance from the CCD.

The deconvolution of the noise-free signal is reported in figure C7b, for both the laser shot shown in the image and for a complete scan of the incidence angle on the grating target. The signal is normalized to 10^5 counts. The positions of the maximum signal, E_{peak}, and of its 10%, E_{cutoff}, are finally selected to characterize all the spectra.

Appendix D

SP-enhanced proton acceleration

As already reminded in chapter 3, the enhanced energy absorption in correspondence of the excitation of a SP has been studied, both numerically and experimentally, in relation to ion acceleration. This appendix discusses the measurements of the maximum proton energy at the rear surface of the grating targets realized during the experimental campaigns devoted to surface electron acceleration. After a short introduction about the acceleration mechanism relevant to the experimental conditions reported in this work, the most recent results are compared to the experiment performed at CEA in 2012 [9]. Interesting differences are remarked, leaving room for further investigation on the possible correlation of the electron and ion emission.

.1 Target Normal Sheath Acceleration

In the early 2000s, the observation of collimated, multi-MeV ion beams from the rear surface of solid targets irradiated at relativistic intensities [154–156] stimulated the development of acceleration mechanisms and interaction schemes aiming to export their remarkable properties to practical applications (*e.g.* proton radiography, heating and probing of warm dense matter, fast ignition of Inertial Confinement Fusion targets, radio-biological treatments, etc., see [19] for a comprehensive review on this topic). On account of the interaction parameters presented in chapter 1 (laser intensity, polarization, target thickness), ion acceleration can be explained here in terms of the popular *Target Normal Sheath Acceleration* mechanism (TNSA).

Basically, a part of the hot electrons accelerated at the front surface of the target (as explained in chapter 1) and re-injected into the overdense plasma manage to cross its whole thickness and escape from the rear surface. There, the charge separation produces an intense electric field (of the order of TV/m), which is able to ionize hydrocarbon impurities and ions from the surface and to accelerate them towards vacuum. A sketch of this mechanism is shown in figure D1.

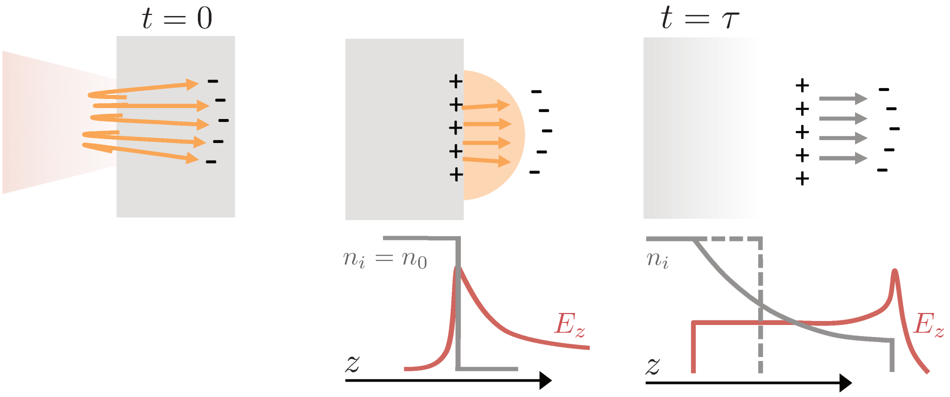

Figure D1: Schematic steps of the TNSA mechanism. The laser field pushes some hot electrons inside the target. Once they cross it, they create a space-charge electric field directed along the normal to target surface; this field accelerates protons and light ions, while the heavier ones are still fixed at the surface. At later times (t comparable with the laser duration) also heavier ions leave the target and a quasi-neutral plasma expands towards vacuum. The profiles in bottom part of the image show the ion density profile and the electric field along the two stages of the acceleration.

The sheath electric field is peaked at the target surface and protons are most favored to acquire high energies in the first steps of the process, when heavier ions can be considered still unperturbed at the surface. In this case, an estimation of the sheath field is:

$$E_{\mathrm{s}} \simeq \frac{\mathcal{E}_{\mathrm{hot}}}{e\lambda_{\mathrm{D}}}$$

This expression results from assuming that the space-charge electric field balances the energy 1.12 of the escaping electrons and extends over a distance comparable to the Debye length, $\lambda_{\mathrm{D}} = v_{th,e}/\omega_p$, where $v_{th,e} \propto T_{\mathrm{hot}}$ from equation 1.12 on page 12. A test proton within such field would gain the energy $\mathcal{E}_p \simeq eE_{\mathrm{s}}\lambda_{\mathrm{D}} = \mathcal{E}_{\mathrm{hot}}$ resulting, for example, in MeV energies for laser intensities of about 10^{20} W/cm^{2}at $\lambda = 800$ nm. This estimation also indicates a proton energy scaling $\propto I^{1/2}$ which, despite being supported by numerous experiments, relies on the approximate expression of the electron temperature, does not discriminate the dependence on the pulse energy and duration, and neglects other elements such as the target thickness and density gradients [157].

A more rigorous solution for the electric field is obtained by solving Poisson's equation for a fixed, step-like ion background and a Maxwellian distribution for energetic electrons. But at later times, also heavier ions acquire kinetic energy and contribute to the temporal evolution of the sheath field. In this case, the solutions to the ion fluid equations describe the expansion of a quasi-neutral plasma (as in chapter 1) and account for the ion rarefaction front, which moves at the ion acoustic velocity $c_s = [ZT_{\text{hot}}/(Am_p)]^{1/2}$ and the exponential energetic spectrum, which has a cutoff energy in correspondence of the velocity of foremost ions, where the neutrality assumption breaks [2]. Significant drawbacks related to the main assumptions of these descriptions (*e.g.* quasi-neutrality, the isothermal electron spectrum) have been addressed in many theoretical works that can be found in the references within [19].

For the scope of this appendix, increased energy absorption at the target laser-irradiated surface is expected to drive ions to higher energies thanks to a more numerous and more energetic population of hot electrons that create the sheath field. As already pointed out in the body of the manuscript, target structuring is largely explored to achieve this goal, and the contribution of SP excitation with gratings has been already investigated both in numerical simulations [114] and experiments.

In particular, figure D2 shows the cutoff proton energy measured at CEA Saclay in 2012 either from a flat foil or a grating target (G30) irradiated at various incidence angles [9]. Consistently with the behavior of the target absorption predicted by the vacuum heating mechanism (compare expression 1.14 on page 15), the proton energy achieved with flat foils increases with larger incidence angles; the red dashed line, indeed, scales as $[\propto \sin^2(\phi_i)/\cos(\phi_i)]$. Enhanced absorption merely caused by the surface corrugation of grating targets explains the emission of more energetic protons for all incidence angles below $\sim 40°$ (further above, gratings and flat foils give comparable results). However, the excitation of a SP in correspondence of the resonant angle (*i.e.* 30°) emerges from the expected geometrical scaling with a ~ 2.5 times increase of the proton energy.

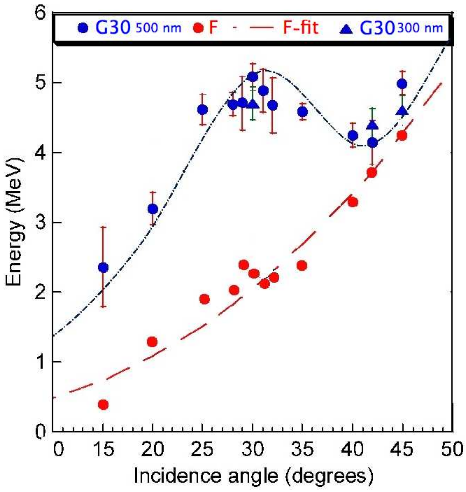

Figure D 2: Maximum proton energy as a function of the incidence angle, for flat and grating targets. From [9].

Although limited to a single grating type, this experiment demonstrated for the first time the enhanced absorption of solid gratings due to the excitation of SPs in the relativistic regime. The following section, instead, looks into the dependence of the proton energy on the resonant angle, relying on the results of the most recent campaigns run at CEA.

.2 Results

In all the experiments presented in chapter 3, the study of SP-driven electron acceleration was carried out along with the measurement of proton acceleration from the rear surface of thin targets, both flat foils and gratings. That allowed to explore the resonance curve of both emissions as a function of the incidence angle and to look for their possible correlation.

Ion detection

As already anticipated in the layout of the interaction chamber, the energy of the ion beams is measured by a Thomson parabola aligned along the normal direction to the target rear surface.

The Thomson parabola is a mass-spectrometer built with parallel electric and magnetic fields in order to steer along parabolic trajectories charges that have different energies and charge-to-mass ratio. Referring to the geometry in figure D3a, a charged particle with velocity v_x enters the region with the electric and magnetic fields aligned along z.

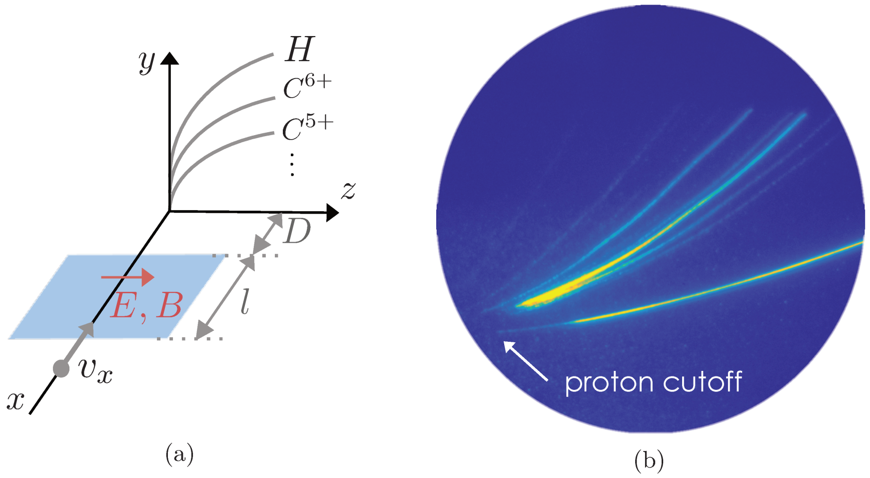

(a)

(b)

Figure D3: (a): operation of a Thomson parabola. Charges are deflected by parallel E, B fields in the region ℓ and reach the detector at a distance D with a displacement (y, z) proportional to their energy. The traces left on the detector are parabolas discriminated by the charge-to-mass ratio of the deflected particles. (b): example of the signal recorded by the Thomson parabola at CEA. The maximum proton energy is found at the edge of the corresponding parabola.

Since laser-driven ions never reach relativistic velocities, the straightforward integration of the linear equations of motions gives the deflections (y, z) when the particle arrives at the detector:

$$y = B\ell D \frac{Ze}{M} \frac{1}{v_x^2}; \qquad z = E\ell D \frac{Ze}{M} \frac{1}{v_x}, \tag{D1}$$

where ℓ is the length of the electric and magnetic plates, D is the distance to the detector, and M is the ion mass ($M = Am_p$). Therefore, it turns out that $z \propto y^2$, describing a parabola; the position of the particle along the parabola is determined by its energy, where the smaller the energy, the higher the deflection; also, charges with the same Z/A ratio will be deflected along the same path. It is also possible to re-arrange the expression of the trajectories to discriminate the charged particles depending on their momentum per unit charge, energy per unit charge, velocity or charge-to-mass ratio [158]. Different parabolas are resolved depending on the size of the collimating pinhole at the entrance of the device and the distances from the particle source and the EM fields. Furthermore, if the detector is absolutely calibrated, the intensity of the signal along the curves can be related to the particle number in order to obtain the energetic spectrum.

The Thomson parabola employed in the experiments at CEA Saclay is characterized by a magnetic field of ~ 3700 Gauss and an electric field of ~ 50 kV/m. The collimating pinhole at the entrance of the device has a diameter 100 μm, resulting into a ~ 200 keV resolution for proton energies around 5 MeV. The detector is micro-channel plate (MCP) coupled to a phosphor screen and imaged by a triggered, 12-bit Guppy PRO CCD camera. The MCP is a high-resolution, spatially-resolved electron multiplier. It consists of a matrix of glass capillaries fused together and sliced into thin wafers. A photon or a charged particle hitting the walls of the capillaries generates secondary electrons, which are drifted towards the scintillating screen by an externally-applied electric field. As the generation of the electron cascade depends on the energy and species of the impinging particle, the MCP calibration is generally quite complex [159]. With regard to this work, the MCP was not calibrated, and only the proton maximum energy was inferred by the images of the phosphor screen, which appear as in figure D3b. By fitting the experimental traces with the equations for the trajectories D1, the maximum energy is found at the point closest to the coordinate of zero deflection, *i.e.* the point where the neutral particles and photon hit the detector.

.2.1 Experimental and numerical results

All thin gratings listed in table 2.1a on page 36 were irradiated at different incidence angles and the Thomson parabola, aligned in the normal direction at the rear surface of the target, measured the maximum energy of the TNSA-driven proton beam. The result is presented in figure D4a.

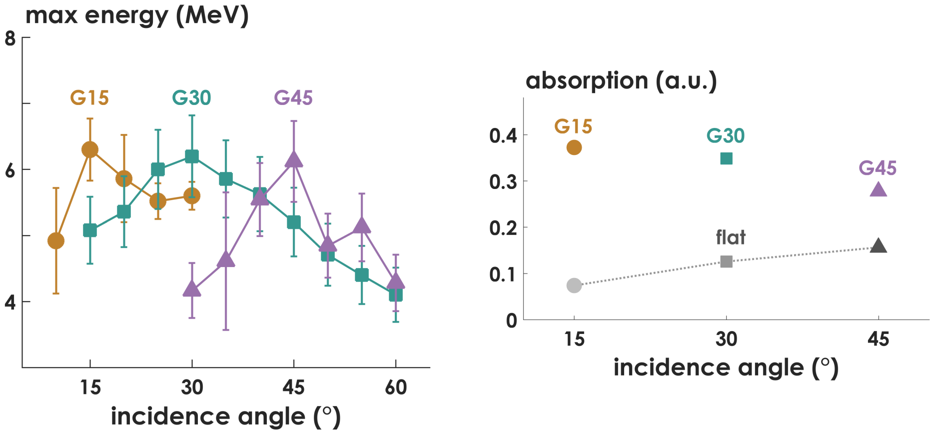

(a) Experimental results

(b) 2D PIC simulation

Figure D4: (a): maximum energy of the protons emitted at the rear surface of thin gratings. More than 6 MeV are attained in correspondence of the resonant angle for SP excitation. (b): absorption of thin gratings and flat foils at the resonant angles: the angular dependence expected by the vacuum heating mechanism does not apply to different resonant gratings.

Each point in the graph represents the average of all the shots collected at a given incidence angle over several days. The comparison of different days in the same plot was justified by the stable trend of each curve, in spite of the large energy fluctuations that, however, are accounted for by the error bars (estimated with the standard error). Visibly, all gratings show an increment of the proton energy at the resonant angle for SP excitation. In all cases, the maximum energy exceeds 6 MeV and it is ~ 1.5 times higher the point at lowest energy.

Remarkably, all the gratings display a neat resonant curve, which seems independent of the geometrical scaling found in figure D2. In support to that, the energy gain does not increase when using larger resonant angles (*i.e.* the G45 over the other gratings), contrarily to what was expected in [9]. As further evidence, figure D4b shows the values of the energy absorption issued by 2D PIC simulations for all thin gratings irradiated at the resonant angle (compare section 3.4 for the details on the numerical parameters). This plot clearly shows that the grating with the higher absorption is G15, and that the angular dependence predicted by vacuum heating (and confirmed by the points calculated on flat targets in the same figure) does not apply when comparing different resonant gratings.

These points raise new questions on the grating parameters affecting the energy absorption, as it was shown in chapter 3 that neither the grating depth or the number of periods illuminated by the focal spot should strongly affect the particle acceleration in the range of values considered here. It should be noted that also within the experimental points the G15 at 15° of incidence results in protons slightly more energetic than G45 at 45°, but their difference is within the resolution of the Thomson parabola, so it is not conclusive. To this extent, the experimental results confirm that among the thin gratings there is not a most efficient one, as in the case of surface electron acceleration (compare figure 3.10 and 3.20 in chapter 3).

Although the resonance curves displayed in figure D4a suggest that the proton acceleration is correlated with an efficient electron emission, the experiments were carried out aiming at the investigation of the best interaction conditions for the surface electron acceleration. This means, for example, that the target position was adjusted depending on the intensity of the electron signal recorded by the Lanex screen, and not on the maximum proton energy detected by the Thomson parabola. Therefore, assessing the correlation between proton and electron acceleration requires a thorough scan of which parameters simultaneously optimize both emissions. Evidence of such correlation would provide unprecedented information on the role of relativistic SPs.

To summarize, this appendix presented the results on proton acceleration from thin grating targets.

All gratings show a $\sim \times 1.5$ increase of the maximum proton energy at the incident angle expected for SP excitation. In particular, the proton energy does not increase with larger incidence angles, in contrast with the behavior of the energy absorption predicted by the vacuum heating mechanism. PIC simulations suggest, on the contrary, that the highest absorption occurs with smaller grating periods.

These results encourage to extend the investigation to sub-wavelength gratings and to further explore which interaction conditions might lead to an efficient generation of both electron and protons energetic beams.

List of abbreviations

ASE Amplified Spontaneous Emission

CPA Chirped Pulse Amplification

CWE Coherent Wake Emission, mechanism for high-order harmonic generation in the non-relativistic regime [136]

DPM Double Plasma Mirror

F Flat foil

G Grating, followed by the incidence angle for surface plasmon excitation

GIST Gwanju Institute for Science and Technology, Republic of Korea, `https://ewww.gist.ac.kr/en/`. The experiment was performed at CORELS, Centre for Relativistic Laser Science `http://corels.ibs.re.kr/html/corels_en/`.

HH High-order Harmonic

MCP Micro-Channel Plate

PIC Particle In Cell

PULSER Petawatt Ultra-Short Laser System for Extreme science Research, PW-class laser system located at GIST

ROM Relativistic Oscillating Mirror, mechanism for high-order harmonic generation in the relativistic regime [135]

SDI Spatial Domain Interferometry

SG Solid Grating, followed by its blaze angle

SP Surface Plasmon

TNSA	Target Normal Sheath Acceleration
UHI100	Ultra Haute Intensité 100 TW, laser system at CEA Saclay, France, http://iramis.cea.fr/slic/PresentationSlic.php.
XUV	eXtreme Ultra-Violet, *i.e.* λ within $[10, 100]$ nm

List of Figures

References

[1] S. M. Hooker, "Developments in laser-driven plasma accelerators", *Nat Photon* 7.10 (2013) - on pages 1, 79.

[2] A. Macchi, *A superintense laser-plasma interaction theory primer*, Springer, 2013 - on pages 1, 9–12, 24, 41, 83, 84, 131.

[3] S. Kneip et al., "X-ray phase contrast imaging of biological specimens with femtosecond pulses of betatron radiation from a compact laser plasma wakefield accelerator", *Applied Physics Letters* 99.9 (2011) - on page 1.

[4] G. Sarri et al., "Generation of neutral and high-density electron-positron pair plasmas in the laboratory." *Nature communications* 6 (2015) - on page 1.

[5] W. P. Leemans et al., "Multi-GeV Electron Beams from Capillary-Discharge-Guided Subpetawatt Laser Pulses in the Self-Trapping Regime", *Physical Review Letters* 113.24 (2014) - on page 1.

[6] W. L. Barnes, A. Dereux, and T. W. Ebbesen, "Surface plasmon subwavelength optics", *Nature* 424.August (2003) - on pages 2, 25.

[7] J. A. Schuller et al., "Plasmonics for extreme light concentration and manipulation", *Nature Materials* 9.3 (2010) - on pages 2, 25.

[8] A. Lévy et al., "Double plasma mirror for ultrahigh temporal contrast ultraintense laser pulses", *Optics Letters* 32.3 (2007) - on pages 2, 33, 34.

[9] T. Ceccotti et al., "Evidence of resonant surface-wave excitation in the relativistic regime through measurements of proton acceleration from grating targets", *Physical Review Letters* 111.18 (2013) - on pages 2, 4, 17, 48, 49, 71, 129, 131, 134.

[10] L. Fedeli et al., "Electron Acceleration by Relativistic Surface Plasmons in Laser-Grating Interaction", *Physical Review Letters* 116.1 (2016) - on pages 2, 5, 17, 43, 49, 68, 74, 78.

[11] M. Thevenet et al., "Vacuum laser acceleration of relativistic electrons using plasma mirror injectors", *Nat Phys* 12.4 (2016) - on pages 3, 47, 57, 60, 64.

[12] S. Tokita, S. Inoue, S. Masuno, M. Hashida, and S. Sakabe, "Single-shot ultrafast electron diffraction with a laser-accelerated sub-MeV electron pulse", *Applied Physics Letters* 95.11 (2009) - on page 3.

[13] I. Pomerantz et al., "Ultrashort pulsed neutron source", *Physical Review Letters* 113.18 (2014) - on page 3.

[14] L. Fedeli, A. Sgattoni, G. Cantono, and A. Macchi, "Relativistic surface plasmon enhanced harmonic generation from gratings", *Applied Physics Letters* 110.5 (2017) - on pages 3, 5, 82, 87, 88, 94, 96, 98, 99, 103.

[15] M. Yeung et al., "Near-monochromatic high-harmonic radiation from relativistic laser-plasma interactions with blazed grating surfaces", *New Journal of Physics* 15 (2013) - on pages 4, 86, 87, 95, 103.

[16] L. Fedeli, "High Field Plasmonics", PhD thesis, 2016 - on pages 5, 42, 43, 48, 66, 68, 70, 79, 82, 87.

[17] P. Gibbon, *Short pulse laser interactions with matter*, Imperial College Press, 2005 - on pages 8, 12, 14, 15, 83.

[18] W. L. Kruer, *The physics of laser plasma interactions*, Westview, 2003 - on pages 9–11.

[19] A. Macchi, M. Borghesi, and M. Passoni, "Ion acceleration by super-intense laser-plasma interaction", *Reviews of Modern Physics* 85.2 (2013) - on pages 10–12, 129, 131.

[20] P. Mulser and D. Bauer, *High power laser-matter interaction*, Springer, 2010 - on page 11.

[21] A. Macchi, F. Cattani, T. V. Liseykina, and F. Cornolti, "Laser acceleration of ion bunches at the front surface of overdense plasmas", *Physical Review Letters* 94.16 (2005) - on page 11.

[22] C. Thaury and F. Quéré, "High-order harmonic and attosecond pulse generation on plasma mirrors: basic mechanisms", *Journal of Physics B: Atomic, Molecular and Optical Physics* 43.21 (2010) - on pages 11, 82–86, 88, 93.

[23] D. E. Baldwin, "Resonant Absorption in Zero-Temperature Nonuniform Plasma", *Physics of Fluids* 12.3 (1969) - on page 13.

[24] F. Brunel, "Not-so-resonant, resonant absorption", *Physical Review Letters* 59.1 (1987) - on page 14.

[25] H. Popescu et al., "Subfemtosecond, coherent, relativistic, and ballistic electron bunches generated at $\omega 0$ and $2\omega 0$ in high intensity laser-matter interaction", *Physics of Plasmas* 12.6 (2005) - on page 14.

[26] P. Gibbon, "Efficient production of fast electrons from femtosecond laser interaction with solid targets", *Physical Review Letters* 73.5 (1994) - on page 14.

[27] T. Liseykina, P. Mulser, and M. Murakami, "Collisionless absorption, hot electron generation, and energy scaling in intense laser-target interaction", *Physics of Plasmas* 22.3 (2015) - on page 14.

[28] P. Mulser, H. Ruhl, and SteinmetzJ., "Routes to irreversibility in collective laser-matter interaction", *Laser and Particle Beams* 19 (2001) - on page 14.

[29] W. L. Kruer and K. Estabrook, "JxB heating by very intense laser light", *Physics of Fluids* 28.1 (1985) - on page 16.

[30] A. Macchi, A. Sgattoni, S. Sinigardi, M. Borghesi, and M. Passoni, "Advanced strategies for ion acceleration using high-power lasers", *Plasma Physics and Controlled Fusion* 55.12 (2013) - on page 16.

[31] H. Ruhl, A. Macchi, P. Mulser, F. Cornolti, and S. Hain, "Collective Dynamics and Enhancement of Absorption in Deformed Targets", *Physical Review Letters* 82.10 (1999) - on page 17.

[32] O. Klimo et al., "Short pulse laser interaction with micro-structured targets: simulations of laser absorption and ion acceleration", *New Journal of Physics* 13.5 (2011) - on pages 17, 70.

[33] V. Floquet et al., "Micro-sphere layered targets efficiency in laser driven proton acceleration", *Journal of Applied Physics* 114.8 (2013) - on page 17.

[34] D. Margarone et al., "Laser-driven proton acceleration enhancement by nanostructured foils", *Physical Review Letters* 109.23 (2012) - on page 17.

[35] M. Passoni et al., "Energetic ions at moderate laser intensities using foam-based multi-layered targets", *Plasma Physics and Controlled Fusion* 56.4 (2014) - on page 17.

[36] A. Zigler et al., "Enhanced proton acceleration by an ultrashort laser interaction with structured dynamic plasma targets", *Physical Review Letters* 110.21 (2013) - on page 17.

[37] A. Andreev, N. Kumar, K. Platonov, and A. Pukhov, "Efficient generation of fast ions from surface modulated nanostructure targets irradiated by high intensity short-pulse lasers", *Physics of Plasmas* 18.10 (2011) - on page 17.

[38] S. Jiang, A. G. Krygier, D. W. Schumacher, K. U. Akli, and R. R. Freeman, "Effects of front-surface target structures on properties of relativistic laser-plasma electrons", *Physical Review E - Statistical, Nonlinear, and Soft Matter Physics* 89.1 (2014) - on page 17.

[39] T. Kluge et al., "High proton energies from cone targets: electron acceleration mechanisms", *New Journal of Physics* 14.2 (2012) - on page 17.

[40] T. Taguchi, T. M. Antonsen, and H. M. Milchberg, "Resonant heating of a cluster plasma by intense laser light", *Physics of Plasmas* 12.5 (2005) - on page 17.

[41] M. Burza et al., "Hollow microspheres as targets for staged laser-driven proton acceleration", *New Journal of Physics* 13.1 (2011) - on page 17.

[42] P. Mulser, M. Kanapathipillai, and D. H. H. Hoffmann, "Two very efficient nonlinear laser absorption mechanisms in clusters", *Physical Review Letters* 95.10 (2005) - on page 17.

[43] H. A. Sumeruk et al., "Control of strong-laser-field coupling to electrons in solid targets with wavelength-scale spheres", *Physical Review Letters* 98.4 (2007) - on page 17.

[44] M. M. Murnane et al., "Efficient coupling of high-intensity subpicosecond laser pulses into solids", *Applied Physics Letters* 62.10 (1993) - on page 17.

[45] S. Kahaly et al., "Near-complete absorption of intense, ultrashort laser light by sub-λ gratings", *Physical Review Letters* 101.14 (2008) - on pages 17, 26.

[46] S. Bagchi et al., "Surface-plasmon-enhanced MeV ions from femtosecond laser irradiated, periodically modulated surfaces", *Physics of Plasmas* 19.3 (2012) - on pages 17, 26.

[47] G. Q. Liao et al., "Intense terahertz radiation from relativistic laser-plasma interactions", *Plasma Physics and Controlled Fusion* 59.1 (2016) - on page 18.

[48] Y. T. Li et al., "Observation of a fast electron beam emitted along the surface of a target irradiated by intense femtosecond laser pulses", *Physical Review Letters* 96.16 (2006) - on pages 18, 47, 57, 61.

[49] H. Ahmed et al., "Investigations of ultrafast charge dynamics in laser-irradiated targets by a self probing technique employing laser driven protons", *Nuclear Instruments and Methods in Physics Research, Section A: Accelerators, Spectrometers, Detectors and Associated Equipment* 829 (2016) - on page 18.

[50] S. Tokita, S. Sakabe, T. Nagashima, M. Hashida, and S. Inoue, "Strong sub-terahertz surface waves generated on a metal wire by high-intensity laser pulses", *Scientific Reports* 5.1 (2015) - on page 18.

[51] A. Gopal et al., "Observation of Gigawatt-Class THz Pulses from a Compact Laser-Driven Particle Accelerator", *Physical Review Letters* 111.7 (2013) - on page 18.

[52] S. A. Maier, *Plasmonics : Fundamentals and Applications*, ed. by Springer, 2007th ed., vol. 677, 1, Springer, 2004 - on pages 18, 20, 21.

[53] C. S. Liu et al., "Nonlinear surface plasma wave induced target normal sheath acceleration of protons", *Physics of Plasmas* 22.2 (2015) - on pages 19, 24.

[54] P. K. Kaw and J. McBride, "Surface Waves on a Plasma Half-Space", *Physics of Fluids* 13.7 (1970) - on pages 19, 24.

[55] C. Riconda et al., "Simple scalings for various regimes of electron acceleration in surface plasma waves", *Physics of Plasmas* 22.073103 (2015) - on pages 20, 48, 49, 52, 53.

[56] M. Lupetti, "High power laser-grating interaction", PhD thesis, Università di Pisa, 2011 - on pages 21, 23, 24, 73.

[57] J. M. Pitarke, V. M. Silkin, E. V. Chulkov, and P. M. Echenique, "Theory of surface plasmons and surface-plasmon polaritons", 70 (2006) - on page 21.

[58] S. T. Koev, A. Agrawal, H. J. Lezec, and V. A. Aksyuk, "An Efficient Large-Area Grating Coupler for Surface Plasmon Polaritons", *Plasmonics* 7.2 (2012) - on pages 23–25.

[59] I. R. Hooper and J. R. Sambles, "Dispersion of surface plasmon polaritons on short-pitch metal gratings", *Physical Review B* 65.16 (2002) - on page 24.

[60] F. Pisani, "Ultrashort Surface Plasmon Generation by Rotating Wavefronts", PhD thesis, Università di Pisa, 2017 - on page 24.

[61] Editorial, "Surface plasmon resurrection", *Nat Photon* 6.11 (2012) - on page 25.

[62] E. Ozbay, "Plasmonics: Merging Photonics and Electronics at Nanoscale Dimensions", *Science* 311.5758 (2006) - on page 25.

[63] R. F. Oulton, V. J. Sorger, D. A. Genov, D. F. P. Pile, and X. Zhang, "A hybrid plasmonic waveguide for subwavelength confinement and long-range propagation", *Nature Photonics* 2.8 (2008) - on page 25.

[64] M. I. Stockman, "Nanofocusing of optical energy in tapered plasmonic waveguides", *Physical Review Letters* 106.1 (2004) - on page 25.

[65] D. K. Gramotnev and S. I. Bozhevolnyi, "Nanofocusing of electromagnetic radiation", *Nat Photon* 8.1 (2014) - on page 25.

[66] S. S.-W. S. Kim et al., "High-harmonic generation by resonant plasmon field enhancement", *Nature* 453.7196 (2008) - on pages 25, 87.

[67] K. J. Russell, T.-L. Liu, S. Cui, and E. L. Hu, "Large spontaneous emission enhancement in plasmonic nanocavities", *Nat Photon* 6.7 (2012) - on page 25.

[68] N. L. Gruenke et al., "Ultrafast and nonlinear surface-enhanced Raman spectroscopy", *Chem. Soc. Rev.* 45.8 (2016) - on page 25.

[69] A. G. Brolo, "Plasmonics for future biosensors", *Nature Photonics* 6.11 (2012) - on page 25.

[70] V. V. Temnov et al., "Nonlinear ultrasonics in gold-cobalt bilayer structures probed with femtosecond surface plasmons", *CLEO: 2013*, Washington, D.C.: OSA, 2013 - on page 25.

[71] M. Gu et al., "Nanoplasmonics: a frontier of photovoltaic solar cells", *Nanophotonics* 1.3-4 (2012) - on page 25.

[72] A. N. Grigorenko, M. Polini, and K. S. Novoselov, "Graphene plasmonics", *Nat Photon* 6.11 (2012) - on page 25.

[73] L. Willingale et al., "Surface waves and electron acceleration from high-power, kilojoule-class laser interactions with underdense plasma", *New Journal of Physics* 15.2 (2013) - on page 26.

[74] N. Naseri, D. Pesme, and W. Rozmus, "Electron acceleration in cavitated laser produced ion channels", *Physics of Plasmas* 20.10 (2013) - on page 26.

[75] A. Macchi et al., "Surface Oscillations in Overdense Plasmas Irradiated by Ultrashort Laser Pulses", *Physical Review Letters* 87.20 (2001) - on page 26.

[76] A. Sgattoni, S. Sinigardi, L. Fedeli, F. Pegoraro, and A. Macchi, "Laser-driven Rayleigh-Taylor instability: Plasmonic effects and three-dimensional structures", *Physical Review E* 91.1 (2015) - on page 26.

[77] T. Oksenhendler, D. Kaplan, P. Tournois, G. Greetham, and F. Estable, "Intracavity acousto-optic programmable gain control for ultra-wide-band regenerative amplifiers", *Applied Physics B* 83.4 (2006) - on page 29.

[78] N. Lefaudeux, E. Lavergne, S. Monchoce, and X. Levecq, "Diffraction limited focal spot in the interaction chamber using phase retrieval adaptive optics", *SPIE Photonics West 2014-LASE: Lasers and Sources* 8960 (2014) - on page 31.

[79] Spiricon, "Hartmann Wavefront Analyzer Tutorial", *Report* (2004) - on page 32.

[80] N. Lefaudeux, X. Levecq, L. Escolano, and S. Theis, "Large deformable mirrors for beam control of high brightness lasers", International Society for Optics and Photonics, 2013 - on page 32.

[81] J. R. Fienup, "Phase retrieval algorithms: a comparison", *Applied Optics* 21.15 (1982) - on page 32.

[82] C. Thaury et al., "Plasma mirrors for ultrahigh-intensity optics", *Nature Physics* 3.6 (2007) - on pages 32, 33, 83.

[83] M. Kaluza et al., "Influence of the Laser Prepulse on Proton Acceleration in Thin-Foil Experiments", *Physical Review Letters* 93.4 (2004) - on page 32.

[84] D. Batani et al., "Effects of laser prepulse on proton generation", *Radiation Effects and Defects in Solids* 165.6-10 (2010) - on page 32.

[85] C. Hooker et al., "Improving coherent contrast of petawatt laser pulses", *Optics Express* 19.3 (2011) - on page 33.

[86] D. M. Gold, "Direct measurement of prepulse suppression by use of a plasma shutter", *Optics Letters* 19.23 (1994) - on page 33.

[87] G. Doumy, F. Queré, O. Gobert, M. Perdrix, and P. Martin, "Complete characterization of a plasma mirror for the production of high-contrast", *Physical Review E* 69.6402 (2004) - on pages 33, 34.

[88] A. Lévy, "Accélération d'ions par interaction laser - matière en régime de ultra haut contraste laser", PhD thesis, Université Paris Sud, 2008 - on page 34.

[89] C. Palmer and E. Loewen, *Diffraction grating handbook*, ed. by N. corporation, 7th ed., Rochester, 2014 - on pages 36, 38.

[90] *Richardson gratings technical notes* - on pages 36, 38.

[91] C. Shimadzu, *Optical and Laser Devices, Blaze Wavelength* - on page 37.

[92] E. G. Loewen, M. Nevière, and D. Maystre, "Grating efficiency theory as it applies to blazed and holographic gratings", *Applied Optics* 16.10 (1977) - on pages 38, 39.

[93] C. K. Birdsall and A. B. Langdon, *Plasma physics via computer simulation*, Taylor & Francis, 2005 - on pages 40, 41.

[94] H. Fehske, R. Schneider, and A. Weisse, *Computational many-particle physics*, Springer, 2008 - on page 41.

[95] A. Sgattoni et al., "Optimising PICCANTE - an Open Source Particle-in-Cell Code for Advanced Simulations on Tier-0 Systems" (2015) - on page 42.

[96] I. Prencipe et al., "Development of foam-based layered targets for laser-driven ion beam production", *Plasma Physics and Controlled Fusion* 58.3 (2016) - on page 42.

[97] A. Macchi, *Electron acceleration by relativistic surface plasmons in laser-grating interaction, Notes on the analytical model*, Private communication, 2016 - on pages 46, 49, 52.

[98] T. Tajima and J. M. Dawson, "Laser Electron Accelerator", *Physical Review Letters* 43.4 (1979) - on page 47.

[99] F. N. Beg et al., "A study of picosecond laser-solid interactions up to 1019 W cm-2", *Physics of Plasmas* 4.447 (1997) - on page 47.

[100] H. Chen, S. C. Wilks, W. L. Kruer, P. K. Patel, and R. Shepherd, "Hot electron energy distributions from ultraintense laser solid interactions", *Physics of Plasmas* 16.2 (2009) - on page 47.

[101] S. Bastiani et al., "Experimental study of the interaction of subpicosecond laser pulses with solid targets of varying initial scale lengths", *Physical Review E* 56.6 (1997) - on page 47.

[102] F. Brandl et al., "Directed acceleration of electrons from a solid surface by Sub-10-fs laser pulses." *Physical review letters* 102.19 (2009) - on page 47.

[103] D. F. Cai et al., "Experimental study for angular distribution of the hot electrons generated by femtosecond laser interaction with solid targets", *Physics of Plasmas* 10.8 (2003) - on page 47.

[104] L. M. Chen et al., "Effects of Laser Polarization on Jet Emission of Fast Electrons in Femtosecond-Laser Plasmas", *Physical Review Letters* 87.22 (2001) - on page 47.

[105] A. G. Mordovanakis et al., "Quasimonoenergetic electron beams with relativistic energies and ultrashort duration from laser-solid interactions at 0.5 kHz." *Physical review letters* 103.23 (2009) - on pages 47, 57, 60, 63.

[106] Y. Tian et al., "Electron emission at locked phases from the laser-driven surface plasma wave", *Physical Review Letters* 109.11 (2012) - on page 47.

[107] W. Wang et al., "Angular and energy distribution of fast electrons emitted from a solid surface irradiated by femtosecond laser pulses in various conditions", *Physics of Plasmas* 17.2 (2010) - on page 47.

[108] W. M. Wang et al., "Collimated quasi-monoenergetic electron beam generation from intense laser solid interaction", *High Energy Density Physics* 9.3 (2013) - on page 47.

[109] G. Y. Hu et al., "Enhanced surface acceleration of fast electrons by using subwavelength grating targets", *Physics of Plasmas* 3102.2010 (2010) - on pages 47, 70.

[110] G. Y. Hu et al., "Collimated hot electron jets generated from subwavelength grating targets irradiated by intense short-pulse laser", *Physics of Plasmas* 17.3 (2010) - on page 48.

[111] F. Nürnberg et al., "Radiochromic film imaging spectroscopy of laser-accelerated proton beams", *Review of Scientific Instruments* 80.3 (2009) - on page 48.

[112] M. Raynaud, J. Kupersztych, C. Riconda, J. C. Adam, and A. Héron, "Strongly enhanced laser absorption and electron acceleration via resonant excitation of surface plasma waves", *Physics of Plasmas* 14.9 (2007) - on pages 48, 49, 53, 71.

[113] A. Bigongiari, M. Raynaud, C. Riconda, A. Héron, and A. MacChi, "Efficient laser-overdense plasma coupling via surface plasma waves and steady magnetic field generation", *Physics of Plasmas* 18.10 (2011) - on pages 48, 49, 53.

[114] A. Bigongiari, M. Raynaud, C. Riconda, and A. Héron, "Improved ion acceleration via laser surface plasma waves excitation", *Physics of Plasmas* 20.5 (2013) - on pages 49, 71, 131.

[115] K. Nakamura et al., "Electron beam charge diagnostics for laser plasma accelerators", *Physical Review Special Topics - Accelerators and Beams* 14.6 (2011) - on page 55.

[116] Y. Glinec et al., "Absolute calibration for a broad range single shot electron spectrometer", *Review of Scientific Instruments* 77.10 (2006) - on page 56.

[117] M. Alves, C. Arnault, and C. Bruni, "PHIL photoinjector test line", *Journal of Instrumentation* 8.01 (2013) - on page 57.

[118] T. Vinatier, P. Bambade, C. Bruni, and S. Liu, "Measurement of low-charged electron beam with a scintillator screen", *Proceedings of IPAC2014, Dresden, Germany* (2014) - on pages 57, 117.

[119] A. Buck et al., "Absolute charge calibration of scintillating screens for relativistic electron detection", *Review of Scientific Instruments* 81.3 (2010) - on pages 57, 117.

[120] G. E. Giakoumakis, C. D. Nomicos, and P. C. Euthymiou, "Light angular distribution and modulation transfer function of a fluorescent screen excited by an electron beam", *Canadian Journal of Physics* 57.12 (1979) - on page 57.

[121] S. Kahaly et al., "Direct observation of density-gradient effects in harmonic generation from plasma mirrors", *Physical Review Letters* 110.17 (2013) - on pages 64, 83, 86, 90.

[122] T. J. Yu et al., "Generation of high-contrast, 30 fs, 15 PW laser pulses from chirped-pulse amplification Ti:sapphire laser", *Optics express* 20.10 (2012) - on page 66.

[123] I. Kim et al., "Spatio-temporal characterization of double plasma mirror for ultrahigh contrast and stable laser pulse", *Applied Physics B* 104.1 (2011) - on page 66.

[124] T. M. Jeong and J. Lee, "Femtosecond petawatt laser", *Annalen der Physik* 526.3-4 (2014) - on page 66.

[125] A. Bigongiari, “High Intensity Laser-Plasma Grating Interaction: surface wave excitation and particle acceleration”, PhD thesis, Ecole Polytechnique X, 2012 - on page 71.

[126] O. Lundh et al., “Few femtosecond, few kiloampere electron bunch produced by a laser–plasma accelerator”, *Nature Physics* 7.3 (2011) - on page 79.

[127] T. Pfeifer, C. Spielmann, and G. Gerber, “Femtosecond x-ray science”, *Reports on Progress in Physics* 69.2 (2006) - on page 82.

[128] G. D. Tsakiris, K. Eidmann, J. Meyer-ter-Vehn, and F. Krausz, “Route to intense single attosecond pulses”, *New Journal of Physics* 8 (2006) - on pages 82, 84.

[129] F. Krausz and M. Ivanov, “Attosecond physics”, *Reviews of Modern Physics* 81.1 (2009) - on page 82.

[130] F. Lepine, M. Y. Ivanov, and M. J. J. Vrakking, “Attosecond molecular dynamics: fact or fiction?”, *Nat Photon* 8.3 (2014) - on page 82.

[131] G. Sansone et al., “Isolated Single-Cycle Attosecond Pulses”, *Science* 314.5798 (2006) - on page 82.

[132] Y. Nomura et al., “Attosecond phase locking of harmonics emitted from laser-produced plasmas”, *Nature Physics* 5.2 (2009) - on page 82.

[133] P. B. Corkum and F. Krausz, “Attosecond science”, *Nature Physics* 3.6 (2007) - on page 82.

[134] A. Leblanc, “Miroirs et réseaux plasmas en champs lasers ultra-intenses: génération d’harmoniques d’ordre élevé et de faisceaux d’électrons relativistes”, PhD thesis, Université Paris Sud, 2016 - on pages 83, 90, 91, 97, 102, 103.

[135] R. Lichters, J. Meyer-ter-Vehn, and A. Pukhov, “Short-pulse laser harmonics from oscillating plasma surfaces driven at relativistic intensity”, *Physics of Plasmas* 3.9 (1996) - on pages 83, 84, 137.

[136] F. Quéré et al., “Coherent wake emission of high-order harmonics from overdense plasmas”, *Physical Review Letters* 96.12 (2006) - on pages 83, 137.

[137] S. V. Bulanov, N. M. Naumova, and F. Pegoraro, “Interaction of an ultrashort, relativistically strong laser pulse with an overdense plasma”, *Physics of Plasmas* 1.3 (1994) - on page 84.

[138] B. Dromey et al., “Coherent synchrotron emission from electron nanobunches formed in relativistic laser–plasma interactions”, *Nature Physics* 8.11 (2012) - on page 85.

[139] T. Baeva, S. Gordienko, and A. Pukhov, “Relativistic plasma control for single attosecond x-ray burst generation”, *Physical Review E* 74.6 (2006) - on page 85.

[140] B. Dromey et al., "Bright Multi-keV Harmonic Generation from Relativistically Oscillating Plasma Surfaces", *Physical Review Letters* 99.8 (2007) - on page 85.

[141] H. Vincenti et al., "Optical properties of relativistic plasma mirrors", 5 (2014) - on page 85.

[142] A. Tarasevitch, K. Lobov, C. Wünsche, and D. von der Linde, "Transition to the Relativistic Regime in High Order Harmonic Generation", *Physical Review Letters* 98.10 (2007) - on page 86.

[143] B. Dromey et al., "Diffraction-limited performance and focusing of high harmonics from relativistic plasmas", *Nat Phys* 5.2 (2009) - on page 86.

[144] C. Rödel et al., "Harmonic Generation from Relativistic Plasma Surfaces in Ultrasteep Plasma Density Gradients", *Physical Review Letters* 109.12 (2012) - on page 86.

[145] R. L. Sandberg et al., "Lensless Diffractive Imaging Using Tabletop Coherent High-Harmonic Soft-X-Ray Beams", *Physical Review Letters* 99.9 (2007) - on page 86.

[146] M. Cerchez et al., "Generation of laser-driven higher harmonics from grating targets", *Physical Review Letters* 110.6 (2013) - on pages 87, 95, 96.

[147] A. Husakou, F. Kelkensberg, J. Herrmann, and M. J. J. Vrakking, "Polarization gating and circularly-polarized high harmonic generation using plasmonic enhancement in metal nanostructures", *Optics Express* 19.25 (2011) - on page 87.

[148] I.-Y. Park et al., "Plasmonic generation of ultrashort extreme-ultraviolet light pulses", *Nature Photonics* 5.11 (2011) - on page 87.

[149] M. Sivis, M. Duwe, B. Abel, and C. Ropers, "Extreme-ultraviolet light generation in plasmonic nanostructures", *Nature Physics* 9.5 (2013) - on page 87.

[150] S. Han et al., "High-harmonic generation by field enhanced femtosecond pulses in metal-sapphire nanostructure", *Nature Communications* 7.May (2016) - on page 87.

[151] X. Lavocat-Dubuis and J. P. Matte, "Numerical simulation of harmonic generation by relativistic laser interaction with a grating", *Physical Review E - Statistical, Nonlinear, and Soft Matter Physics* 80.5 (2009) - on page 87.

[152] M. Bocoum et al., "Spatial-domain interferometer for measuring plasma mirror expansion", *Optics letters* 40.13 (2015) - on page 91.

[153] B. H. Shaw et al., "High-peak-power surface high-harmonic generation at extreme ultra-violet wavelengths from a tape", *Journal of Applied Physics* 114.4 (2013) - on page 103.

[154] R. A. Snavely et al., "Intense High-Energy Proton Beams from Petawatt-Laser Irradiation of Solids", *Physical Review Letters* 85.14 (2000) - on page 129.

[155] A. Maksimchuk, S. Gu, K. Flippo, D. Umstadter, and V. Y. Bychenkov, "Forward Ion Acceleration in Thin Films Driven by a High-Intensity Laser", *Physical Review Letters* 84.18 (2000) - on page 129.

[156] E. L. Clark et al., "Measurements of Energetic Proton Transport through Magnetized Plasma from Intense Laser Interactions with Solids", *Physical Review Letters* 84.4 (2000) - on page 129.

[157] M. Borghesi, "Laser-driven ion acceleration: State of the art and emerging mechanisms", *Nuclear Instruments and Methods in Physics Research, Section A: Accelerators, Spectrometers, Detectors and Associated Equipment* 740 (2014) - on page 130.

[158] P. R. Bolton et al., "Instrumentation for diagnostics and control of laser-accelerated proton (ion) beams", *Physica Medica* 30.3 (2013) - on page 133.

[159] R. Prasad et al., "Thomson spectrometer-microchannel plate assembly calibration for MeV-range positive and negative ions, and neutral atoms", *Review of Scientific Instruments* 84.5 (2013) - on page 133.

List of scientific contributions

List of publications

with relevance to the PhD project

In preparation

[2] G. Cantono, A. Sgattoni, L. Fedeli, T. Ceccotti and A. Macchi, *Experimental enhancement of harmonic generation by relativistic surface plasmons.*

[1] G. Cantono, A. Sgattoni, L. Fedeli, A. Macchi and T. Ceccotti, *Extended study of electron acceleration by relativistic surface plasmons.*

In peer reviewed international journals

[4] L. Fedeli, A. Formenti, L. Cialfi, A. Sgattoni, G. Cantono, M. Passoni, *Structured targets for advanced laser-driven sources*, Plasma Physics and Controlled Fusion, accepted (September 2017).

[3] L. Fedeli, A. Sgattoni, G. Cantono, A. Macchi, *Relativistic surface plasmon enhanced harmonic generation from gratings*, Applied Physics Letters 110, 051103 (2017).

[2] L. Fedeli, A. Sgattoni, G. Cantono, D. Garzella, F. Réau, I. Prencipe, M. Passoni, M. Raynaud, M. Květoň, J. Proska, A. Macchi, T. Ceccotti, *Electron acceleration by relativistic surface plasmons in laser-grating interaction*, Physical Review Letters 116, 015001 (2016).

[1] A. Sgattoni, L. Fedeli, G. Cantono, T. Ceccotti, A. Macchi, *High field plasmonics and laser-plasma acceleration in solid targets*, Plasma Physics and Controlled Fusion 58, 014004 (2015).

based on work carried out before the PhD

[3] H. Ahmed, S. Kar, G. Cantono, P. Hadjisolomou, A. Poye, D. Gwynne, C. Lewis, A. Macchi, K. Naughton, G. Nersisyan, V. Tikhonchuk, O. Willi, M. Borghesi, *Efficient post-acceleration of protons in helical coil targets driven by sub-ps laser pulses*, Scientific Reports 7, 10891 (2017).

[2] H. Ahmed, S. Kar, G. Cantono, G. Nersisyan, S. Braukmann, D. Doria, D. Gwynne, A. Macchi, K. Naughton, O. Willi, C. S. Lewis, M. Borghesi,*Investigations of ultra-fast charge dynamics in laser-irradiated targets by a self proton probing technique*, Nuclear Instruments and Methods in Physics Research A 829, 172-175 (2016).

[1] S. Kar, H. Ahmed, R. Prasad, M. Cerchez, S. Brauckmann, B. Aurand, G. Cantono, P. Hadjisolomou, C. Lewis, A. Macchi, G. Nersisyan, A. Robinson, A. Schroer, M. Swantusch, M. Zepf, O. Willi, M. Borghesi, *Guided post-acceleration of laser driven ions by a miniature modular structure*, Nature Communications 7:10792 (2016).

Contributions to international conferences

[6] (talk) *Relativistic surface plasmons in laser-plasma interaction*, EPS 44th European Physical Society Conference - Belfast, Northern Ireland, 25-30 June 2017.

[5] (invited talk) *Paquets d'électrons et harmoniques d'ordre élévé générés par plasmons de surface relativistes excités par laser*, ILP 8ème Forum Lasers et Plasmas - Aussois, France, 12-16 March 2017.

[4] (invited talk) *Relativistic plasmonics for ultrashort electron and XUV sources*, INO Annual Symposium 2017 - Trento, Italy, 9-10 February 2017.

[3] (talk and poster) *Relativistic surface plasmon driven electron acceleration and high harmonic generation*, ICUIL 2016, 7th Conference on the International Committee on Ultrahigh Intensity Lasers - Montebello, Québec, Canada, 11-16 September 2017. (Award) for *Outstanding contribution to the conference.*

[2] (poster) *Experimental study of the spatial distribution of electron bunches driven by resonant relativistic plasmons*, ILP 7ème Forum Lasers et Plasmas - Ile de Porquerolles, France 14-19 June 2015

[1] (talk) *Electron acceleration by relativistic surface plasmons in laser-grating interaction*, LPAW 2015, Laser Plasma Acceleration Workshop - Guadeloupe, 10-15 May 2015.

Participation to international schools

[5] *Laser driven sources of high energy particles and radiation, Advanced Summer School*, 10-16 July 2017, Anacapri (Napoli, Italy).

[4] *2nd IPERION Doctoral Summer School, Development of innovative instruments and diagnostic strategies in heritage science*, 4-7 July 2017, Paris (France).

[3] *ELISS 2016 Summer School*, 21-26 August 2016, - Prague (Czech Republic); contributing with a poster, *Electron acceleration by relativistic surface plasmons.*

[2] *LA3NET 3rd School on Laser Applications and Accelerators* - 27 September - 3 October 2014, Salamanca (Spain); contributing with a poster, *Ultrafast Proton Probing of Laser-Driven Current Propagation.*

[1] *54th Course of International School of Quantum Electronics, atom and plasmas in intense laser fields*, 21-31 July 2013, Erice (Trapani, Italy).

université
PARIS-SACLAY

ÉCOLE DOCTORALE
Ondes et Matière
(EDOM)

Title: Relativistic plasmonics for ultra-short radiation sources

Keywords: Laser-plasma interaction, surface plasmons, electron acceleration, high-order harmonic generation

Summary: Plasmonics studies how the electromagnetic radiation couples with the collective oscillations of the electrons within a medium. Surface plasmons (SPs), in particular, have a well-established role in the development of forefront photonic devices, as they allow for strong enhancement of the local EM field over submicrometric dimensions. Promoting the SP excitation to the high-field regime, where the electrons quiver at relativistic velocities, would open stimulating perspectives for the both the manipulation of ultra-intense laser light and the development of energetic, short radiation sources. Indeed, the excitation of resonant plasma modes is a possible strategy to efficiently deliver the energy of a high-power laser to a solid target, this being among the current challenges in the physics of highly-intense laser-matter interaction.

Gathering these topics, this thesis demonstrates the opportunity of resonant surface plasmon excitation at ultra-high laser intensities by studying how such waves accelerate bunches of relativistic electrons along the target surface and how they enhance the generation of high-order harmonics of the laser frequency.

Both these processes have been investigated with numerous experiments and extensive numerical simulations. Adopting a standard configuration from classical plasmonics, SPs are excited on solid, wavelength-scale grating targets. In their presence, both electron and harmonic emissions exhibit remarkable features that support the conception of practical applications.

Putting aside some major technical and conceptual issues discouraging the applicability of plasmonic effects in the high-field regime, these results are expected to mark new promises to the exploration of Relativistic Plasmonics.

Titre: Plasmonique relativiste pour sources de rayonnement ultra-brèves

Mots clefs: Interaction laser-plasma, plasmons de surface, accélération d'électrons, génération d'harmoniques d'ordre élevé

Résumé: La plasmonique étudie le couplage entre le rayonnement électromagnétique et les oscillations collectives des électrons dans un matériel. Les plasmons de surface (SPs), notamment, ont la capacité de concentrer le champ électromagnétique sur des distances micrométriques, ce qui les rend intéressants pour le développement des dispositifs photoniques les plus novateurs. Étendre l'excitation de SPs au régime de champs élevés, où les électrons oscillent à des vitesses relativistes, ouvre des perspectives stimulantes pour la manipulation de la lumière laser ultra-intense et le développement de sources de rayonnement énergétiques et à courte durée. En fait, l'excitation de modes résonnants du plasma est l'une des stratégies possibles pour transférer efficacement l'énergie d'une impulsion laser ultra-puissante à une cible solide, cela étant parmi les défis actuels dans la physique de l'interaction laser-matière à haute intensité.

Dans le cadre de ces deux sujets, ce travail de thèse démontre la possibilité d'exciter de façon résonnante des plasmons de surface avec des impulsions laser ultra-intenses. Elle étudie comment ces ondes peuvent à la fois accélérer de paquets d'électrons relativistes le long de la surface de la cible mais aussi augmenter la génération d'harmoniques d'ordre élevé de la fréquence laser.

Ces deux processus ont été caractérisés avec de nombreuses expériences et simulations numériques. En utilisant un schéma d'interaction standard de la plasmonique classique, les SPs sont excités sur des cibles dont la la surface présente une modulation périodique régulière à l'échelle micrométrique (cibles réseau). Dans ce cas, les propriétés de l'émission d'électrons tout comme celles des harmoniques permettent d'envisager leur utilisation dans des application pratiques.

En réussissant à dépasser les principaux problèmes conceptuels et techniques qui jusqu'au présent avaient empêché l'application d'effets plasmoniques dans le régime de champs élevés, ces résultats apportent un intérêt nouveau à l'exploration de la Plasmonique Relativiste.

Université Paris-Saclay
Espace Technologique / Immeuble Discovery
Route de l'Orme aux Merisiers RD 128 / 91190 Saint-Aubin, France